



Universitat
de les Illes Balears

Title:

Noise Effects in Kerr Frequency Combs

AUTHOR: *Juan Luis Gómez González*

Master's Thesis

Master's degree in ***Physics of Complex Systems***
at the

UNIVERSITAT DE LES ILLES BALEARS

Academic year *2015/2016*

Date: 20/09/2016

UIB Master's Thesis Supervisor ***Damià Gomila Villalonga***

Contents

1	Introduction	2
1.1	Frequency Combs	2
1.2	Kerr Frequency Combs (KFC)	7
1.3	Noise in microresonator based frequency combs	11
2	Modeling	13
2.1	A spatio-temporal representation	13
2.2	Linear stability analysis	18
2.3	Characterization of noise excited sidebands	23
3	Results	26
3.1	Deterministic Combs	27
3.2	Stochastic Combs	36
4	Conclusions	52
5	Appendix	54
5.1	Appendix A: Pseudo Spectral Method	54
5.1.1	Deterministic Differential Partial Equations	54
5.1.2	Stochastic Partial Differential Equations	57
5.1.3	Approximate approaches	62
5.2	Appendix B: Discrete Fourier Transform	63
5.2.1	DFT	63
5.2.2	Subroutine Fast Fourier Transform from the West (FFTW)	65

Abstract

Frequency combs are astounding optical systems that aid to solve many technical and scientific problems. Those known as kerr frequency combs rely on the non-linear kerr effect to produce combs from a monochromatic light source in devices known as whispering gallery mode resonators. The goal of the thesis is to characterize the effect of fluctuations and to identify the scenario under which a series of modes around the pumping frequency are randomly excited. This result was obtained in the laboratory and it was not previously predicted. To that extent a spatio-temporal model 1D partial differential equation, the Lugiato - Lefever Equation, is reviewed and validated as a tool to study the dynamics of frequency combs. Consequently the stochastic version of the model is numerically solved, using a pseudo-spectral algorithm. Contributions come by characterizing fluctuations for different types of noise and comparing the numerical with the experimental results, identifying the more important mechanisms supporting such fluctuations.

Acknowledgements

First of all I want to express my sincere gratitude to IFISC institute for granting me a IFISC scholarship to pursue my MSc degree. Next I want to thank my supervisor Damià Gomila for giving me the opportunity of working in the topic of Kerr Frequency Comb and pattern formation modeling. Over the time preparing my thesis the skills in numerical modeling and the peculiar scientific way of being creative I have learnt are currently part of my daily piece of work. Next I would like to mention my new supervisors Rafael Rodrigo and Luisa Lara for allowing me to share my time between master thesis and research work in planetary science modeling. During the master course, the fact of studying at a new university and in particular at IFISC gave me different points of view of what is physics and how can be used. I consider this a very important contribution to my background as physicist. Along with this, conversations held among my master colleagues were an influence as important as the master program itself, creating me new interests and new insights that will grow with me. Finally I want to give my gratitude to my family for supporting me anytime.

Chapter 1

Introduction

1.1 Frequency Combs

The nobel prize in 2005 was half awarded both to John L. Hall and Theodor W. Hänsch for their contribution to spectroscopy sciences and the development of Frequency Combs techniques. An ideal **Frequency Comb** (FC) is basically a frequency spectrum composed of an evenly spaced sequence of discrete delta dirac peaks. The frequency domain is given by

$$f(q) = f_0 + qf_r, \quad q \in \mathbb{Z} \quad (1.1)$$

Where integer q labels the peak, f_0 is called the carrier offset frequency and f_r the comb tooth spacing. In reality such exact spectrums can not exist due to the ideal properties of the dirac delta function. More realistic combs are achieved performing the fourier transform to trains of evenly spaced short pulses. This still leads to the formation of discretized spectrums. The envelope of the pulse is related to the amplitude of fourier coefficients, Fig. 1.1.

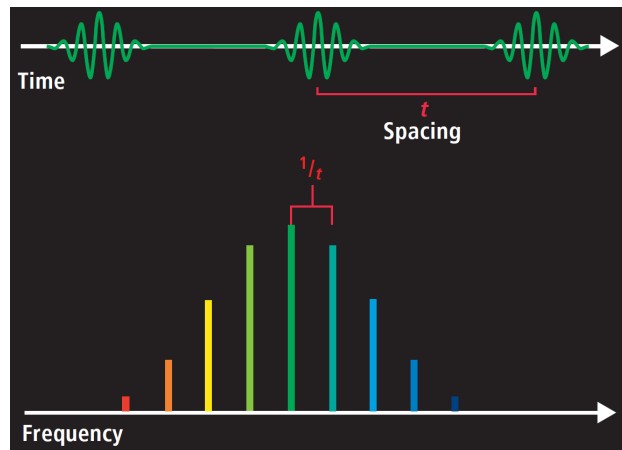


Figure 1.1: The fourier transform of a train of pulses is a frequency comb. $f_r = 1/t$ where t is the temporal distance between pulses [1].

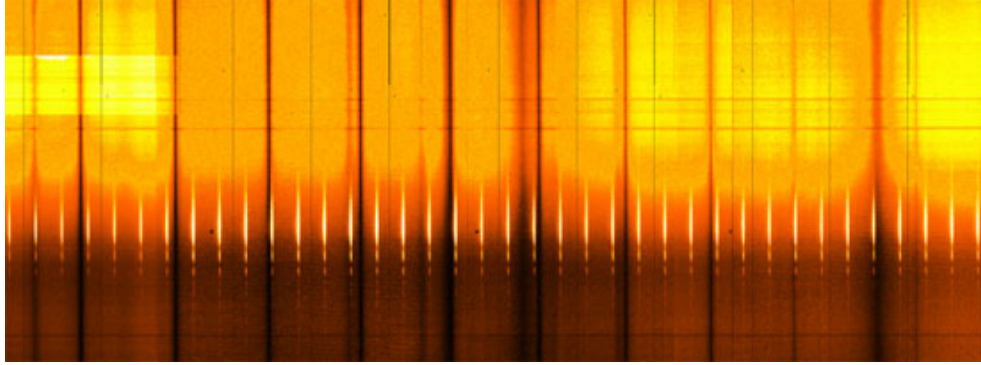


Figure 1.2: Basic purpose of Frequency Combs as frequency ruler. Figure shows a section of the Sun absorption spectrum around 189.3THz (1584nm) in dark stripes. As bright shorter vertical lines the spectral calibration of a particular frequency comb [19].

Access to control of these systems has vastly contributed to many fields. The underlying nature of frequency comb based technology is optical. That is the reason these systems are usually named Optical Frequency Combs [1]. Visible light oscillates at about 10^{15} cycles per second. An adequate knowledge of light manipulation would lead to use those high frequencies to explore similar high frequency phenomena. In spite of for microwave regime, technology is available and easily accessible to accomplish such kind of tasks for a long time, that remained unveiled for optical light until recently. In this context optical frequency combs would play a similar role to the traditional oscilloscope, but opening the direct manipulation of optical frequencies.

Some of the areas benefited from the use of frequency combs are: development of **Optical Atomic Clocks** [2], **Exoplanets Search** [3], measurement and **Validation of Fundamental Constants** constancy [4], **Photonic** sciences [5], **LIDAR** techniques [6], and of course high precision **Spectroscopy** [7] to time scales without precedents as seen in Figure 1.2, among many others.

The analogy to a spectral ruler is partially exact. Even though the resemblance is clear, to take advantage of the comb one just does not overlap spectrums to make direct measurements. Instead the procedure is detecting the effect of adding up the frequency to be determined with its closest frequency in the comb. After channeling the combination through nonlinear mixers, the output presents components that are product of harmonic functions involving the sum and difference of the input frequency. These “beatings” are of smaller frequency and easy to measure, therefore the desired frequency too. This technique is known as **Heterodyne Detection**.

Prior to the development of combs, a regular laser was used to obtain light at a very precise frequency. In comparison to a musical instrument, it is similar if a violin could only produce one single note. In that way to create music with light one requires an orchestra of single frequency lasers. The comb stands as that entity at once. As it is suggested by the very beginning of this thesis, such improvement could be accompanied by a source of light capable of output a periodic rate of short pulses. Those devices, responsible for the Nobel prize award, are known as **Mode-Locked Lasers** [8].

A laser is mainly composed of an active medium capable of exhibiting spontaneous emission, a

pumping process to induce population inversion and optical feedback elements such as mirrors. The last component forces the light to be trapped in a kind of optical cavity. It helps to increase the number of photons enhancing the spontaneous emission process before being emitted through the number of roundtrips they are able to perform.

The modes supported by the laser cavity are those that satisfy the boundary conditions. Hence, axial modes must be an integer number of times half roundtrip length assuming at the mirror-ends electric field is zero.

$$f_q = q \frac{c}{2L} \quad (1.2)$$

The quantity $f_r = c/2L$ where c is the light speed in the medium and L the cavity length, is known as **Free Spectral Range**. This is the lowest admitted frequency and the separation between modes.

In principle a single frequency laser may excite several modes which oscillates independently if losses are undertaken. In addition relative phases would be selected at random. Nevertheless a mode-locked laser precisely makes this quantity a fixed magnitude $\phi_q - \phi_{q-1} = cte$. Under this assumption the combination of $2n + 1$ modes with amplitude E_0 around a central mode f_c reads

$$E(t) = \sum_{q=-n}^n E_0 e^{i(f_c + qf_r)t + i\phi_q} \quad (1.3)$$

Expressing $\phi_q = qC + \phi_0$ plus carrying out a translation of time $t \rightarrow t - C/\Delta\nu$ the sum becomes

$$E(t) = E_0 e^{if_c t + i\phi_0} \sum_{q=-n}^n e^{iqf_r t} = A(t) e^{if_c t} \quad (1.4)$$

Thus this basic examples appears as a carrier frequency ν_0 modulated by a time varying envelope $A(t)$. This particular example allows to compute analytically such envelope

$$|A(t)|^2 = \frac{\sin((2n+1)f_r t/2)^2}{\sin(f_r t/2)^2} \quad (1.5)$$

This is a periodic function, which resembles a train of pulses that shortens as n increases. Precisely its fourier transform converges to the comb spectrum, centered at mode f_c . The result is similar if amplitudes follow some distribution meanwhile phases are locked. There exists 3 basic mechanisms to induce mode-locking of modes:

Active Mode Locking An electro-optical or acousto-optical modulator placed inside the cavity acts as a shutter opening only at times the light completes a roundtrip. Providing the frequency is f_r this technique attenuates radiation outside the intensity peak interval of the pulse train.

Passive Mode Locking An absorber medium is placed inside the cavity, whose radiation absorption capacity depends on the light intensity. Intense peaks are not affected meanwhile small amplitude fluctuations diminish. The pulse train is reinforced this way.

Self Mode locking Analogous to the passive mode locking case, but the active medium itself presents the absorption intensity dependence.

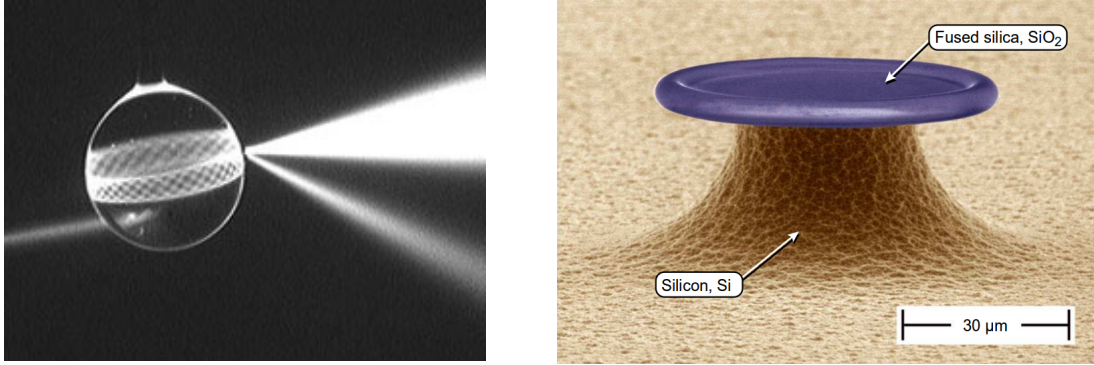


Figure 1.3: **Left:** Spherical Optical Whispering Gallery resonator already excited by a laser [9]. **Right:** Monolithic Optical Whispering Gallery Resonator build on a Silicon Wafer [11].

Experimental work of such systems was carried out from 70^s to 90^s to address comb like spectrums really displays the properties of a frequency comb. Another reality that has to be taken under consideration is the spectral span of the comb, or the domain size where spectrum lines are measurable. The simple mathematical result displayed before stated a finite combination of modes. It is not only a matter of a broader measurement capability. To be of practical usage the comb attributes need to be calibrated.

The presence of the offset frequency in the spectrum is an unknown quantity after building the system. Its presence is due to the particular phase shift happening between the carrier frequency and the amplitude envelope maximum. To tackle the determination of this magnitude, the most simple process is **Self Referencing**. Part of the comb light is passed through a non linear crystal which doubles all comb frequencies. Then, given the peak corresponding to the first detectable line labeled by n , $f_1 = nf_r + f_0$ the non linear process yields $f_d = 2(nf_r + f_0)$. Adding back together both pulsed beams, there should be a frequency $f_2 = 2nf_r + f_0$ at the other side of the spectrum. Hence the location of f_2 differs from f_d only by f_0 . Finally in the self-referenced comb this offset frequency is detectable as a beating radio frequency by heterodyne detection. This is general for all combs. To that extent, the comb needs to span a full **Octave**. An octave is defined such as

$$octave = \log_2 \left(\frac{f_2}{f_1} \right) \quad (1.6)$$

This is the requirement for high spanning frequency combs. Otherwise such measurement is not simple. New optical systems appeared as different actors producing optical frequency comb, and also contributing with better performance for some capabilities. For instance in 1999 fiber based lasers, through a non linear medium, were able to output octave spanning spectrums easily [20].

Most recently approaches to develop frequency combs come by the use of **Whispering Gallery Modes Resonators** (WGMR) [10]. These are optical microresonators, with spherical or torus geometry, capable of trapping light inside, devices displayed in Figure 1.3. Made of several materials, its name comes by the analogous acoustic effect taking place in certain galleries that also traps sound waves. Indeed the microresonator is characterized by optical modes at which the electric field resonates.

As in many resonating systems, the efficiency at storing the radiation is given by the **Quality Factor Q**. Providing the cavity is made of non linear optical material, the resonating modes interact within each others. That is the case of the **kerr effect**. The collective behaviour of the interacting modes leads to the formation of complex patterns in which some frequencies are enhanced and others suppressed. Finally light escaping the whispering gallery resonator shows frequency comb like spectrum, as indicated in Fig. 1.4, even in the case only one mode is initially coupled to the device. Results presented in this thesis stems from frequency combs obtained through modeling these **kerr frequency combs**. Next subsection will detail the physical characterization of this phenomena.

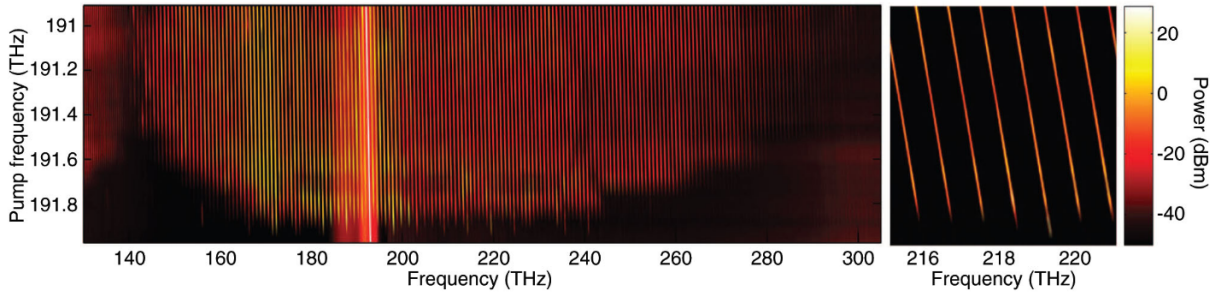


Figure 1.4: Tunable octave-spanning microresonator based frequency comb. The horizontal axis shows the measured frequency comb at different pump laser frequencies (vertical axis). The brightest line corresponds to the pump laser. Right panel shows a zoom of the spectrum [18]

1.2 Kerr Frequency Combs (KFC)

First high quality spherical resonators were introduced in 1989 by melting optical fiber tips made of Quartz [21]. For toroidal-geometry resonators they receive the name of **microtoroid** [22] and they can be sculpted on oxidized silicon wafers (fused silica). The strong confinement in microresonators gives rise to nonlinear optical effects at very low optical power levels and enable the observation of Raman lensing [23], parametric oscillations [24], **four wave mixing** [25], frequency doubling [26] and tripling [27]. In particular four wave mixing is the responsible for the appearance of KFC in WGMR.

The mechanism leading to the creation of optical patterns only requires a single frequency tunable light source such a laser. Nevertheless to excite modes in the cavity the beam needs to be coupled to the WGMR [11]. To this extent the most simple experimental set up is using a tapered optical fiber adjoining to the microcavity. Within the narrow gap among both structures, there exists an evanescent light that couples the resonator to the its nearest mode. The difference between those frequencies is an important parameter called **detuning**. Geometry is also adjustable to help the process.

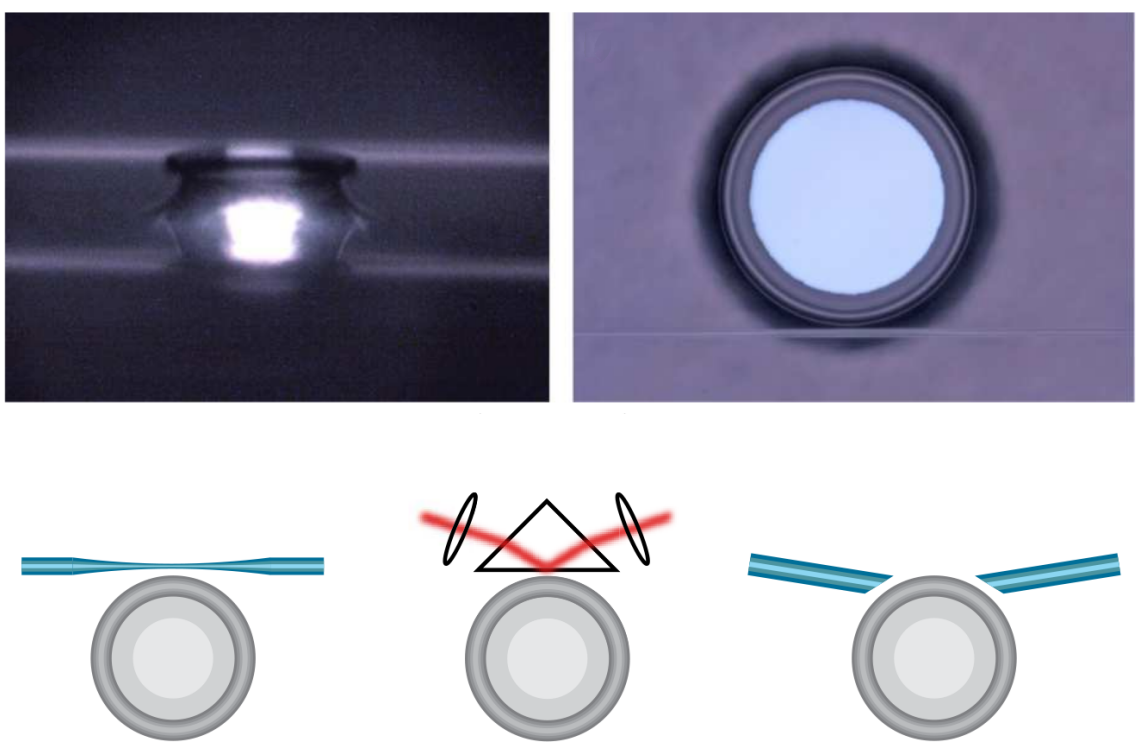


Figure 1.5: **Top:** Top and side images of a real coupling set-up. Lower part of top left picture is the reflexion of the microtoroid and fiber on the silicon wafer. **Below** Different coupling methods for microresonators [11].

Non linear optical effects are described by the response of the non linear medium on which the resonator is built to an electromagnetic wave. The interaction is expressed by the dielectric polarization $\vec{P}(\vec{E})$. This polarization can be expanded in a power series on the electric field.

$$\vec{P}(\vec{E}) = \epsilon_0 \xi \vec{E} + \epsilon_0 \xi^{(2)} \vec{E} \vec{E} + \epsilon_0 \xi^{(3)} \vec{E} \vec{E} \vec{E} + \dots \quad (1.7)$$

Kerr effect appears when assuming inversion symmetry ($\vec{P}(-\vec{E}) = -\vec{P}(\vec{E})$) on this magnitude and hence neglecting $\xi^{(2)}$ keeping up to $\xi^{(3)}$

$$\vec{P}(\vec{E}) \approx \epsilon_0 \xi \vec{E} + \epsilon_0 \xi^{(3)} \vec{E} \vec{E} \vec{E} \quad (1.8)$$

What follows outlines the analytical derivation of the **Modal Expansion Approach** [11], [12] which describes the collective interaction of light modes in the microresonator. The optical field in mediums with kerr nonlinearity fullfills the maxwell wave equation, with the nonlinear polarization $\vec{P}_{NL} = \epsilon_0 \xi^{(3)} \vec{E} \vec{E} \vec{E}$ as driving term.

$$\nabla^2 \vec{E} - \frac{n^2}{c_0^2} \frac{\partial^2 \vec{E}}{\partial t^2} = -\mu_0 \frac{\partial^2 \vec{P}_{NL}}{\partial t^2} \quad (1.9)$$

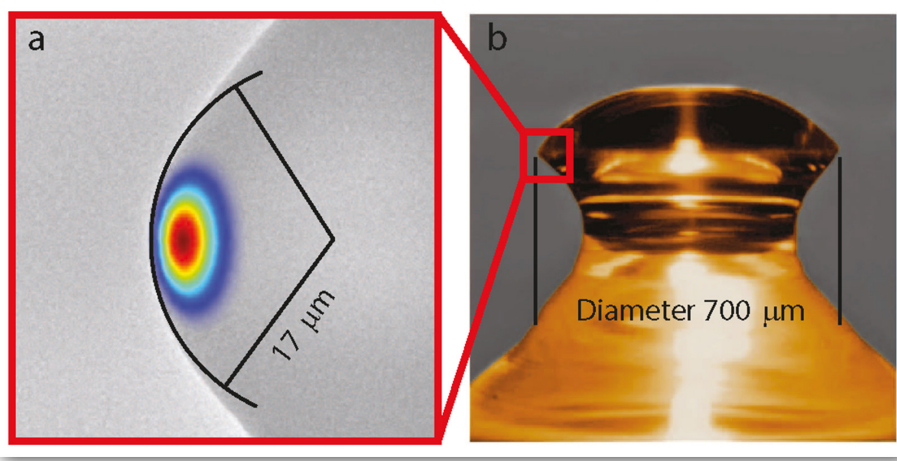


Figure 1.6: Confinement of WGM in a microresonator cavity. The confinement has approximately circular symmetry. Due to high quality factor Q and the small confinement volume, the high intensity of modes traveling inside leads to non linear kerr effects [11].

Restricting to **Whispering Gallery Modes** in microresonators. Those are cavity radial fundamental eigenmodes enhancing the light confinement as displayed in Figure 1.6. These, solutions to Eq. (1.9) with cylindrical symmetry, read

$$\vec{E}_l(r, \phi, z, t) = \frac{1}{2} A_l(t) \tilde{E}_l(r, z) e^{i(l\phi - \omega_l t)} \quad (1.10)$$

This set corresponds to the homogeneous solution of Eq. (1.9) times a time-varying amplitude due to the driving term. They characterize light modes by a single integer l regarding to the angular symmetry and photons angular momentum. Since here is only considering the fundamental radial eigenmodes, the frequencies ω_l only depend likewise on l . Though the interpretation of $|A_l|^2$ goes beyond its equivalence to $|\vec{E}|^2$, essentially it can be considered as the amplitude of the electric field inside the microresonator [11]. Inserting ansatz (1.10) into Eq. (1.9) yields

$$-\mu_0 \frac{\partial^2 \vec{P}_{NL}}{\partial t^2} = \sum_l A_l(t) \left(\nabla^2 - \frac{n^2}{c_0^2} \frac{\partial^2}{\partial t^2} \right) \tilde{E}_l e^{i(l\phi - \omega_l t)} - \sum_l \tilde{E}_l(r, z) e^{i(l\phi - \omega_l t)} \left(\frac{n^2}{c_0^2} \frac{\partial^2 A_l(t)}{\partial t^2} + 2i\omega_l \frac{n^2}{c_0^2} \frac{\partial A_l(t)}{\partial t} \right) \quad (1.11)$$

The first summatory from the right hand side vanishes since it is the evaluation of the homogeneous wave equation solution. There is another approximation arising from the fact that $A_l(t)$ varies slowly relative to its carrier frequency.

$$\left| \frac{\partial A_l(t)}{\partial t} \right| \ll \omega_l |A_l(t)| \quad (1.12)$$

This is known as **Slow varying envelope approximation**. This formulation finally reproduces the governing temporal rate $dA_l(t)/dt$, applying the previous approximation and using the orthonormality property of maxwell wave equation solutions. Projecting them to extract the targeting amplitudes, the modal expansion approach is demonstrated

$$\frac{d\mathcal{A}_\eta}{dt} = -\frac{1}{2} \Delta\omega_\eta \mathcal{A}_\eta - ig_0 \sum_{\alpha, \beta, \mu=1} \Lambda_\eta^{\alpha\beta\eta} \mathcal{A}_\alpha \mathcal{A}_\beta^* \mathcal{A}_\mu e^{-i\bar{\omega}_{\alpha\beta\mu\eta} t} + \frac{1}{2} \Delta\omega_\eta \mathcal{F}_\eta e^{-i(\Omega_0 - \omega_\eta)t} \quad (1.13)$$

Expression (1.13) appears with a set of coefficients and new magnitudes. \mathcal{A}_η a rescaled amplitude measuring number of photons. $\Delta\omega_\alpha$ corresponds to the modal bandwidth related to the modal photon lifetime, hence this term corresponds to the cavity losses. \mathcal{F}_α is the external pumping term, being Ω_0 its frequency. An external pumping is needed in order to generate the frequency comb, this factor quantifying how it interacts with the WGM. g_0 is called the four wave mixing reference gain. Finally $\Lambda_\eta^{\alpha\beta\eta}$ is the intermodal coupling factor, a term involving how the 4 modes for each differential equation encompassed in Eq. (1.13) are coupled. The complex exponential oscillates according to $\bar{\omega}_{\alpha\beta\mu\eta}$, which receives the name of molda fourwave mixing frequency detuning These parameters are deeper explained in [12]

The modal expansion allows to explain physically the emergence of frequency combs. Due to \vec{P}_{NL} each differential equation composing the set of equations (1.13) contains the term

$$\sum_{\alpha, \beta, \mu=1} \Lambda_\eta^{\alpha\beta\eta} \mathcal{A}_\beta \mathcal{A}_\gamma^* \mathcal{A}_\delta e^{-i\bar{\omega}_{\alpha\beta\mu\eta} t} \quad (1.14)$$

responsible for the contribution to the dynamics of \mathcal{A}_η . To have an effective interaction among modes, these need to be in resonance condition, thus the complex exponential has to oscillate slower

than the time scale of the dynamics in order to not vanish in average the interaction. The modal four wave mixing frequency detuning reads

$$\bar{\omega}_{\alpha,\beta,\mu,\eta} = \omega_{\alpha} - \omega_{\beta} + \omega_{\mu} - \omega_{\eta} \quad (1.15)$$

The ideal resonance condition occurs for $\bar{\omega}_{\alpha,\beta,\mu,\eta} = 0$. The four wave mixing process is viewing this interplay of modes as a photon creation/anihilation process, that is able to excite unpopulated states. The previous condition precisely states energy and angular momentum conservation of the involved photons.

$$\begin{aligned} \hbar\omega_{\alpha} + \hbar\omega_{\mu} &= \hbar\omega_{\beta} + \hbar\omega_{\eta} \\ l_{\alpha} + l_{\mu} &= l_{\beta} + l_{\eta} \end{aligned} \quad (1.16)$$

There are many possible combinations of \mathcal{A}_x , dividing them in two cases, either $\alpha \neq \mu \neq \beta \neq \eta$ (not degenerated) or $\alpha = \mu \neq \beta \neq \eta$ (Degenerated). Figure 1.7 summerizes this process including the two cases.

The series expansion provides analytical results such as the threshold for frequency comb generation. To generate a qualitative idea of the role taken by FWM mechanism it has to bear in mind that both degenerated and non-degenerated process involve 3 to 4 coupled differential equations. Initially only the pumping frequency from the laser (coupled to the cavity) is non zero, hence it is only possible to have 2 photons of the same mode to get involved in the generation of new frequencies, i.e. degenerated case. Quantum fluctuations in the no-photon modes make that at a certain pumping threshold to have $d\mathcal{A}/dt > 0$ for these new frequencies. In this way the new populated modes can mix with previous to yield new populations. This happens sequentially and the microresonator is outcoming a combination of frequencies.

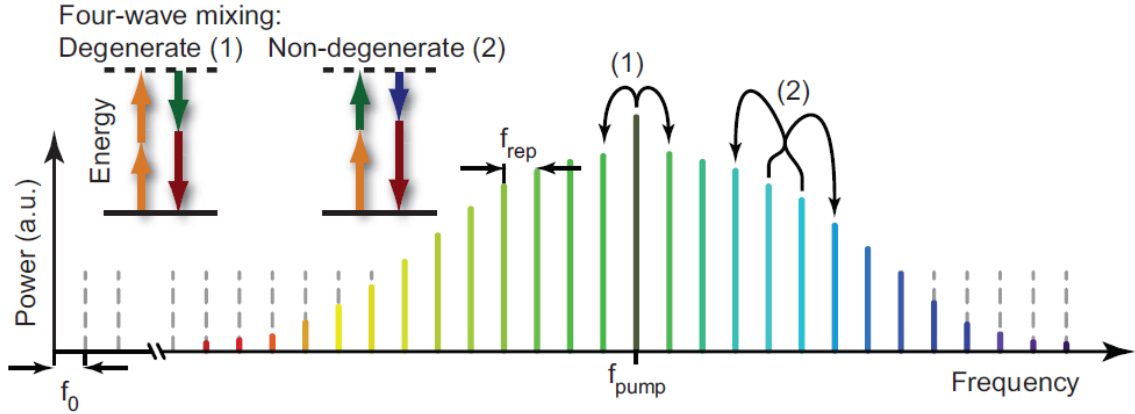


Figure 1.7: Illustration of both degenerated (1) and non-degenerated (2) FWM processes in the frequency comb generation [11].

1.3 Noise in microresonator based frequency combs

Shortly after the generation of microresonator based frequency combs, the existence of noise has been reported and intimately linked to these spectrums. Potential noise mechanisms considered are thermorefractive noise, thermoelastic noise, thermal Brownian motion, photothermal noise, laser phase noise and quantum noise [13]. These can be characterized from the microcavity point of view. Nevertheless the problem seems to be universal and independent of the experimental set up. Moreover parameters such as intracavity intensity or detuning seems to play an important role in its performance.

Noise outcomes are basically two; broadening of frequency comb peaks, and noise in the spacing between peaks. There has been experimental works describing it. Experimentally noise properties are studied along heterodyne beatnotes and **RF beatnote detections**. heterodyne beatnote detects broadening in frequency comb lines meanwhile RF beatnote (see Figure 1.8) detects noise in comb line spacing.

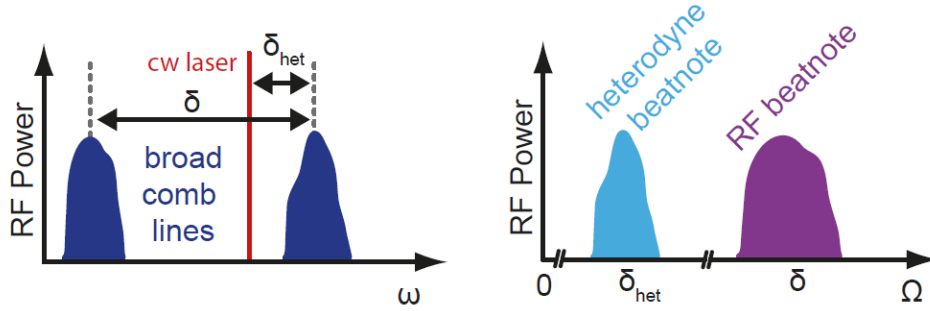


Figure 1.8: Noise detection in frequency combs. A broad frequency comb is captured by a broad heterodyne beatnote. A noise in spacing between comb lines is captured by RF beatnote through a cw laser [13].

The broadening of frequency peaks is a big issue, mainly because distorts the precision of these peaks and in the worst scenario destroy the frequency comb. Figures 1.10, 1.9 show obtained spectrums from different microcavities and the effect of noise in the detection measurements.

This master thesis deals with the numerical characterization of the noise effect in spectrum, adding (from the numerical stochastic point of view) additive and multiplicative noise, and a further discuss of both within its physical interpretation will be include. To accomplish this task a nonlinear model will be obtained which in fact coincides with the **Lugiato Lefever Equation (LLE)** in the context of temporal systems.

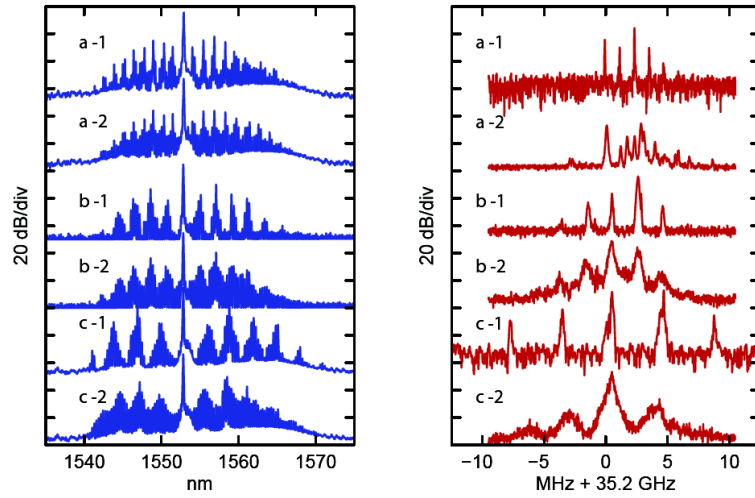


Figure 1.9: Frequency comb spectra generated in a MgF_2 resonator (blue) within RF beat notes (red). In this case the pump power increases from 50 to 200 mW. Each comb (a,b,c) are shown in early stage (a-1,b-1,c-1), and after increasing the intracavity power (reducing detuning). Broadening and collapse of peaks are shown. [13].

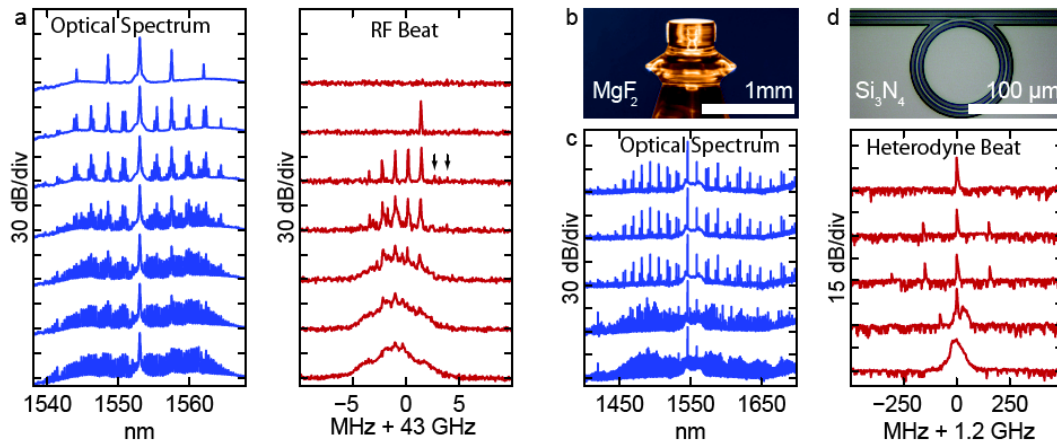


Figure 1.10: **a** Evolution of optical frequency comb in a MgF_2 microresonator within a picture in **b**. The RF beatnote evolves while reducing the detuning between laser and cavity resonance. **b** As in (a) but for a Si_3N_4 microresonator (shown in **d**) including now a heterodyne beat note measurement also varying the detuning. The appearance, broadening and collapse of peaks is a consequence indicating an increasing in noise [13].

Chapter 2

Modeling

2.1 A spatio-temporal representation

The laws of physics in kerr micro optical cavities yielded the set of coupled ODEs (1.13). The nonlinear multi-mode competition it establishes can be tracked numerically, since the system remains intractable to be fully solved purely by analytical approach. Nevertheless the numerical complexity due to the FWM processes cause the computation time to increase in a cubic power fashion with the number of modes [12]. A comb with 200 modes requires few days of simulation for a regular laptop.

Spatio temporal models have provided good results for mode locked lasers [14]. These determine the evolution of the mode amplitudes as a single spatio-temporal field. Hence implying less costly computational schemes. Besides it successfully predicted comb generation through mode-locking and pulse formation. This section is devoted to the derivation of such equivalent model for kerr-comb generation in WGMR [15] and the related approximations. As starting point the modal expansion in the following notation,

$$\begin{aligned} \frac{d\mathcal{A}_l}{dt} = & -\frac{1}{2}\Delta\omega_{l_0}\mathcal{A}_l + \frac{1}{2}\Delta\omega_{l_0}\mathcal{F}_l \exp\{i(\Omega_0 - \omega_{l_0})t\}\delta(l - l_0) \\ & - ig_0 \sum_{l_\alpha, l_\beta, l_\eta} \Lambda_l^{l_\alpha, l_\beta, l_\eta} \mathcal{A}_{l_\alpha} \mathcal{A}_{l_\beta}^* \mathcal{A}_{l_\eta} e^{i(\omega_{l_\alpha} - \omega_{l_\beta} + \omega_{l_\eta} - \omega_l)t} \delta(l_\alpha - l_\beta + l_\eta - l) \end{aligned} \quad (2.1)$$

The kronecker deltas are included to stress the driving field only excites the nearest mode to its frequency, noted by l_0 and considering the FWM process only taking place for the ideal resonance condition. Following the toroidal symmetry, eigenfrequencies can be expanded in a Taylor series around the central mode l_0 ,

$$\omega_l = \omega_{l_0} + \sum_{n=1}^N \frac{\xi_n}{n!} (l - l_0)^n \quad (2.2)$$

A similar approach is adopted for the coupling term, in this case simply retaining up to linear order in $l, l_\alpha, l_\eta, l_\beta$ around l_0 . Implicitly only valid in a neighbourhood of l_0 .

$$\Lambda_l^{l_\alpha, l_\beta, l_\eta} \approx 1 + \eta_l (l - l_0) + \eta_{l_\alpha} (l_\alpha - l_0) + \eta_{l_\beta} (l_\beta - l_0) + \eta_{l_\eta} (l_\eta - l_0) \quad (2.3)$$

The **spatio temporal varying envelope** can be casted as the inverse fourier transform of all amplitude modes in the toroidal domain.

$$\mathcal{A}(\theta, t) = \sum_l \mathcal{A}_l(t) \exp \{i(\omega_l - \omega_{l_0})t - i(l - l_0)\theta\} \quad (2.4)$$

In pursuance of the equation governing this spatio temporal envelope we perform the temporal derivative

$$\frac{\partial \mathcal{A}(\theta, t)}{\partial t} = \sum_l \left[\frac{d\mathcal{A}_l(t)}{dt} + i(\omega_l - \omega_{l_0}) \mathcal{A}_l(t) \right] \exp \{i(\omega_l - \omega_{l_0})t - i(l - l_0)\theta\} \quad (2.5)$$

For the sake of clarity it is convenient to split this expression in two terms to work independently,

$$\frac{\partial \mathcal{A}}{\partial t} = \frac{\partial \mathcal{A}^{(1)}}{\partial t} + \frac{\partial \mathcal{A}^{(2)}}{\partial t} \quad (2.6)$$

$$\frac{\partial \mathcal{A}^{(1)}}{\partial t} = \sum_l \frac{d\mathcal{A}_l(t)}{dt} \exp \{i(\omega_l - \omega_{l_0})t - i(l - l_0)\theta\} \quad (2.7)$$

$$\frac{\partial \mathcal{A}^{(2)}}{\partial t} = \sum_l i(\omega_l - \omega_{l_0}) \exp \{i(\omega_l - \omega_{l_0})t - i(l - l_0)\theta\} \quad (2.8)$$

First inserting the individual amplitude rates from the set (1.13) into $\partial \mathcal{A}^{(1)}/\partial t$ yields a series over l ,

$$\begin{aligned} & \sum_l \frac{d\mathcal{A}_l}{dt} e^{[i(\omega_l - \omega_{l_0})t - i(l - l_0)\theta]} = \\ & \sum_l \left\{ -\frac{1}{2} \Delta\omega_{l_0} \mathcal{A}_l e^{[i(\omega_l - \omega_{l_0})t - i(l - l_0)\theta]} + \frac{1}{2} \Delta\omega_{l_0} \mathcal{F}_l e^{i(\Omega_0 - \omega_{l_0})t} e^{-i(l - l_0)\theta} \delta(l - l_0) \right. \\ & \left. - ig_0 \sum_{l_m, l_\beta, l_\eta} \Lambda_l^{l_\alpha, l_\beta, l_\eta} \mathcal{A}_{l_m} \mathcal{A}_{l_\beta}^* \mathcal{A}_{l_\eta} e^{[i(\omega_{l_m} - \omega_{l_\beta} + \omega_{l_\eta} - \omega_{l_0})t]} e^{-i(l - l_0)\theta} \delta(l_m - l_n + l_\eta - l) \right\} \end{aligned} \quad (2.9)$$

Where the term including the coupling factor $\Lambda_l^{l_m l_l l_\eta}$ expands,

$$\begin{aligned}
& -ig_0 \sum_l \sum_{l_m, l_\beta, l_\eta} \Delta_l^{l_\alpha, l_\beta, l_\eta} \mathcal{A}_{l_\alpha} \mathcal{A}_{l_\beta}^* \mathcal{A}_{l_\eta} e^{[i(\omega_{l_\alpha} - \omega_{l_\beta} + \omega_{l_\eta} - \omega_{l_0})t]} e^{-i(l-l_0)\theta} \delta(l_\alpha - l_n + l_\eta - l) = \\
& -ig_0 \sum_l \sum_{l_\alpha, l_\beta, l_\eta} \mathcal{A}_{l_\alpha} \mathcal{A}_{l_\beta}^* \mathcal{A}_{l_\eta} e^{[i(\omega_{l_\alpha} - \omega_{l_\beta} + \omega_{l_\eta} - \omega_{l_0})t]} e^{-i(l-l_0)\theta} \delta(l_\alpha - l_n + l_\eta - l) + \\
& -ig_0 \eta_l \sum_l \sum_{l_\alpha, l_\beta, l_\eta} (l - l_0) \mathcal{A}_{l_\alpha} \mathcal{A}_{l_\beta}^* \mathcal{A}_{l_\eta} e^{[i(\omega_{l_\alpha} - \omega_{l_\beta} + \omega_{l_\eta} - \omega_{l_0})t]} e^{-i(l-l_0)\theta} \delta(l_\alpha - l_n + l_\eta - l) + \quad (2.10) \\
& -2ig_0 \eta_{l_\alpha} \sum_l \sum_{l_\alpha, l_\beta, l_\eta} (l_\alpha - l_0) \mathcal{A}_{l_\alpha} \mathcal{A}_{l_\beta}^* \mathcal{A}_{l_\eta} e^{[i(\omega_{l_\alpha} - \omega_{l_\beta} + \omega_{l_\eta} - \omega_{l_0})t]} e^{-i(l-l_0)\theta} \delta(l_\alpha - l_n + l_\eta - l) + \\
& -ig_0 \eta_{l_\beta} \sum_l \sum_{l_\alpha, l_\beta, l_\eta} (l_\beta - l_0) \mathcal{A}_{l_\alpha} \mathcal{A}_{l_\beta}^* \mathcal{A}_{l_\eta} e^{[i(\omega_{l_\alpha} - \omega_{l_\beta} + \omega_{l_\eta} - \omega_{l_0})t]} e^{-i(l-l_0)\theta} \delta(l_\alpha - l_n + l_\eta - l)
\end{aligned}$$

The presence of the common $\delta(x)$ factor involves a contraction on the sum over l index due to the fact that for each set of given indexes $\{l_\alpha, l_\beta, l_\eta\}$ only the term $l = l_\alpha - l_\beta + l_\eta$ is non-vanishing.

$$\sum_l \sum_{l_\alpha, l_\beta, l_\eta} (\dots) \delta(l_\alpha - l_\beta + l_\eta - l) = \sum_{l_\alpha, l_\beta, l_\eta} (\dots) \quad (2.11)$$

The resulting g_0 series is,

$$\begin{aligned}
& -ig_0 \sum_{l_\alpha, l_\beta, l_\eta} \mathcal{A}_{l_\alpha} \mathcal{A}_{l_\beta}^* \mathcal{A}_{l_\eta} e^{[i(\omega_{l_\alpha} - \omega_{l_\beta} + \omega_{l_\eta} - \omega_{l_0})t - i(l_\alpha - l_\beta + l_\eta - l_0)\theta]} \Delta_l^{l_\alpha, l_\beta, l_\eta} = \\
& -ig_0 \sum_{l_\alpha, l_\beta, l_\eta} \mathcal{A}_{l_\alpha} \mathcal{A}_{l_\beta}^* \mathcal{A}_{l_\eta} e^{[i(\omega_{l_\alpha} - \omega_{l_\beta} + \omega_{l_\eta} - \omega_{l_0})t - i(l_\alpha - l_\beta + l_\eta - l_0)\theta]} + \\
& -ig_0 \eta_l \sum_{l_\alpha, l_\beta, l_\eta} (l_\alpha - l_\beta + l_\eta - l_0) \mathcal{A}_{l_\alpha} \mathcal{A}_{l_\beta}^* \mathcal{A}_{l_\eta} e^{[i(\omega_{l_\alpha} - \omega_{l_\beta} + \omega_{l_\eta} - \omega_{l_0})t - i(l_\alpha - l_\beta + l_\eta - l_0)\theta]} + \quad (2.12) \\
& -2ig_0 \eta_{l_\alpha} \sum_{l_\alpha, l_\beta, l_\eta} (l_\alpha - l_0) \mathcal{A}_{l_\alpha} \mathcal{A}_{l_\beta}^* \mathcal{A}_{l_\eta} e^{[i(\omega_{l_\alpha} - \omega_{l_\beta} + \omega_{l_\eta} - \omega_{l_0})t - i(l_\alpha - l_\beta + l_\eta - l_0)\theta]} + \\
& -ig_0 \eta_{l_\beta} \sum_{l_\alpha, l_\beta, l_\eta} (l_\beta - l_0) \mathcal{A}_{l_\alpha} \mathcal{A}_{l_\beta}^* \mathcal{A}_{l_\eta} e^{[i(\omega_{l_\alpha} - \omega_{l_\beta} + \omega_{l_\eta} - \omega_{l_0})t - i(l_\alpha - l_\beta + l_\eta - l_0)\theta]}
\end{aligned}$$

From the previous 4 terms it is simple to distinguish the following spatiotemporal relations,

$$-i |\mathcal{A}|^2 \mathcal{A} = -i \sum_{l_\alpha, l_\beta, l_\eta} \mathcal{A}_{l_\alpha} \mathcal{A}_{l_\beta}^* \mathcal{A}_{l_\eta} e^{[i(\omega_{l_\alpha} - \omega_{l_\beta} + \omega_{l_\eta} - \omega_{l_0})t - i(l_\alpha - l_\beta + l_\eta - l_0)\theta]} \quad (2.13)$$

$$- \eta_{l_\beta} \mathcal{A}^2 \frac{\partial \mathcal{A}^*}{\partial \theta} = -i \eta_{l_\beta} \sum_{l_\alpha, l_\beta, l_\eta} (l_\beta - l_0) \mathcal{A}_{l_\alpha} \mathcal{A}_{l_\beta}^* \mathcal{A}_{l_\eta} e^{[i(\omega_{l_\alpha} - \omega_{l_\beta} + \omega_{l_\eta} - \omega_{l_0})t - i(l_\alpha - l_\beta + l_\eta - l_0)\theta]} \quad (2.14)$$

$$\eta_l \frac{\partial (|\mathcal{A}|^2 \mathcal{A})}{\partial \theta} = -i \eta_l \sum_{l_\alpha, l_\beta, l_\eta} (l_\alpha - l_\beta + l_\eta - l_0) \mathcal{A}_{l_\alpha} \mathcal{A}_{l_\beta}^* \mathcal{A}_{l_\eta} e^{[i(\omega_{l_\alpha} - \omega_{l_\beta} + \omega_{l_\eta} - \omega_{l_0})t - i(l_\alpha - l_\beta + l_\eta - l_0)\theta]} \quad (2.15)$$

$$\eta_{l_\alpha} |\mathcal{A}|^2 \frac{\partial \mathcal{A}}{\partial \theta} = \eta_{l_\eta} |\mathcal{A}|^2 \frac{\partial \mathcal{A}}{\partial \theta} = -i \eta_{l_\alpha} \sum_{l_\alpha, l_\beta, l_\eta} (l_\alpha - l_0) \mathcal{A}_{l_\alpha} \mathcal{A}_{l_\beta}^* \mathcal{A}_{l_\eta} e^{[i(\omega_{l_\alpha} - \omega_{l_\beta} + \omega_{l_\eta} - \omega_{l_0})t - i(l_\alpha - l_\beta + l_\eta - l_0)\theta]} \quad (2.16)$$

The remaining term to be analyzed from expression (2.9) is another spatio temporal term

$$-\frac{1}{2} \Delta \omega_{l_0} \sum_l \mathcal{A}_l(t) \exp [i(\omega_l - \omega_{l_0})(l - l_0)] = -\frac{1}{2} \Delta \omega_{l_0} \mathcal{A} \quad (2.17)$$

Gathering everything up

$$\begin{aligned} \frac{\partial \mathcal{A}^{(1)}}{\partial t} = & -\frac{1}{2} \Delta \omega_{l_0} \mathcal{A} + g_0 \left(-i |\mathcal{A}|^2 \mathcal{A} + \eta_l \frac{\partial (|\mathcal{A}|^2 \mathcal{A})}{\partial \theta} - \eta_{l_\beta} \mathcal{A}^2 \frac{\partial \mathcal{A}^*}{\partial \theta} + 2\eta_{l_m} |\mathcal{A}|^2 \frac{\partial \mathcal{A}}{\partial \theta} \right) \\ & + \frac{1}{2} \omega_{l_0} \mathcal{F}_{l_0} \exp \{i(\Omega_0 - \omega_{l_0})t\} \end{aligned} \quad (2.18)$$

The analysis for the term (2.8) is straightforward. Using Eq. (2.2) let expressing

$$\frac{\partial \mathcal{A}^{(2)}}{\partial t} = i \sum_l \left(\sum_{n=1}^N \frac{\xi_n}{n!} (l - l_0)^n \right) \mathcal{A}_l(t) \exp \{i(\omega_l - \omega_{l_0})t - i(l - l_0)\theta\} \quad (2.19)$$

Separately, one performs the spatial derivative of the spatio-temporal expansion (2.4),

$$i^n \frac{\partial^n \mathcal{A}}{\partial \theta^n} = \sum_l (l - l_0)^n \mathcal{A}_l \exp \{i(\omega_l - \omega_{l_0})t - i(l - l_0)\theta\} \quad (2.20)$$

Hence exchanging sums in expression (2.19) it has the following more compact spatiotemporal expression

$$\frac{\partial \mathcal{A}^{(2)}}{\partial t} = \sum_{n=1}^N i^{n+1} \frac{\xi_n}{n!} \frac{\partial^n \mathcal{A}}{\partial \theta^n} \quad (2.21)$$

Finally the resulting evolution for $\mathcal{A}(t)$ is

$$\begin{aligned} \frac{\partial \mathcal{A}}{\partial t} = & -\frac{1}{2}\Delta\omega_{l_0}\mathcal{A} + g_0 \left(-i|\mathcal{A}|^2\mathcal{A} + \eta_l \frac{\partial(|\mathcal{A}|^2\mathcal{A})}{\partial\theta} - \eta_\beta \mathcal{A}^2 \frac{\partial \mathcal{A}^*}{\partial\theta} + 2\eta_\alpha |\mathcal{A}|^2 \frac{\partial \mathcal{A}}{\partial\theta} \right) \\ & + \frac{1}{2}\omega_{l_0}\mathcal{F}_{l_0} \exp\{i(\Omega_0 - \omega_{l_0})t\} + \sum_{n=1}^N i^{n+1} \frac{\xi_n}{n!} \frac{\partial^n \mathcal{A}}{\partial\theta^n} \end{aligned} \quad (2.22)$$

This is a general expression. First of all, the span of the spectrum is not infinite and the eigenfrequency Taylor expansion can have a low cut off. It is the case when $l \approx l_0$ is a valid approximation such that $\xi_n \forall n \geq 3$ can be neglected. Within a heavier approximation in the coupling factor assuming $\Lambda_l^{l_\beta l_m l_n} \approx 1$ it reads

$$\frac{\partial \mathcal{A}}{\partial t} + \xi_1 \frac{\partial \mathcal{A}}{\partial \theta} = -\frac{1}{2}\Delta\omega_{l_0}\mathcal{A} - ig_0 |\mathcal{A}|^2 \mathcal{A} + \frac{1}{2}\omega_{l_0}\mathcal{F}_{l_0} \exp\{i(\Omega_0 - \omega_{l_0})t\} - i\frac{\xi_2}{2} \frac{\partial \mathcal{A}^2}{\partial\theta^2} \quad (2.23)$$

This is the desired final approximation. The notation can be compacted by further transformations. First noting $\sigma = \Omega_0 - \omega_{l_0}$ and performing the transformation $\mathcal{A} \rightarrow \mathcal{A} \exp(i\sigma t)$ the oscillating dependence on σ is removed. Thereafter the group velocity dependence is also removed making the transformation $\theta \rightarrow \theta - (\xi_1 t \bmod [2\pi])$.

$$\begin{aligned} \implies \frac{\partial \mathcal{A}}{\partial t} + \xi_1 \frac{\partial \mathcal{A}}{\partial \theta} - i\sigma \mathcal{A} = & -\frac{1}{2}\Delta\omega_{l_0}\mathcal{A} - ig_0 |\mathcal{A}|^2 \mathcal{A} + \frac{1}{2}\omega_{l_0}\mathcal{F}_{l_0} - i\frac{\xi_2}{2} \frac{\partial \mathcal{A}^2}{\partial\theta^2} \\ \implies \left(\frac{\partial \mathcal{A}}{\partial t} - \xi_1 \frac{\partial \mathcal{A}}{\partial \theta} \right) + \xi_1 \frac{\partial \mathcal{A}}{\partial \theta} - i\sigma \mathcal{A} = & -\frac{1}{2}\Delta\omega_{l_0}\mathcal{A} - ig_0 |\mathcal{A}|^2 \mathcal{A} + \frac{1}{2}\omega_{l_0}\mathcal{F}_{l_0} - i\frac{\xi_2}{2} \frac{\partial \mathcal{A}^2}{\partial\theta^2} \\ \implies \frac{\partial \mathcal{A}}{\partial t} = & -\frac{1}{2}\Delta\omega_{l_0}\mathcal{A} + i\sigma \mathcal{A} - ig_0 |\mathcal{A}|^2 \mathcal{A} + \frac{1}{2}\omega_{l_0}\mathcal{F}_{l_0} - i\frac{\xi_2}{2} \frac{\partial \mathcal{A}^2}{\partial\theta^2} \end{aligned} \quad (2.24)$$

This equation can be rewritten in the form of the normalized **Lugiato-Lefever equation**

$$\frac{\partial \psi}{\partial \tau} = -(1 + i\alpha)\psi + i|\psi|^2\psi - i\frac{\beta}{2} \frac{\partial^2 \psi}{\partial \theta^2} + \psi_o \quad (2.25)$$

The first term on the right hand side describe cavity losses, α measures the cavity frequency detuning between the frequency of the input pump and the nearest cavity resonance. ∂_θ^2 models dispersion and the cubic term represents the interaction among modes. F corresponds to the input field which here is considered to be an homogeneous wave. New field envelope and time are consequence of rescaling such that $\psi = (2g_0/\Delta\omega_{l_0})^{1/2} \mathcal{A}^*$, $\tau = \Delta\omega_{l_0}t/2$. Dimensionless parameters are the frequency detuning $\alpha = -2\sigma/\Delta\omega_{l_0}$, the dispersion $\beta = -2\xi_2\Delta\omega_{l_0}$ and the external pump $\psi_o = (2g_0/\Delta\omega_{l_0})\mathcal{F}_{l_0}$. $\beta = 2$ is chosen and the dimensionless time parameter τ is noted back as t for the remainder thesis.

The LLE equation has been extensively mathematically studied, specially in the context of cavity solitons [16]. This previous work helps us to understand the emergence of frequency combs.

2.2 Linear stability analysis

The spatio temporal envelope representation allows to study the collective evolution of modes inside a cavity. In order to retrieve their individual information, recalling Eq. (2.4) the procedure would be to perform the fourier transform of the field. Linear analysis is an analytical tool usefull to determine, in parameter space, the stability or instability of individual fourier modes when studied as small perturbations around a stationary solution. Perturbations are considered small enough such that non linear terms can be neglected and a linearized differential equation describes the evolution. Therefore linearization is only valid until non linear terms come into play.

Through the development of this thesis the system under study is excited by a monochromatic electric plane wave. Thus the frequency comb is expected to grow from an homogeneous and stationary background. The equation needs to be linearized around solutions ψ_{sh} fulfilling $\partial_t \psi_{sh} = \partial_{\theta\theta} \psi_{sh} = 0$.

$$0 = -(1 + i\alpha) \psi_{sh} + i|\psi_{sh}|^2 \psi_{sh} + \psi_o \quad (2.26)$$

This is a cubic, complex, polynomial for ψ_{sh} . It is more appropriate to work with its amplitude, the **Intracavity Field** I_s parameter yielding the following relation

$$\psi_{sh} \psi_{sh}^* = I_s = \frac{\psi_o \psi_o^*}{1 + (\alpha - I_s)^2} \quad (2.27)$$

In the position to undertake the linearization of Eq. (2.25), ψ is complex so that the field is described by $Re(\psi)$, $Im(\psi)$ or rather by ψ and ψ^* . Without any simplification the following system describes completely the solution.

$$\begin{aligned} \partial_t \psi &= -(1 + i\alpha) \psi + i\partial_{xx} \psi + i|\psi|^2 \psi + \psi_o \\ \partial_t \psi^* &= -(1 - i\alpha) \psi^* - i\partial_{xx} \psi^* - i|\psi|^2 \psi^* + \psi_o^* \end{aligned} \quad (2.28)$$

ψ_o is removed from the system provided the following expression for perturbations; $\psi = (1 + A) \psi_{sh}$. A is the normalized deviation from ψ_{sh} . Thus

$$\begin{aligned} \psi_{sh} \partial_t A &= \psi_o - (1 + i(\alpha - I_s)) \psi_{sh} - (1 + i(\alpha - I_s)) A \psi_{sh} + \\ &+ i\psi_{sh} \partial_{xx} A + iI_s (A^* + A + A^2 + 2|A|^2 + |A|^2 A) \psi_{sh} \end{aligned} \quad (2.29)$$

It is noticeable that $\psi_o - (1 + i(\alpha - I_s)) \psi_{sh} = 0$ from Eq. (2.27). System (2.28) finally reads

$$\begin{aligned} \partial_t A &= -(1 + i(\alpha - I_s)) A + iI_s (A^* + A + A^2 + 2|A|^2 + |A|^2 A) + i\partial_{xx} A \\ \partial_t A^* &= -(1 - i(\alpha - I_s)) A^* - iI_s (A^* + A + (A^*)^2 + 2|A|^2 + |A|^2 A^*) - i\partial_{xx} A^* \end{aligned} \quad (2.30)$$

Linearizing is straightforward by means of neglecting cubic and square terms, assuming the order of A is small enough,

$$\partial_t \begin{pmatrix} A \\ A^* \end{pmatrix} = \begin{pmatrix} -(1 + i(\alpha - 2I_s)) + i\partial_{xx} & iI_s \\ -iI_s & -(1 - i(\alpha - 2I_s)) - i\partial_{xx} \end{pmatrix} \begin{pmatrix} A \\ A^* \end{pmatrix} \quad (2.31)$$

The trial solution for such systems is the exponential. Altogether with its derivatives result in

$$\begin{pmatrix} A \\ A^* \end{pmatrix} \propto \mathbb{1} e^{\lambda t} e^{ik\theta} \Rightarrow \partial_t \begin{pmatrix} A \\ A^* \end{pmatrix} \propto \lambda \begin{pmatrix} A \\ A^* \end{pmatrix}, \partial_{xx} \begin{pmatrix} A \\ A^* \end{pmatrix} \propto -k^2 \begin{pmatrix} A \\ A^* \end{pmatrix} \quad (2.32)$$

This defines an eigenvalue problem, whose solution comes by the determination of the characteristic polynomial

$$\lambda \begin{pmatrix} A \\ A^* \end{pmatrix} = \begin{pmatrix} -(1 + i(\alpha - 2I_s + k^2)) & iI_s \\ -iI_s & -(1 - i(\alpha - 2I_s + k^2)) \end{pmatrix} \begin{pmatrix} A \\ A^* \end{pmatrix} \quad (2.33)$$

$\lambda(k)$ are the temporal rates for modes with wavenumber k . They can be obtained by solving the characteristic polynomial

$$\lambda^2 + 2\lambda + \left(1 - I_s^2 + (\alpha - 2I_s + k^2)^2\right) = 0 \quad (2.34)$$

With two solutions corresponding to A, A^*

$$\lambda_{\pm} = -1 \pm \sqrt{I_s^2 - (\alpha - 2I_s + k^2)^2} \quad (2.35)$$

$\lambda_- < 0 \quad \forall k$. Any perturbation around ψ_{sh} described by this dispersion relation will decay (stable modes). On the other hand for λ_+ it is not longer the same. The **condition for instability** reads,

$$\lambda_+ > 0 \Rightarrow \sqrt{I_s^2 - (\alpha - 2I_s + k^2)^2} > 1 \Rightarrow I_s^2 - (\alpha - 2I_s + k^2)^2 > 1 \quad (2.36)$$

As it was stated before, stability relies on the system's parameters; α and I_s . In order to check the conditions that the discriminant $\Delta = I_s^2 - (\alpha - 2I_s + k^2)^2$ fullfils the previous condition, one can compute its maximum and constraint $\Delta(k_{max}) > \Delta(k) \quad \forall k$ to the critical condition (2.36) such that $\Delta(k_{max}) = 1$. The extremals of Δ are computed

$$\frac{d\Delta}{dk}(k^*) = -2(\alpha - 2I_s + (k^*)^2)(-2k^*) = 0 \quad (2.37)$$

There are 3 possibilities; $k_1 = 0$, $k_{2,3} = \pm\sqrt{2I_s - \alpha}$. When the second derivative evaluated at the point of interest is negative it is a maximum.

$$\frac{d^2\Delta}{dk^2}(k_1) = -4\alpha + 8I_s \quad (2.38)$$

$$\frac{d^2\Delta}{dk^2}(k_{2,3}) = 8\alpha - 16I_s \quad (2.39)$$

The condition for maximum $d^2\Delta/dk^2 < 0$ is exclusive for each k_1 and $k_{2,3}$ with transition at $\alpha = 2I_s$. Scheme (2.1) indicate which k is maximum for $\alpha - 2I_s$ values.

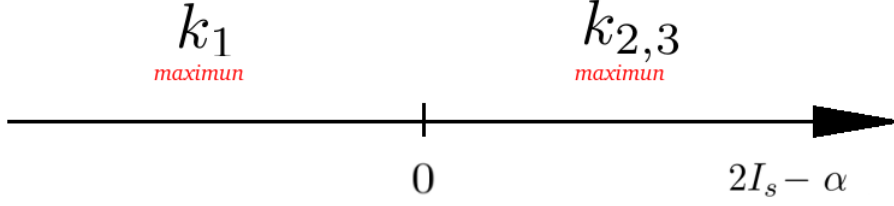


Figure 2.1: Parameter region where k_1 and $k_{2,3}$ are maximuns.

k_1 corresponds to an **homogeneous instability** while $k_{2,3}$ are symmetric wavenumbers which introduce a **pattern forming instability** according to their periodicity. Condition (2.36) establishes for which parameters the modes will grow as a consequence of any perturbation. The following addresses the thresholds to meet such instabilities and critical wavelengths.

$$\Delta(k_{2,3}) = I_s^2 \Rightarrow I_s^c = +1 \quad (2.40)$$

$$\Delta(k_1) = I_s^2 - (\alpha - 2I_s)^2 \Rightarrow (I_s^c)^2 - \frac{4}{3}\alpha^c I_s^c + \frac{((\alpha^c)^2 + 1)}{3} = 0 \quad (2.41)$$

As far as $k_{2,3}$ are the maximun, no matter the parameter α to present pattern forming instability with periodicity given by $k_c = \sqrt{\theta - 2}$. The requirements to encounter homogeneous instability ($k_c = 0$) are met on the curve (α^c, I_s^c) defined by the expression (2.41). Since it is a second order polynomial, the curve has two branches

$$I_{s\pm}^c = \frac{1}{3} \left(2\alpha \pm \sqrt{\alpha^2 - 3} \right) \quad (2.42)$$

It is easily verified that for I_{s+}^c k_1 is not maximun anymore ($2I_{s+}^c > \alpha$). Homogeneous instability can only develop on the negative branch. Figures (2.2) displays graphically this information.

Intracavity field is not necessary single valuated for all possible $\psi_0\psi_0^*$ taking into account Eq. (2.27) is cubic in I_s . For certain values of the pumping the equation provides three possible stationary solutions in a phenomena denoted by **bistability**. Physically such possibilities cannot exist at the same time. Through the linear stability analysis previously performed it can be proven that two of the solutions will always be unstable ($\lambda_+ > 0$ for some k) in case the system is found in this regime.

Bistability requires (2.27) to have to extremals respect to I_s . With $I_0 = \psi_0\psi_0^*$

$$I_o = I_s (1 + \alpha^2) + I_s^3 - 2\alpha I_s^2 \quad (2.43)$$

Looking for extremals

$$\begin{aligned} \frac{dI_o}{dI_s} &= 1 + \alpha^2 + 3I_s^2 - 4\alpha I_s = 0 \\ \implies I_s^2 - \frac{4}{3}\alpha I_s + \frac{(\alpha^2 + 1)}{3} &= 0 \end{aligned} \tag{2.44}$$

Exactly equivalent to the homogeneous instability threshold (2.41). In this case bistability requires to have 2 real solutions, which implies the condition $\alpha^2 > 3$, a result complementary to the previous analysis.

In the **monostable** regime plotted in Fig. 2.3 following Eq. (2.41), for $\alpha^2 < 3$ the homogeneous stationary solution is stable all the way to $I_s = 1$ because implicitly $\alpha < 2$, taking place the pattern forming instability.

On the other hand in the **bistable** regime plotted in Figure 2.4, if $\sqrt{3} < \alpha < 2$ the homogeneous stationary solution is stable all the way to $I_s = 1$ occurring the pattern forming instability and being the other two solutions unstable. If $\alpha > 2$, the homogeneous instability takes place at $I_{s-}(\alpha)$, once again being the other two solutions unstable. In this way bistability settles down a qualitative different mechanism leading to instability and pattern formation since homogeneous instability only happens in the bistable regime.

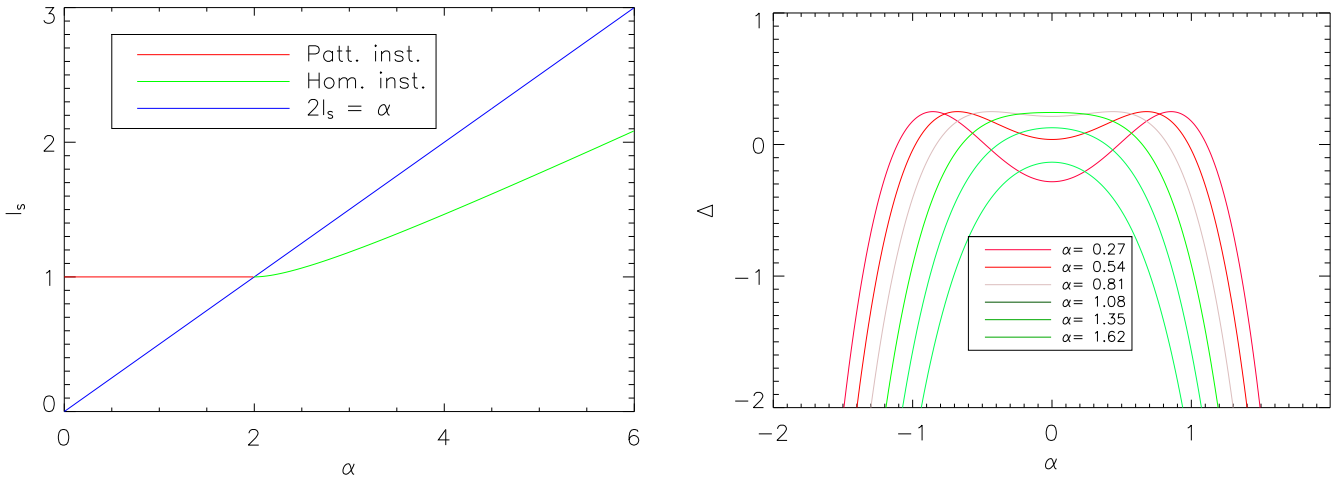


Figure 2.2: **Left** Thresholds for unstable homogeneous steady LLE solutions in parameter space. Blue line is the separation representing the domains from (2.1). **Right** Graphical transition from $k_{2,3} \rightarrow k_1$ maximum in discriminant $\Delta(k)$ for several detuning α parameter values. Evolution of maximas can be interpreted as a horizontal trajectory crossing the blue line at $I_s = 0.5$ from left figure, hence critical transition happens for $\alpha = 2I_s = 1$. To stress that $\Delta < 1$ thus all modes are stable.

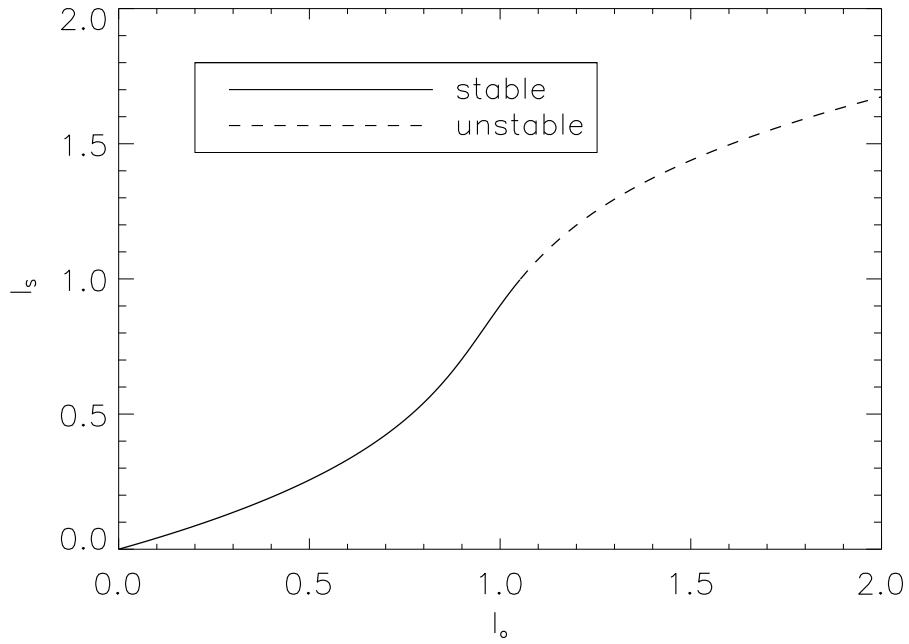


Figure 2.3: Monostable regime with $\alpha = \sqrt{3} - 0.5$. $I_c = 1$

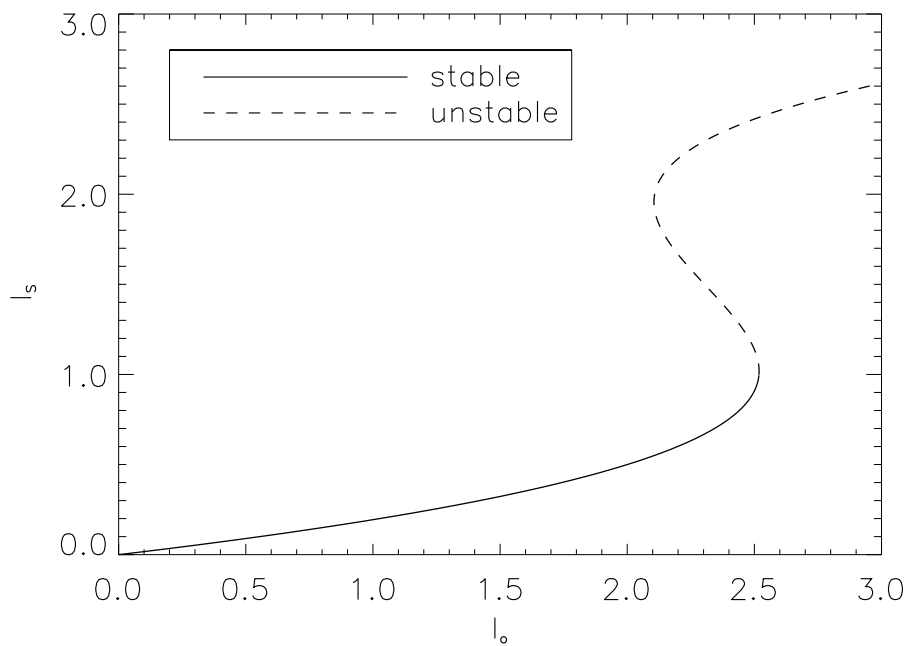


Figure 2.4: Bistable regime with $\alpha = \sqrt{3} + 0.5$. $I_c = I_{s-}^c (\alpha = \sqrt{3} + 0.5) \approx 1$ almost indistinguishable compared to Figure 2.3.

2.3 Characterization of noise excited sidebands

A fully analytical approach to Equation (2.25) is not affordable. In that context, exploring the patterns provided by the instabilities predicted in the previous section requires numerical integrations techniques. Results, that are presented in chapter 3 are split in two: **Deterministic Combs** and **Stochastic Combs**.

A deterministic comb is the pattern resulting from solving the Lugiato Lefever Equation without stochastic terms in an initially homogeneous background, under proper instability conditions. Provided small random fluctuations over the initial field, modes are excited and start growing based on their eigenvalue. The Fourier transform yields the frequency spectrum, integrated by the non-vanishing modes.

Stochastic terms, so far not included in the theoretical derivations, are introduced *a posteriori* according to phenomenological reasonings. Solving the LLE within these yields stochastic frequency combs. Theoretically, the main effect of noise is the damped excitation of modes aside to the main comb, modes called **Soft-Modes** [17]. These broaden the peaks with $k \neq 0$. **As main motivation for this work**, it has been recently discovered that this is no longer true in certain experimental set-ups, seen at Figure 2.5.

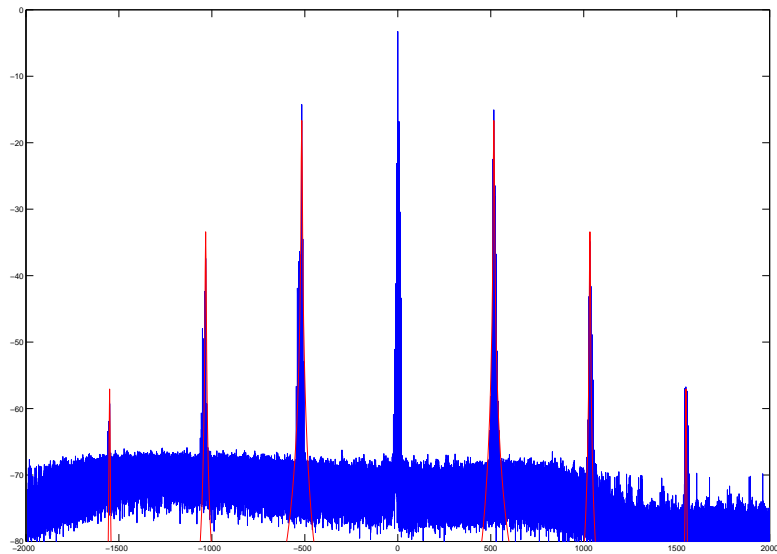


Figure 2.5: An experimental comb from experiments. Red curve correspond to theoretical prediction for soft modes, broadening comb peaks. Central peak is out of predictions. Background noise can correspond to experimental precision.

To that extent numerical integrations of stochastic combs will be adressed in an attempt to recover such kind of spectrums. The terms introduced match possible physical deviations from LLE elements. Hereafter some considered schemes will be mentioned and briefly discussed. In every case white noise, purely spatial, temporal or rather spatio temporal is involved.

$$\begin{aligned}
\mu(t) \quad | \quad & \langle \mu(t) \rangle = 0 \\
& \langle \mu(t) \mu(t') \rangle = \delta(t - t') \\
\\
\mu(\theta) \quad | \quad & \langle \mu(\theta) \rangle = 0 \\
& \langle \mu(\theta) \mu(\theta') \rangle = \delta(\theta - \theta') \\
\\
\mu(t, \theta) \quad | \quad & \langle \mu(t, \theta) \rangle = 0 \\
& \langle \mu(t, \theta) \mu(t', \theta') \rangle = \delta(\theta - \theta') \delta(t - t')
\end{aligned} \tag{2.45}$$

Fluctuations in the Electric field rates. Quantum fluctuations inside the WGMR may provoke modes at random to be excited by spontaneous creation and annihilation of photons, directly perturbing the spatio temporal field ψ . This can happen at any time at any place, independently from the current magnitude of the field. Hence it can be modeled by additive spatio temporal white noise

$$\begin{aligned}
\partial_t \psi^s &= \mu_0 \mu(t, \theta) \\
\implies \frac{\partial \psi}{\partial t} &= -(1 + i\alpha) \psi + i |\psi|^2 \psi - i \frac{\beta}{2} \frac{\partial^2 \psi}{\partial^2 \theta} + \psi_o + \mu_0 \mu(t, \theta)
\end{aligned} \tag{2.46}$$

Static fluctuations in the detunning parameter. Detuning parameter measures the difference between pumping frequency and the nearest cavity mode. Due to cavity imperfections, that modal frequency can fluctuate inside the resonator at any section of it. It would be a built-in property implying to be static in time. The structure of the equation leads to a multiplicative noise, hence these fluctuations affect more (less) those high (low) populated modes

$$\begin{aligned}
i\alpha\psi &\longrightarrow i\alpha\psi + i\mu_0\mu(\theta)\psi \\
\partial_t \psi^s &= i\mu_0\mu(\theta)\psi \\
\implies \frac{\partial \psi}{\partial t} &= -(1 + i\alpha) \psi + i |\psi|^2 \psi - i \frac{\beta}{2} \frac{\partial^2 \psi}{\partial^2 \theta} + \psi_o + i\mu_0\mu(\theta)\psi
\end{aligned} \tag{2.47}$$

Spatio-temporal multiplicative noise. Altogether with cavity imperfections, the presence of thermal fluctuations produces homogeneous thermal expansion/contraction along the WGMR size. These last fluctuations would be modeled using purely temporal multiplicative noise in the LLE. The combination of both yields the introduction of spatial-temporal multiplicative noise

$$\begin{aligned}
i\alpha\psi &\longrightarrow i\alpha\psi + i\mu(t, \theta)\psi \\
\partial_t \psi^s &= i\mu_0\mu(t, \theta)\psi \\
\implies \frac{\partial \psi}{\partial t} &= -(1 + i\alpha) \psi + i |\psi|^2 \psi - i \frac{\beta}{2} \frac{\partial^2 \psi}{\partial^2 \theta} + \psi_o + i\mu_0\mu(t, \theta)\psi
\end{aligned} \tag{2.48}$$

Static long wavelength fluctuations. These perturbations try to model the fact that perfect monochromatic light is not technically feasible. The pumping term is assumed to be monochromatic and wavelengths are described respect its value in the model. Long wavelength perturbations to this pumping, implies that the fourier spectrum of such is a decaying gaussian centered at the pumping wave peak ($k = 0$, after renormalizing variables). Taking the fourier transform of the pumping term

$$\begin{aligned}
\hat{F} &\propto \delta(k) \longrightarrow \hat{\mu}(k) e^{-\frac{k^2}{2\sigma^2}} \\
\partial_t \hat{\psi}_k^s &= \mu_0 \hat{\mu}(k) e^{-\frac{k^2}{2\sigma^2}} \\
\implies \frac{\partial \psi}{\partial t} &= -(1+i\alpha)\psi + i|\psi|^2\psi - i\frac{\beta}{2}\frac{\partial^2 \psi}{\partial^2 \theta} + \psi_o + \frac{\mu_0}{\sqrt{2\pi}} \int_{-\infty}^{+\infty} dk \hat{\mu}(k) e^{-\frac{k^2}{2\sigma^2}} e^{i2\pi k\theta}
\end{aligned} \tag{2.49}$$

Where $\hat{\mu}(k)$, $\partial_t \hat{\psi}_k^s$ are white noise and the contribution to the fourier mode k time evolution in fourier space, respectively.

Spatio-Temporal long wavelength fluctuations. This work will also explore the possibility that the laser frequency broadening changes in time.

$$\begin{aligned}
\hat{F} &\propto \delta(k) \longrightarrow \hat{\mu}(t, k) e^{-\frac{k^2}{2\sigma^2}} \\
\partial_t \hat{\psi}_k^s &= \mu_0 \hat{\mu}(t, k) e^{-\frac{k^2}{2\sigma^2}} \\
\implies \frac{\partial \psi}{\partial t} &= -(1+i\alpha)\psi + i|\psi|^2\psi - i\frac{\beta}{2}\frac{\partial^2 \psi}{\partial^2 \theta} + \psi_o + \frac{\mu_0}{\sqrt{2\pi}} \int_{-\infty}^{+\infty} dk \hat{\mu}(t, k) e^{-\frac{k^2}{2\sigma^2}} e^{i2\pi k\theta}
\end{aligned} \tag{2.50}$$

The numerical approaches to solve the LLE including these noise schemes are detailed in appendix chapter 5.

Chapter 3

Results

This chapter presents the solutions of LLE by means of a **pseudo spectral numerical method**. In a nutshell, the method translates the PDE problem into a set of coupled ordinary differential equations. To that extent the **fourier transform** of the equation is taken, in particular following the **discrete fourier transform (DFT)**, its numerical analogue. Each of these ODEs consists of a linear and a non-linear part. Hereafter the algorithm iteratively solves each fourier mode computing first the non-linear term in real space, being the linear part fully analytical solvable. The integration scheme is detailed in Appendix A.

As in any numerical technique, time and space are inevitably discretized, consequently the accessible fourier modes. Part of modeling WGMR relies on their circular symmetry approximation. This is built-in in the LLE (see Eq. 2.2). This symmetry is interpreted using **periodic boundary conditions** when solving the equation, which naturally introduces the discretization of resonator modes in the numerical model.

$$\psi(t, 0) = \psi(t, L) \tag{3.1}$$

Once defined the minimum wavenumber interval Δk (the free spectral range) the system size is determined

$$L = \lambda_{max} = \frac{2\pi}{f_r} \implies L = \frac{2\pi}{\Delta k} \tag{3.2}$$

Therefore, given the number of grid points N the minimum spatial interval comes by $\Delta x = L/N = (2\pi)/(N\Delta k)$. Patterns are expressed as $\psi\psi^*$, the square modulus of the complex field ψ . Likewise the frequency comb is obtained displaying the **power spectral density** of the resulting field fourier transform $\hat{\psi}\hat{\psi}^*$. Simulations are presented as follows: First the Deterministic Combs, showing the basic phenomena resulting from the linear analysis stability. Second, using those patterns as initial conditions the effect of fluctuations into the equation is depicted. Finally results that matches the experimental results are analyzed.

3.1 Deterministic Combs

The LLE equation is vastly rich in phenomena depending on its parameter space and the initial condition. For instance, for high values of I_s the appearance of chaotic behaviour is guaranteed [16]. This work restricts the dynamics to the parameter space around the critical conditions derived from the study of the linear regime done in chapter 2.2. Thus patterns are obtained slightly beyond the onset of instability delimited in Figure 2.2 using the steady homogeneous solutions as initial conditions.

Simulations take a time step $dt = 10^{-3}$ and the discretization contains $N = 1024$ points. Due to the use of DFT the numerical problem of **Aliasing** appears (see Appendix B). In order to avoid it, the system size given by Δk as free parameter has to be properly tuned for each set $\{I_s, \alpha\}$ with the purpose of covering all the meaningful frequencies (see page 31, first paragraph). Figures 3.1,3.2,3.3 are simulations carried out in the monostable regime with pattern forming instability $\theta < \sqrt{3}$, bistable regime with pattern forming instability $\sqrt{3} < \theta < 2$ and in the bistable regime with homogeneous instability $\theta > 2$, for which qualitative differences were found performing the linear analysis. In fourier space, to stress the individuality of fourier modes along to the representation by continuous lines, those are denoted by a diamond symbol. The power spectrums are symmetric around $k = 0$ because of the discrete fourier transform involves conjugated exponential terms.

Arrays of figures are intended to highlight the basic dynamics of the building process. Within the parameter region under study, the stationary state in every case corresponds to patterns whose DFT is **a set of isolated nonvanishing fourier modes**, legitimizing this mathematical framework for studying frequency combs. Evolution starts at $t = 0$ and runs until the stationary state is achieved. Such stationary state strongly depends on the number of interacting modes for a given detuning α value. More modes requires a longer time. Comparing simulation 3.1 with cases 3.2,3.3, a final different time was required to develop the isolated combs.

The final state is related with the dependence of f_r and the final power spectrum amplitude with α . Assuming I_s is essentially fixed for each α just beyond the instability region, characterizing such combs is a unidimensional problem. For instance, for any N such that the system can develop a valid frequency comb (see page 31, first paragraph) the number of comb peaks increases with a parallel enhancing in the detuning.

Along with the frequency comb it seems to exist a noisy background. Initially for times $t \approx 1-100$, it corresponds to the fluctuations in the initial condition, exciting in an homogeneous way the modes with $k \neq 0$. When the simulation is over it is associated to the **numerical precision** in the code scheme. Modes cannot be precisely described past that precision, remaining a fluctuating background. It does not have any physical meaning.

Figures 3.1,3.2,3.3 show dynamic information of the evolving modes. The most relevant is the dichotomy among the linear and non linear regime. The transition among both regimes takes place approximately when the pattern amplitude in real space (left column of figures 3.1,3.2,3.3) exceeds the threshold in which the forming pattern can be considered a perturbation to the smallest order to the steady homogeneous solution. There is a difference in time of two orders of magnitude in the appearance of such transition among the monostable regime, taking place at $t \approx 1000$, whereas for the other two these quickly go into the nonlinear behaviour at $t \approx 10$. On the mode side point of view the linear regime corresponds for the interval of time when modes evolve exponentially in time independent of each other according to $\lambda(k)$.

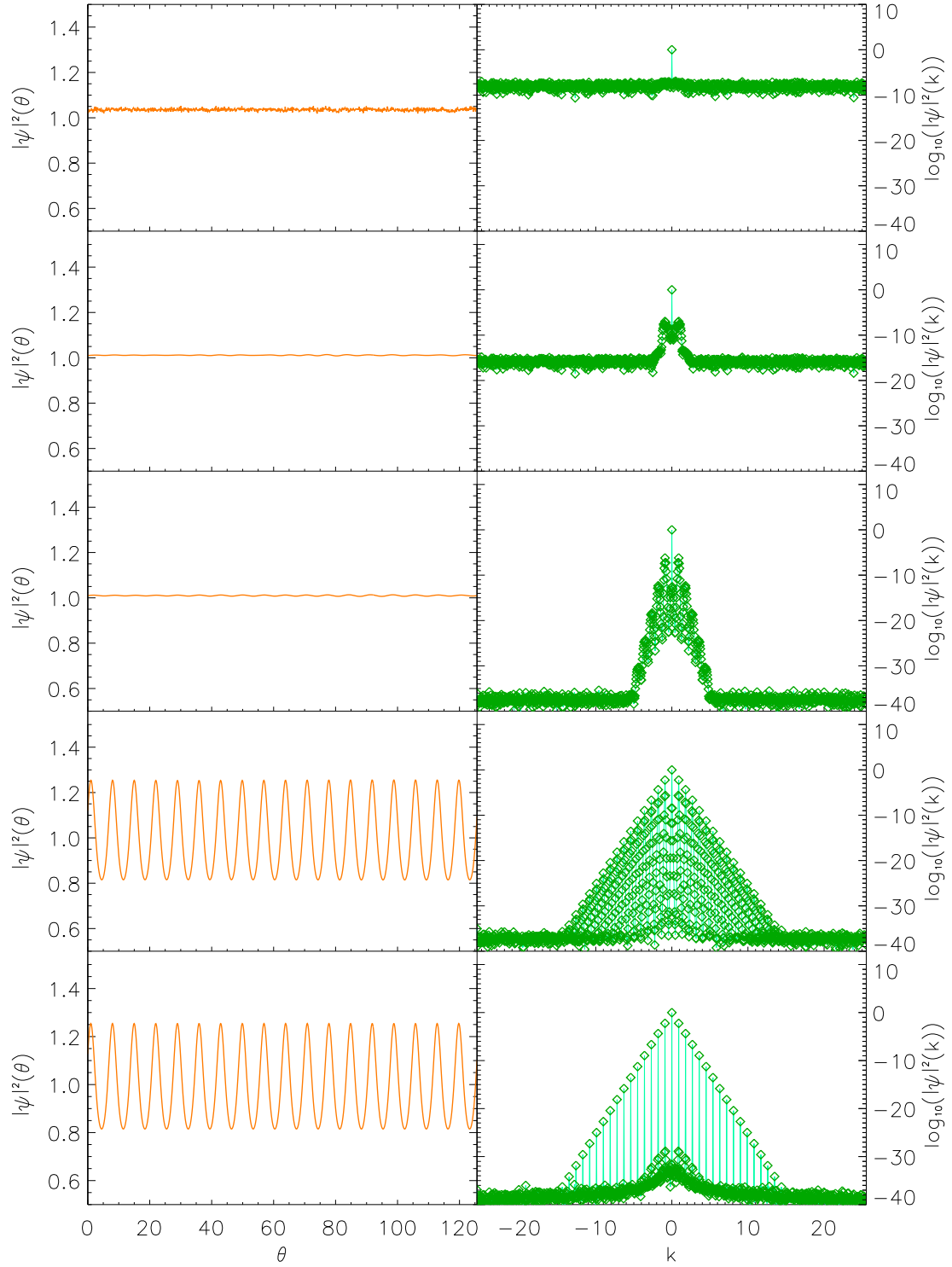


Figure 3.1: **(Left)** Pattern evolution from initial condition and **(Right)** resulting frequency comb. $\alpha = \sqrt{3} - 0.5$ (monostable regime with pattern forming instability), $I_s = 1.01$, $\Delta k = 0.05$. From top to bottom: $t = 1, 10, 100, 1000, 10000$.

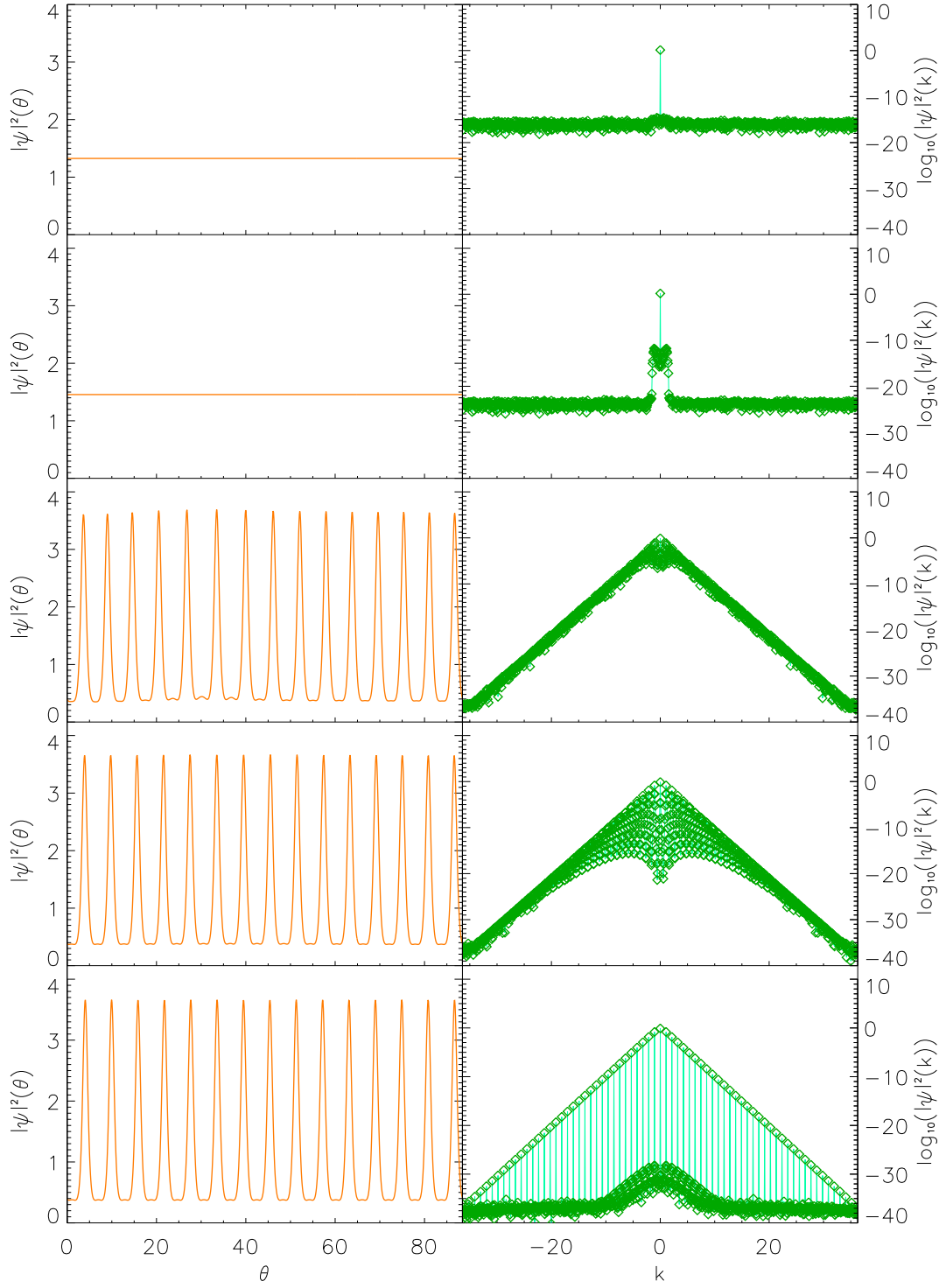


Figure 3.2: **(Left)** Pattern evolution from initial condition and **(Right)** resulting frequency comb. $\alpha = 1.8$ (bistable regime with pattern forming instability), $I_s = 1.01$, $\Delta k = 0.07$. From top to bottom: $t = 1, 10, 100, 1000, 40000$.

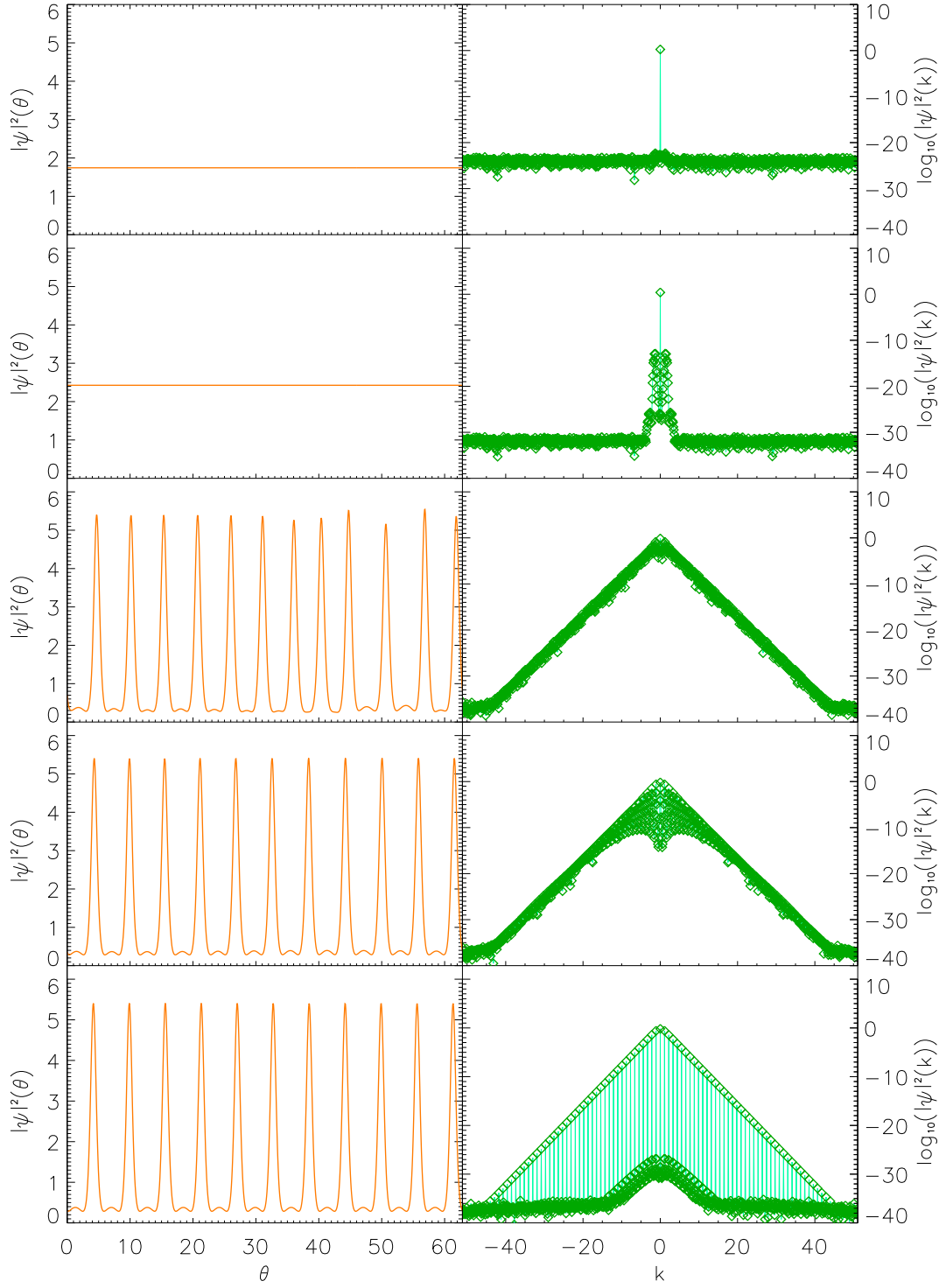


Figure 3.3: **(Left)** Pattern evolution from initial condition and **(Right)** resulting frequency comb. $\alpha = \sqrt{3} + 0.5$ (bistable regime with homogeneous instability), $I_s = 1.03$, $\Delta k = 0.1$. From top to bottom: $t = 1, 10, 100, 1000, 30000$.

Figure 3.4 displays the individual evolution of two given modes altogether with the linear approximation. During the linear regime, because the pattern is presented as $\log_{10}(\psi\psi^*)$, the spectrum resembles Fig. 2.2 so long as $\lambda(k) \in \mathbb{R}$. In case of $\lambda(k) \in \mathbb{C}$ by the same token modes evolve homogeneously with $\lambda(k) + \lambda^*(k) = -2$. Once the flat spectrum barrier constituted by $\lambda(k)$ declines up to approximately the bottom numerical frontier, the nonlinear behaviour emerges as a sudden collective dynamics of the **system meaningful modes**. Due to numerical precision the system has a number of modes that contributes to the system evolution given a set of parameters. These are those whose numerical amplitude is above such limit. The numerical precision considered in the simulations is double precision, i.e. 16 significative digits. Extra modes included just decay and do not participate in the process. Their real amplitude is below that limit indeed. Facing the problem of aliasing partly consists on choosing the system size (by means of Δk) such that it guarantees every mode will have an amplitude lying above the precision limit. As an example, at time $t = 10000$ Fig. 3.1 clearly shows that modes with $k \geq 15$ do not participate in any non-linear dynamics because the space discretization is too fine.

Thus the role of a particular scheme for Δk is of great importance as α changes. Computing the evolution of a limited number of modes implies having the priority that most of them play their role in the comb. As in the previous paragraph was noted, in Figure 3.1 there are many modes not participating in the dynamics, meanwhile the system size in Figure 3.2 seems to be perfectly tuned so that most of the modes are above the precision limit. This means Δk has to be set according to the system size that captures only those modes. To give insight into that question a systematic exploration of this quantity as function of α is carried out. Figure 3.6, (**top**), represents this result labeled as $L_{\Delta k}$. This quantity is the size of the domain in fourier space on which comb peaks develop around $k = 0$ above the noisy. Its meaning is restricted to the context of numerical modeling, otherwise infinite harmonics would participate. As follows the numerical method to retrieve such quantity is described. Considering the y-logscale representation, consecutive fourier modes contribute to the power spectrum with an exponential decay as long as $|k|$ increases. Using this property, fitting the comb peaks logarithm value to a straight line helps to establish that the system size corresponds twice the value of k resulting from crossing such line with the numerical precision limit. Twice because of the comb is symmetric around the homogeneous mode. The behaviour satisfies two regimes, for which the first one (involving $\alpha \in [0, 1.3]$ approximately) yields a soft linear decrease, meanwhile the second seems to follow a law of the kind $y = x^\nu, \nu < 1$, hence steadily increasing for higher detunings. As a consequence the system size $L_{\Delta k}$ or rather Δk is adjusted through Equation (3.2) to this result by means of a piecewise expression for Δk as function of α . The choice of this scheme is presented at the (**Top Inset**) in Fig. 3.6 and every next simulation is computed according to it.

With regard to the nonlinear regime, it emerges as a sudden collective excitation cascade that can be interpreted with the numerical appearance of the four wave mixing process detailed in the introduction. The power input through the homogeneous state flows equally towards all sideband frequencies thus exciting every frequency at instants already discussed when transition between linear-non linear regimes takes place. As the cascade process is over, the frequency amplitudes not belonging to the final stationary frequency comb start decaying. This decline is clearly depicted in Fig. 3.1 at time $t = 1000$ and it can be inferred from 3.2 and 3.3 at $t = 1000$ when it is starting. An alternative visualization for the dynamics described is displayed in panel 3.5 following the time evolution for each of the α used before. The first row exposes the dynamics for those modes whose discriminant is real, meanwhile the other two for those whose discriminant is pure imaginary. For $\alpha = \sqrt{3} - 0.5$ (**Top**) the chosen modes are about the limit of real eigenvalue, a transition occurring at $k = 1.340$. Thus it does not show the decay with $\lambda + \lambda^* = -2$ but with the eigenvalues studied in the

linear analysis approximation. The succeeding non linear regime is here depicted mainly as a sudden increase in amplitude followed by a generalized decay for the modes not belonging to the stationary frequency comb. When looking to the cases $\alpha = 1.8$ (**center**), $\alpha = \sqrt{3} + 5$ (**bottom**) the selected modes clearly lie outside the domain of purely real eigenvalue. Therefore initially the behaviour is purely driven by $\lambda = -2$ for all modes since the comb is displayed as the square modulus. It worths to stress that this linearity appears not as a linear curve due to the x-axis log-scale. As an extra observation, it can be observed how the linear regime spans for a narrower window time as α is increased. After the non-linear disruption the amplitude is constrained, finally decaying the comb peak's sidebands wavenumbers.

The property of an exactly fixed f_r is also tested. The finite number of modes makes f_r to present sudden increases/decreases when the number of modes between two consecutive comb peaks switches. The apparent continuous variation in the comb tooth spacing is due to the established functional dependence $\Delta k(\alpha)$. Therefore for each detuning the separation among modes is slightly different. Equation $k_c = \sqrt{2 - \alpha}$ predicts the first wavenumber being excited at the onset of instability. Figure 3.6 (**middle**) shows that in simulations it determines the comb spacing up to a limiting value of α . Nonetheless there is not in principle any theoretical consideration that after the non linear regime the frequency comb has to be composed of this frequency and its harmonics. This switch appears to be precisely at $\alpha = \sqrt{3}$, the transition among monostable-bistable regimes. Right after this transition the spacing steeply increases. Then it is kept constant to continuedly enter in a state where this magnitude is highly sensible on α , being able to shift among several values for really small differences in the detuning. Finally for $\alpha \approx 3$ the spectrum is not discrete anymore due to the appearance of chaotic behaviour in the field. To omit the increase in system size, Figure 3.6 (**bottom**) shows f_r but expressed just as the number of modes separating consecutive comb peaks. In this representation the big shift in the number of modes is due to the transition between "small system size" towards "great system size" lowering the density of meaningful comb peaks.

The requirement for a different final simulation time was accounted by the higher amount of participating modes involved as α increases. Nevertheless this time is different for a smaller detuning than other; $t = 40000$ against $t = 30000$. There is not a simple criteria for selecting this time, since patterns relatively fast evolves towards a definite state but their combs still evolves a great time more before achieving the complete stationary state, until modes not corresponding to comb peaks decays to the numerical precision limit. Several computational methods were tested to find such a criteria, as constraining the numerical computation while $\partial_t |\psi|^2 < tol$ where tol is an input parameter. But this number was not clearly determined. So that the way out was just introducing a time big enough to ensure the stationary state is obtained. Now the reason for $t = 40000$ at $\alpha = 1.8$ is partly due to the increase in $L_{\Delta k}$ as defined in Figure 3.6, the excess of time respect to the realization for $\alpha = \sqrt{3} - 0.5$ cannot be accounted exclusively to a higher amount of participating modes, since this quantity, $L_{\Delta k} f_r$, is even bigger for higher detunings. It suggests the presence of unknown effects at the bistable transition and during this regime, for $\alpha \in [\sqrt{3}, 2]$. So the election of simulation times when obtaining comb realizations is as follows; $t = 20000$ in the monostable regime, $t = 40000$ in the bistable regime, and $t = 30000$ when the pattern forming instability takes place.

Considering the patterns in real space, the periodicity is given by the excited mode with smallest wavenumber, the first non-homogeneous comb peak. Pattern structures begin to tighten as the total number of excited modes $\frac{L_{\Delta k}}{f_r}$ increases, i.e. with larger detuning values.

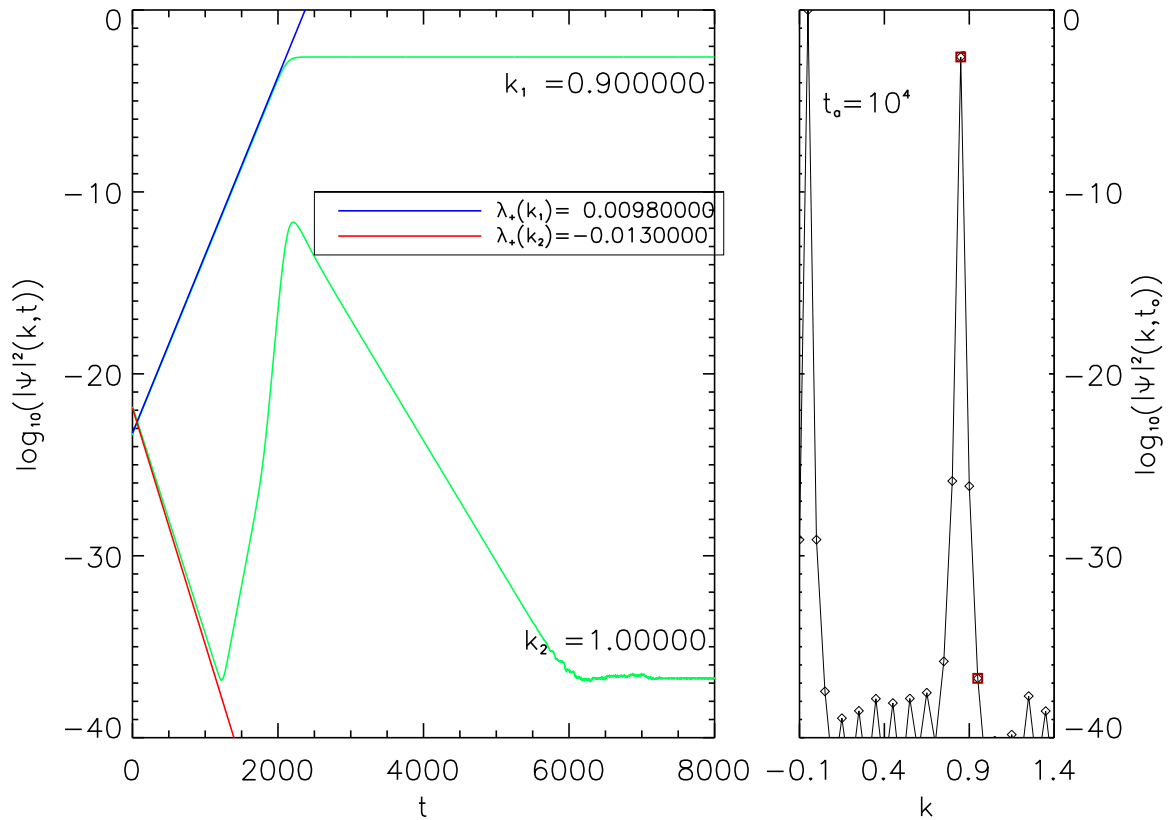


Figure 3.4: Validation of linear approximation in frequency comb dynamics with $\alpha = \sqrt{3} - 0.5$. **(Left)** Plot shows the linear approximation dynamics of two modes with a positive (blue straight line) and negative (red straight line) eigenvalues (indicated at inset legend) in logarithmic scale. In green the whole evolution is included. **(Right)** Plot corresponds to the k interval from where wavenumbers were chosen.

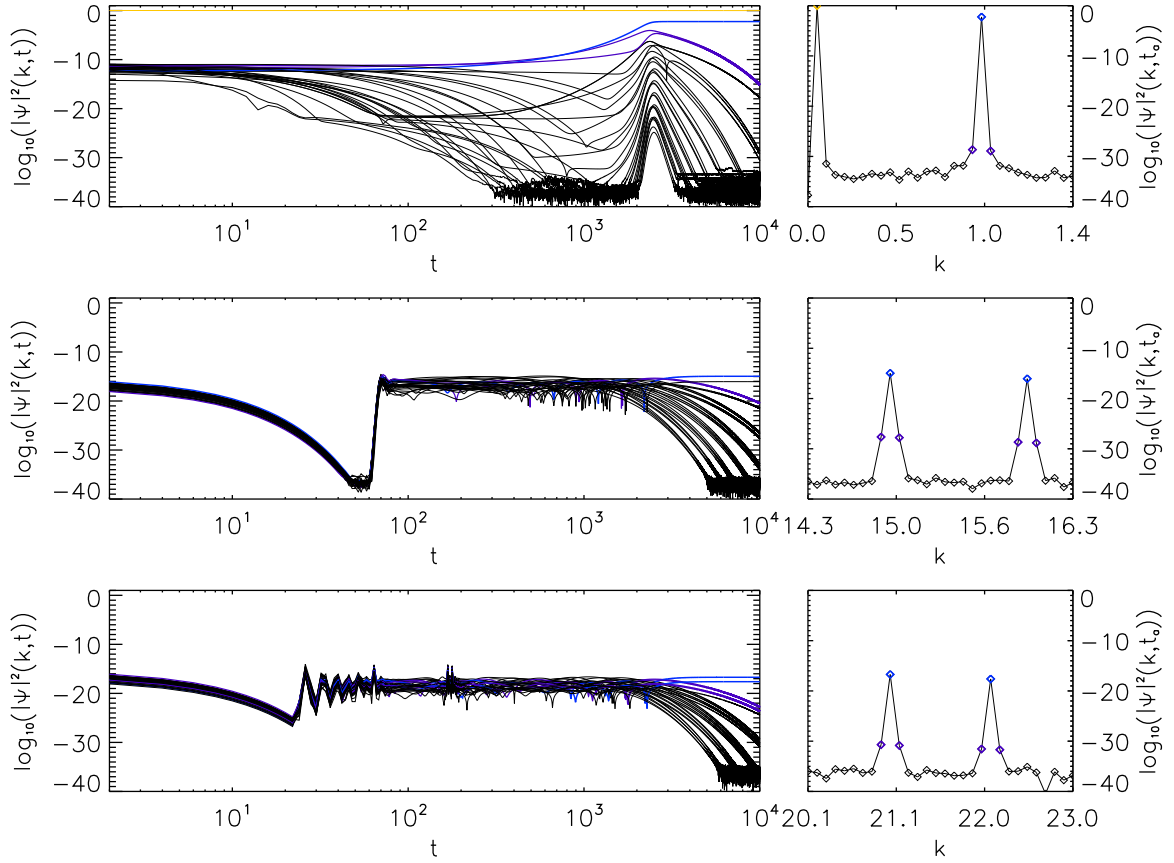


Figure 3.5: Panel distribution displaying mode dynamics for several detunings; (**Top**) $\alpha = \sqrt{3} - 0.5$, (**Middle**) $\alpha = 1.8$, (**Bottom**) $\sqrt{3} + 0.5$. (**Left**) Curves corresponding to the individual time behaviour. (**Right**) Modes labeled by k participating in the plot. Comb peaks are represented in blue, in purple their sideband frequencies and in yellow the homogeneous mode (only in **(top)** row). Time axis is expressed in log-scale.

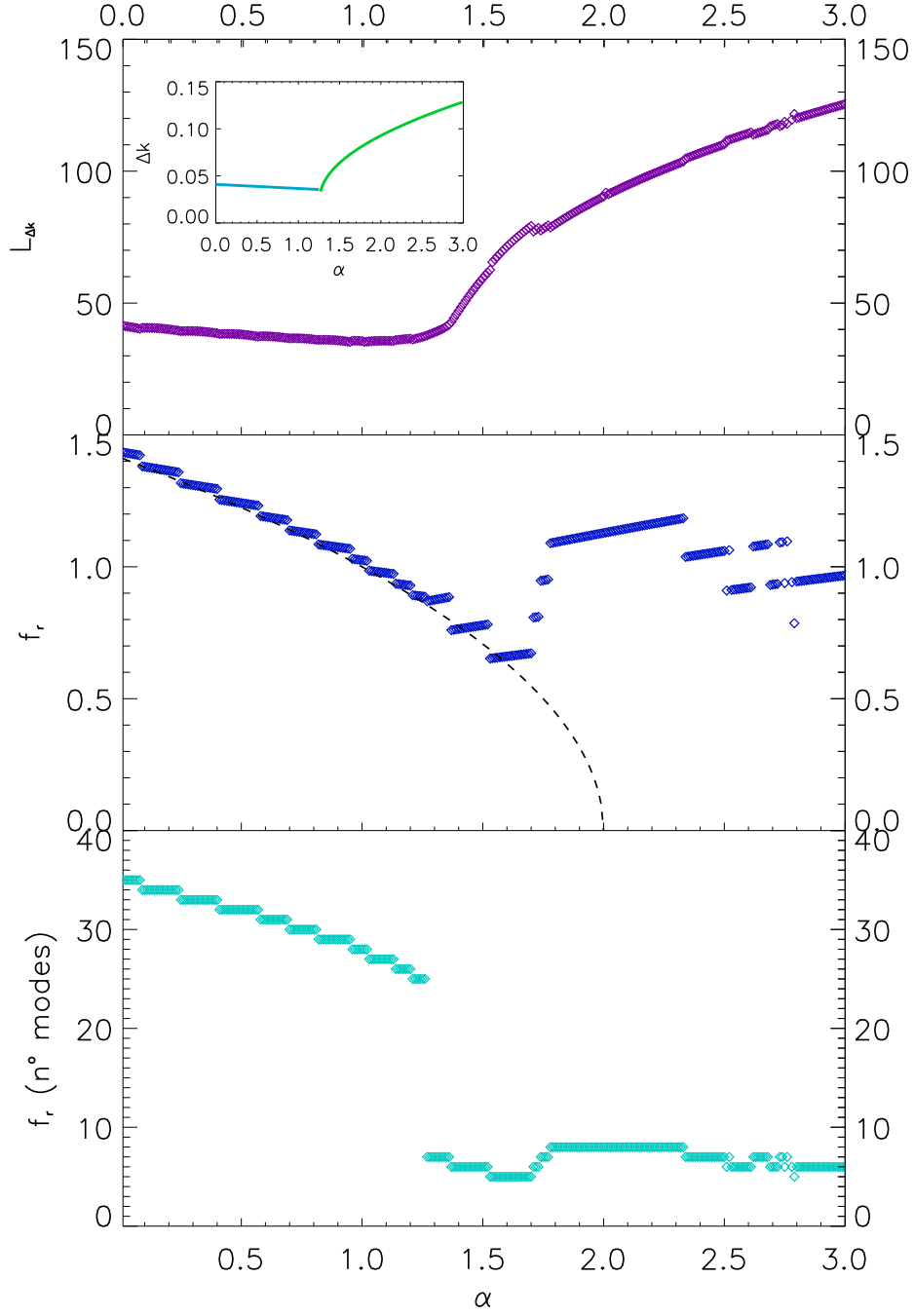


Figure 3.6: Characterization of frequency combs over the detuning domain under study. (**Top Inset**) System size scheme or minimum wavenumber spacing used in the computation of the deterministic frequency combs. (**Top**) Size of the Fourier domain $L_{\Delta k}$ populated by meaningful system modes as a function of α . (**Middle**) Numerical value of f_r , the comb tooth spacing, in Fourier space as a function of α . In dashed line the critical value $k_c = \sqrt{\alpha - 2}$. (**Bottom**) Same as before but expressing f_r as the integer number of modes separating comb peaks resulting from the numerical model.

3.2 Stochastic Combs

Figure 3.6 constitutes the portray of deterministic frequency combs in the detuning regime this thesis discusses; $\alpha \in [0, 3]$. The effect of stochastic terms, introduced in section [2.3], into the deterministic solutions, altogether with the previous information, is analyzed in this section. Therefore the new problem now consists in solving the dynamical system LLE + stochastic term, under the initial condition given as a fully grown stationary deterministic frequency comb. The procedure is evolving the new pattern until it achieves the stationary state. Considering a stochastic LLE equation, the mathematical treatment from section (2.2) is not valid anymore and we are dealing with a different scenario for each different noise scheme. That is the reason new solutions will not start from an homogeneous plus small fluctuations background. If in addition the noise amplitude is of low intensity, this let us to study the effects of noise as first order perturbations in the stationary frequency comb ψ_o , also being valid in fourier space.

$$\begin{aligned}\psi &= \psi_o + \delta\psi \\ \hat{\psi} &= \hat{\psi}_o + \delta\hat{\psi}\end{aligned}\tag{3.3}$$

Still, ψ is a random field. Patterns were provided as the square modulus of the field. This thesis proposes the study of the structures generated through noise excitation taking the average of succesive patterns realizations, both in real and fourier space.

$$\begin{aligned}\langle \psi\psi^* \rangle &= \langle (\psi_o + \delta\psi)(\psi_o^* + \delta\psi^*) \rangle = \langle \psi_o\psi_o^* \rangle + \langle \psi_o\delta\psi^* \rangle + \langle \psi_o^*\delta\psi \rangle + \langle \delta\psi\delta\psi^* \rangle \\ \langle \hat{\psi}\hat{\psi}^* \rangle &= \langle (\hat{\psi}_o + \delta\hat{\psi})(\hat{\psi}_o^* + \delta\hat{\psi}^*) \rangle = \langle \hat{\psi}_o\hat{\psi}_o^* \rangle + \langle \hat{\psi}_o\delta\hat{\psi}^* \rangle + \langle \hat{\psi}_o^*\delta\hat{\psi} \rangle + \langle \delta\hat{\psi}\delta\hat{\psi}^* \rangle\end{aligned}\tag{3.4}$$

The implementation of noise, through white noise, has not any preference around the stationary state. Thus fluctuations fulfill $\langle \delta\psi \rangle = \langle \delta\psi^* \rangle = 0$. Therefore in Eq. (3.4) cross terms vanish, and the average turns out to be

$$\begin{aligned}\langle \psi\psi^* \rangle &= |\psi_o|^2 + \langle |\delta\psi|^2 \rangle \\ \langle \hat{\psi}\hat{\psi}^* \rangle &= |\hat{\psi}_o|^2 + \langle |\delta\hat{\psi}|^2 \rangle\end{aligned}\tag{3.5}$$

Simulations let explore the square modulus of perturbations around the stationary pattern. To begin with, Figures 3.7, 3.8, 3.10, 3.9, 3.11 represent the main outcomes of the simulations. These are averages of 100 realizations using fluctuations, starting from the initial stationary comb with parameters remarked in the figure captions and driving the system towards its stationary state. As for deterministic frequency combs, addressing the question when the stationary state is achieved is not trivial. In the case of fluctuations the system is very sensible to the perturbation amplitude used, hence there is no absolute criteria to accurate determine such final situation. Different modes may achieve stationary state at different times. A generic time of $t = 3000$ is considered to reach the stationary state, inferred by means of analyzing the individual behaviour of modes under different schemes. In case of static noise modes really remain stationary in time while for time dependent fluctuations what remains stationary is the amplitude of modes oscillations. New spectrums include two basic properties. Broadly speaking these consist on a continous spectrum due to the excitation of every mode, overlapping the initial stationary comb and a broadening of the remaining isolated comb peaks through the excitation of their nearby modes.

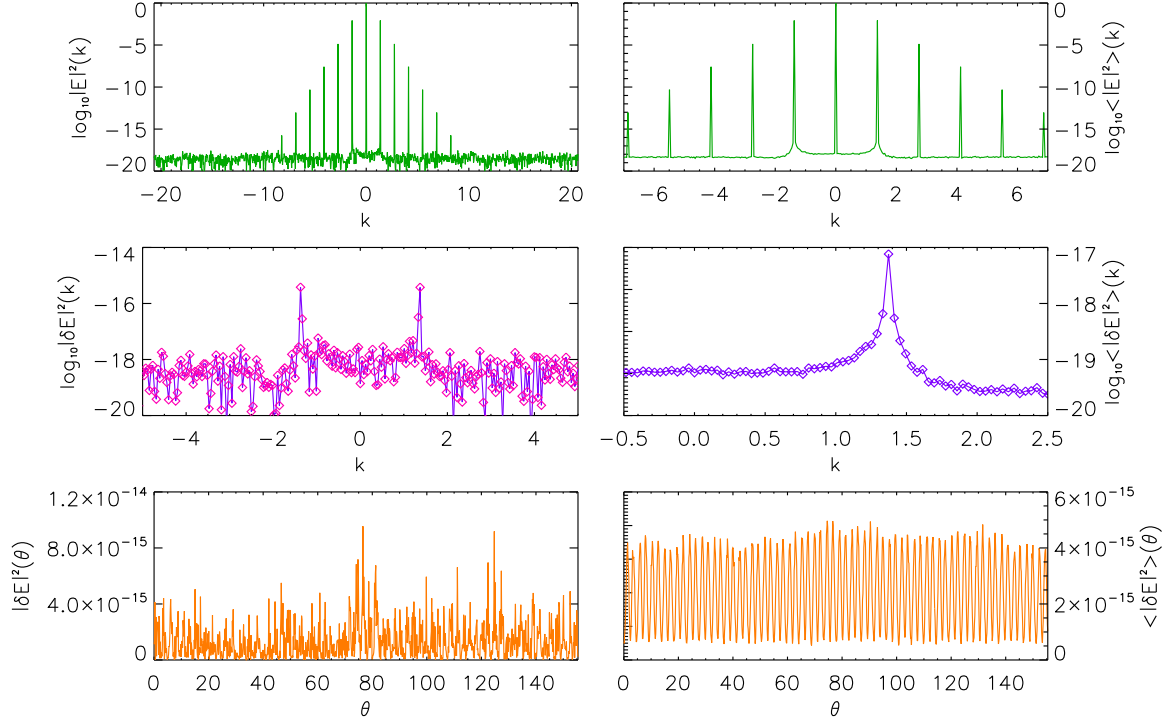


Figure 3.7: LLE with additive spatio temporal noise, Eq. (2.46). **(Left Column)** corresponds to single realizations. **(Right Column)** to averages with 100 realizations. **(Top)** the stationary resulting power spectrum $\hat{\psi}\hat{\psi}^*$, $\langle\hat{\psi}\hat{\psi}^*\rangle$, **(Center)** perturbed patterns $\delta\hat{\psi}\delta\hat{\psi}^*$, $\langle\delta\hat{\psi}\delta\hat{\psi}^*\rangle$, **(Bottom)** the same as before but presenting the real space fluctuations $\delta\psi\delta\psi^*$, $\langle\delta\psi\delta\psi^*\rangle$. For this simulation the noise amplitude is $\mu_0 = 10^{-8}$, $\alpha = 0.1428$.

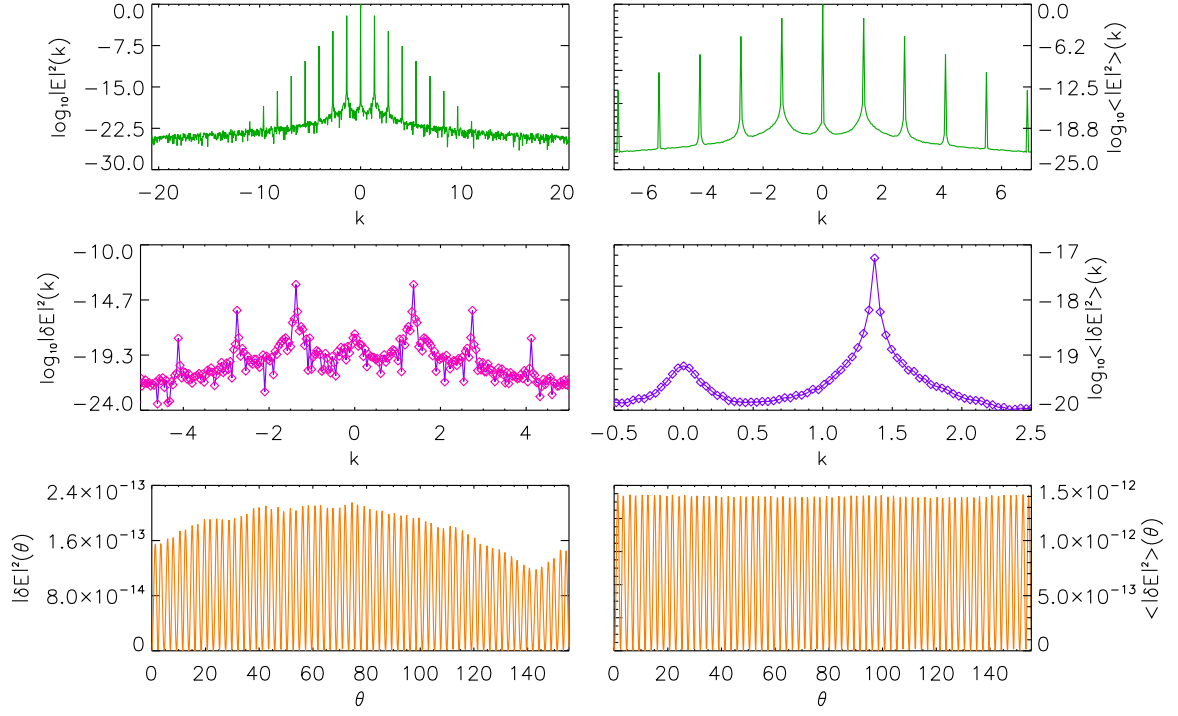


Figure 3.8: LLE with static multiplicative noise in the detuning, Eq. (2.47). **(Left Column)** corresponds to single realizations. **(Right Column)** corresponds to averages with 100 realizations. **(Top)** the stationary resulting power spectrum $\delta\hat{\psi}\delta\hat{\psi}^*$, $\langle \delta\hat{\psi}\delta\hat{\psi}^* \rangle$, **(Center)** perturbed patterns $\delta\hat{\psi}\delta\hat{\psi}^*$, $\langle \delta\hat{\psi}\delta\hat{\psi}^* \rangle$, **(Bottom)** the same as before but presenting the real space fluctuations $\delta\psi\delta\psi^*$, $\langle \delta\psi\delta\psi^* \rangle$. For this simulation the noise amplitude is $\mu_0 = 10^{-8}$, $\alpha = 0.1428$.

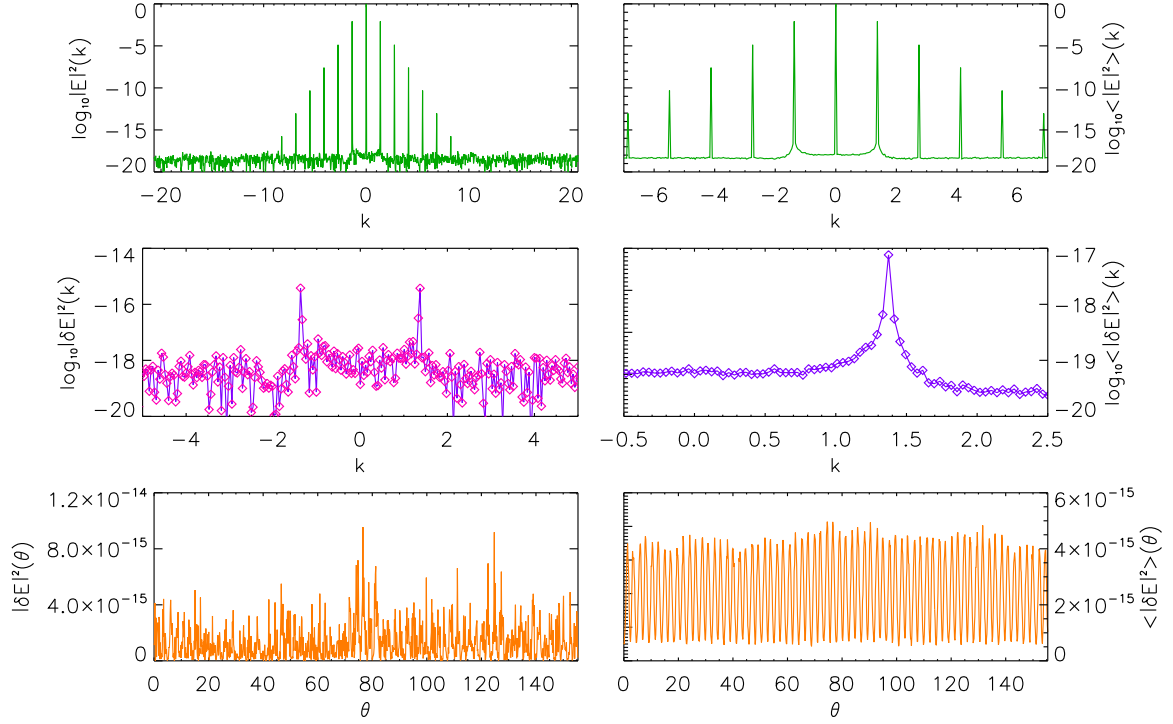


Figure 3.9: LLE with spatio temporal multiplicative noise in the detuning, Eq. (2.48). (**Left Column**) corresponds to single realizations. (**Right Column**) corresponds to averages with 100 realizations. (**Top**) the stationary resulting power spectrum $\delta\hat{\psi}\delta\hat{\psi}^*$, $\langle\delta\hat{\psi}\delta\hat{\psi}^*\rangle$, (**Center**) perturbed patterns $\delta\hat{\psi}\delta\hat{\psi}^*$, $\langle\delta\hat{\psi}\delta\hat{\psi}^*\rangle$, (**Bottom**) the same as before but presenting the real space fluctuations $\delta\psi\delta\psi^*$, $\langle\delta\psi\delta\psi^*\rangle$. For this simulation the noise amplitude is $\eta_0 = 10^{-6}$, $\alpha = 0.1428$.

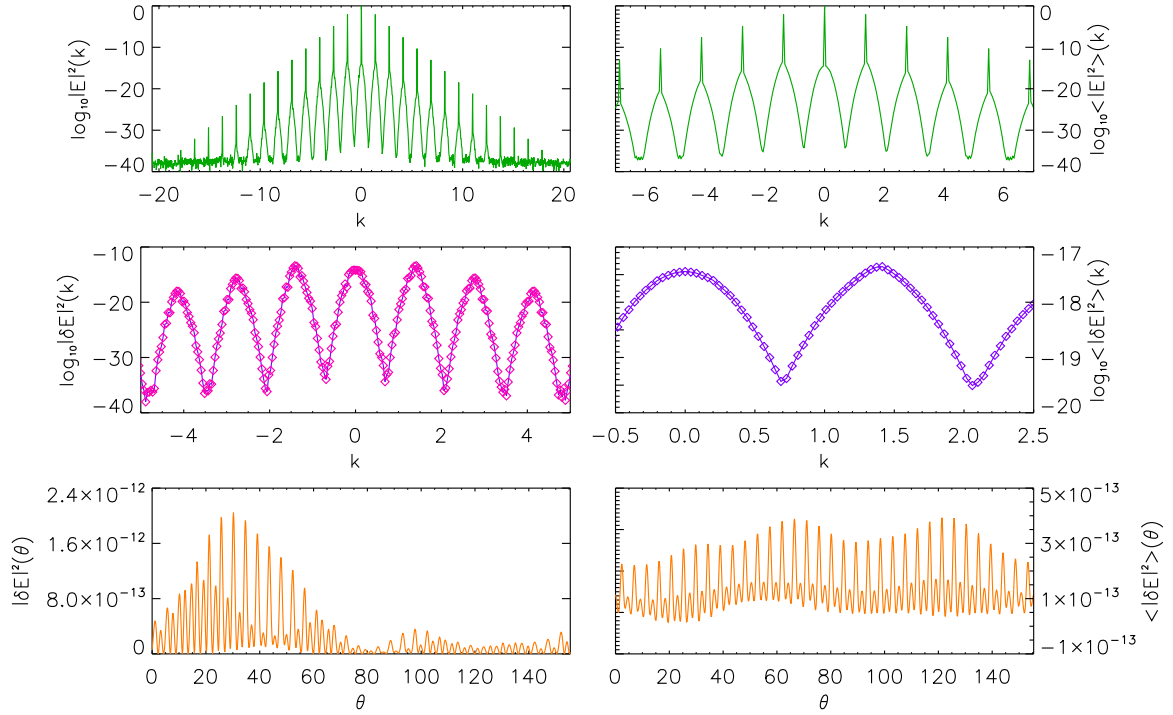


Figure 3.10: LLE with static long wavenumber fluctuations, Eq. (2.49). **(Left Column)** corresponds to single realizations. **(Right Column)** corresponds to averages with 100 realizations. **(Top)** the stationary resulting power spectrum $\hat{\psi}\hat{\psi}^*$, $\langle\hat{\psi}\hat{\psi}^*\rangle$, **(Center)** perturbed patterns $\delta\hat{\psi}\delta\hat{\psi}^*$, $\langle\delta\hat{\psi}\delta\hat{\psi}^*\rangle$, **(Bottom)** the same as before but presenting the real space fluctuations $\delta\psi\delta\psi^*$, $\langle\delta\psi\delta\psi^*\rangle$. For this simulation the noise amplitude is $\mu_0 = 10^{-10}$, $\alpha = 0.1428$ and parameter $\sigma = 0.001$.

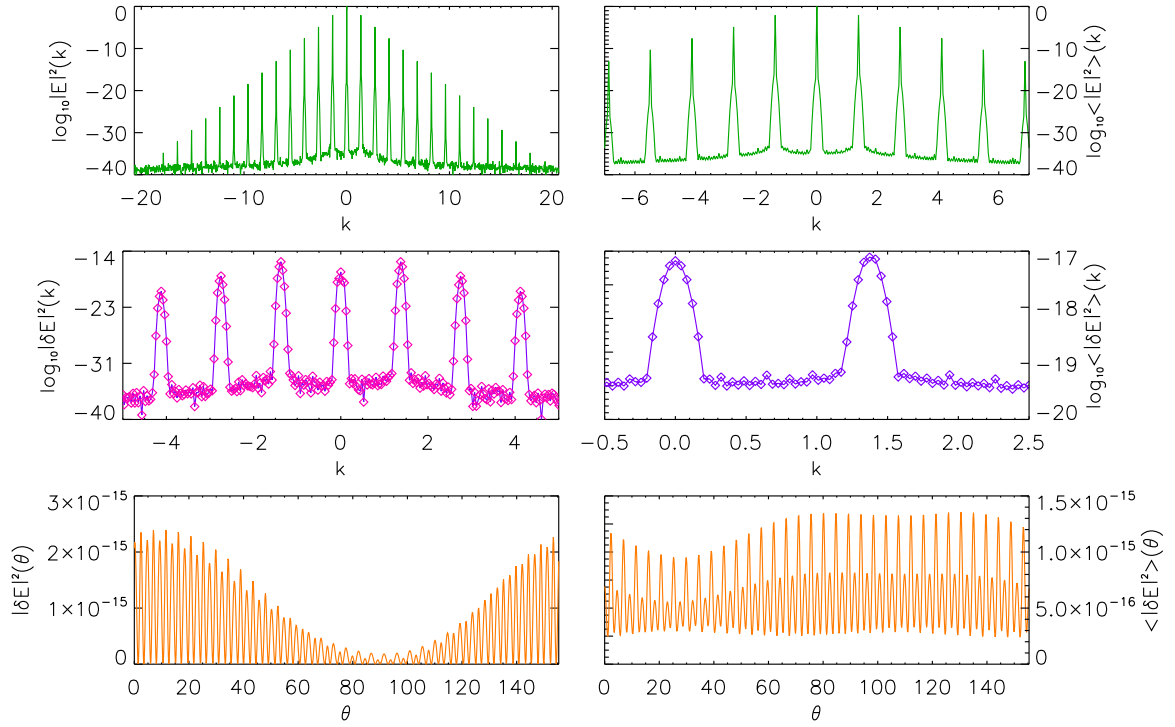


Figure 3.11: LLE with temporal long wavenumber fluctuations, Eq. (2.50). **(Left Column)** corresponds to single realizations. **(Right Column)** corresponds to averages with 100 realizations. **(Top)** the stationary resulting power spectrum $\delta\hat{\psi}\delta\hat{\psi}^*$, $\langle\delta\hat{\psi}\delta\hat{\psi}^*\rangle$, **(Center)** perturbed patterns $\delta\hat{\psi}\delta\hat{\psi}^*$, $\langle\delta\hat{\psi}\delta\hat{\psi}^*\rangle$, **(Bottom)** the same as before but presenting the real space fluctuations $\delta\psi\delta\psi^*$, $\langle\delta\psi\delta\psi^*\rangle$. For this simulation the noise amplitude is $\eta_0 = 10^{-11}$, $\alpha = 0.1428$ and parameter $\sigma = 0.0001$.

There are two exceptions, referring to the cases represented in 3.10 and 3.11. In the case of long wavenumber fluctuations, both static and temporal, there is not appearance of a continuum spectrum, but only the broadening around the comb peaks. Such broadening seems to be directly related to the parameter σ . Meanwhile for static multiplicative noise every comb peak comes with the excitation of its nearby modes, this does not happen for the schemes involving temporal noise, both additive and multiplicative spatio-temporal noise. In those two last, removing the comb peaks one observes that the Fourier spectrum is flat excluding the first mode (and its complex conjugate) which presents a net broadening of their first comb peak. The next observation is the identification of noise excited sidebands around the homogeneous mode. This happens for outcomes 3.8,3.10,3.11. It is interesting to note the absence of such kind of sidebands in the spatio-temporal schemes which may lead to physical interpretations for the experimental comb presented in the modeling section, Figure 2.5.

Regarding the patterns in real space, here it is presented the magnitude $\langle \delta\psi\delta\psi^* \rangle$ altogether with a single realization of the noise. Before presenting these results the pattern harmonics were removed. The resulting contribution to the field on average comes from the highest noise-excited modes. Depending on how these sideband modes are excited, one would expect, once taking the square of the modulus, to be a pure squared harmonic function with frequency $2f_r$. This is clearly seen in Fig. 3.8. Cases 3.10 and 3.11 are different in the sense that they have several excited modes competing each other at a similar magnitude so that the total contribution to the perturbation presents beatings that modulate the amplitude over its periodicity. Concerning single realization simulations, those also present the periodicity approximately of $2f_r$ along with beating modulations which can be accounted for the presence of many randomly excited sideband modes due to noise.

The obtention of more accurate averages with an increasing number of realizations is feasible but would require a huge amount of time. Simulations are carried out in a common desktop computer, taking the order of $\approx 3h$ for averages including $n = 50$ realizations. This amount of time depends on the numerical implementation, being the greatest for additive spatio-temporal noise. This limits the accuracy of predictions done when making the exploration into the space parameters.

Displayed results 3.7,3.10,3.8,3.9,3.11 come with a wide parameter choice. In particular the noise amplitude is different by several orders of magnitude among noise schemes. For instance, Fourier spectrums gathered from the noise-perturbed LLE do not show the same continuum background with the white noise amplitude. Moreover, these combs, altogether with the broadening of comb peaks, can be destroyed (absence of stationary pattern) if this magnitude is too intense. This is related to the threshold where the addition of noise is considered to be a perturbation small enough to be considered of first order. To characterize this, Figure 3.12 presents the **comb energy** \mathcal{E} , the density power spectrum integral. In particular the difference between the deterministic comb and the contribution into Fourier modes due to the noise.

$$\Delta\mathcal{E} = \mathcal{E} - \mathcal{E}_0 = \int dk \hat{\psi}_k \hat{\psi}_k^* - \int dk |\hat{\psi}_{k,0}|^2 = \int dk |\delta\hat{\psi}_k|^2 \quad (3.6)$$

This quantity is a random variable itself. As already stated patterns in this work are described according to their average $\langle |\delta\hat{\psi}|^2 \rangle$, hence it is natural to perform the same analysis with this magnitude. According to Chebyshev's theorem [29] the average is bounded by its sample average and sample standard deviation.

$$\langle \Delta \mathcal{E} \rangle \approx \mu(\Delta \mathcal{E}) + \frac{\sigma(\Delta \mathcal{E})}{\sqrt{M}} \quad (3.7)$$

M is the number of realizations. Given a random variable \hat{x} , μ , σ are expressed as

$$\mu(\hat{x}) = \frac{1}{M} \sum_i \hat{x}_i \quad (3.8)$$

$$\sigma^2(\hat{x}) = \frac{M}{M-1} \left(\frac{1}{M} \sum_i \hat{x}_i^2 - \mu^2(\hat{x}) \right) \quad (3.9)$$

Focusing into the pattern's energy second moment

$$\frac{1}{M} \sum_i \hat{x}_i^2 = \frac{1}{M} \sum_i \Delta \mathcal{E}_i^2 = \iint dk dk' \frac{1}{M} \sum_i |\delta \hat{\psi}_{k,i}|^2 |\delta \hat{\psi}_{k',i}|^2 = \iint dk dk' a_{k,k'} \quad (3.10)$$

Matrix $a_{k,k'}$ is also retrieved from the perturbed LLE realizations.

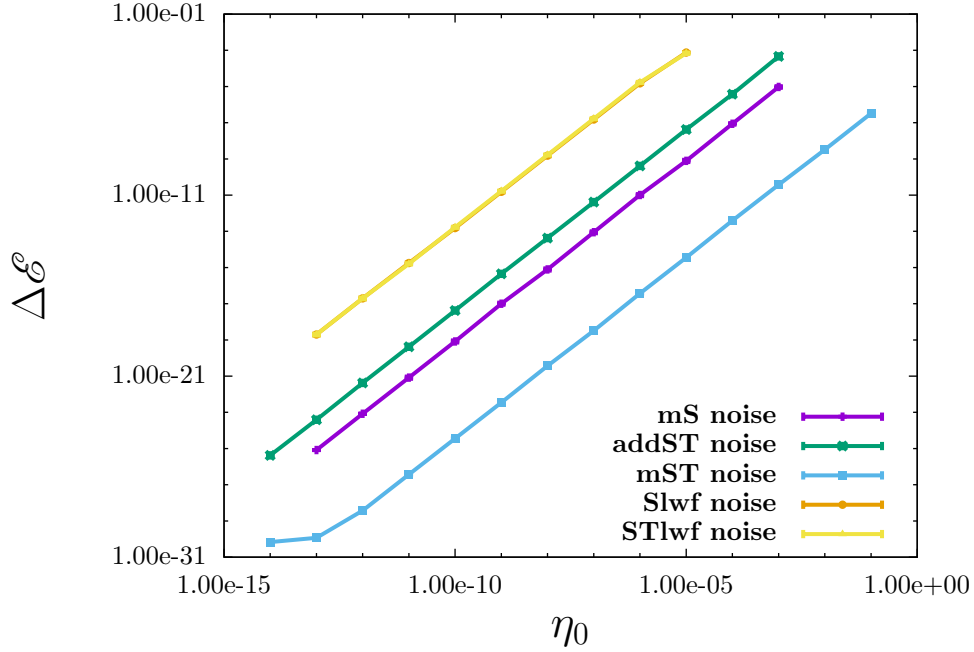


Figure 3.12: Contribution of stochastic perturbations to system's $\Delta \mathcal{E} \delta \psi \delta \psi^*$ as function of the amplitude noise parameter η_0 . Legend reads as **mS** multiplicative Static noise, **addST** additive Spatio-Temporal noise, **mST** multiplicative Spatio-Temporal noise, **Slwf** Static long wavelength fluctuations, **STlwf** Spatio-Temporal longwavelength fluctuations. $\alpha \approx 1.22 < \sqrt{3}$, monostable regime. $\sigma = 0.0001$.

Figure 3.12 displays how the noisy combs depends upon the noise intensity, η_0 , keeping fixed the detuning at $\alpha \approx 1.22$, within the monostable regime. Over a wide range of η_0 , \mathcal{E} seems to

depend linearly on this parameter. Moreover, with the same slope for all the schemes. Using logarithmic scale on both axis the plot keeps it linear with η_0 , showing greater energies as the noise intensity increases. This result may indicate that noise introduces contributions to the comb such that it is evenly distributed once the stationary state is achieved after several realizations, and independent of the kind of fluctuations involved. This happens despite for instance, multiplicative noise has a preference of perturbing modes contributing more to the field ψ (the spectrum of a deterministic comb shows the first harmonic is the most intense). Another interpretation, is that the total contribution to \mathcal{E} is such that every mode but the first harmonic sidebands are negligible in terms of contributing to the integral. Thus based on this analysis, this magnitude does not clearly indicate differences among how noise schemes excite the comb spectrum. Nevertheless this result clearly states the relation of systems more efficiently translating random excitations into their stationary power density spectrum. From greater to lesser degree the relation is, Spatio-Temporal and Static long wavelength fluctuations (approximately equal) **Slwf** and **STlwf**, additive Spatio-Temporal noise **addST**, multiplicative Static noise **mS** and finally multiplicative Spatio-Temporal noise **mST**. From this result next information comes about the stability of patterns depending on η_0 . Not explicitly stated in the graph, it has been observed that **Slwf** and **STlwf** become unstable for, approximately, $\eta_0 > 10^{-6}$. On the other hand the others schemes are fearly stable over a great range for the parameter involved, whose stationary patterns are destroyed when the amplitude of the random numbers are clearly beyond just a first order contribution to the field. The final observation is when noise is negligible enough to produce any excited noise modes. Such limit is displayed for **mST** in figure (3.12) for $\eta_0 \approx 10^{-15}$, with \mathcal{E} not decreasing anymore. Depending \mathcal{E} linearly on η_0 , the previous limit helps to extrapolate to which noise amplitude the system is not exciting any extra-mode.

The previous study was carried out just for a particular α . The following step is extending such analysis to how $\Delta\mathcal{E}$ changes with the detuning. A sample is taken from static multiplicative noise results using amplitudes $\eta_0 = 10^{-3}, 10^{-6}, 10^{-9}$, and displayed in Figure 3.13. First, comprising the whole range of detuning explored, stands out that the difference among η_0 values is the same as indicated in Plot 3.12 for every α . To emphasize this result, what is really plotted is the real output from $\eta_0 = 10^{-9}$ over which the others two data sets, times factors of 10^{-6} and 10^{-3} respectively, overlap it, matching in quite good agreement. Thus the pattern noted in Fig. 3.12 can be extrapolated for every detuning value. There is a sudden and noticeable $\Delta\mathcal{E}$ with several order of magnitudes above what seems to be the natural dependence on α . of this quantity. A possible explanation could be of numerical nature, due to a bad precision on α that leads the underlying deterministic comb to have a higher density of comb peaks. This interpretation is motivated by the bottom plot of Figure 3.6 where a sudden transition towards higher density of comb peaks takes place at approximately such α . Along with each data point is also included its standard deviation as y-errorbar. The values obtained for the last magnitude are small enough to not be significantly differentiated from the data point markers, at least using logscale axis. Nevertheless, the magnitude under study does not seem to meet at a very precise curve, even though $\frac{\sigma(\Delta\mathcal{E})}{\sqrt{N_{aver}}}$ is small. Apart from α , the parameter which this work tries stochastic combs to solely depend on, the system is actually very sensible on other parameters such that Δk or $L_{\Delta k}$. Thus it is feasible not having a very smooth behaviour, although those are fixed for each α .

Next, the previous idea is tested but envisaging all noise schemes. Figures 3.14,3.15 illustrate it for $\eta_0 = 10^{-9}$. With such value, patterns remain stable under any random fluctuations tested. Figure 3.14 includes the standard deviation as y-errorbars, but as before it is not distinguishable. Instead, this magnitude is displayed in 3.14 independently. Assuming the dependence of $\Delta\mathcal{E}$ on η_0 is independent of α , comparing among the different schemes for each α is also independent of the

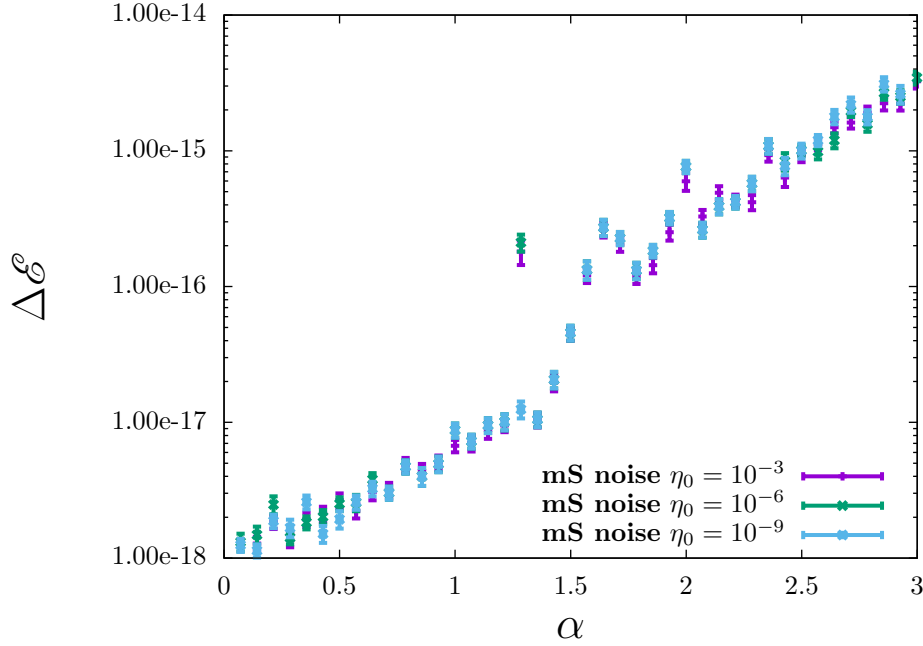


Figure 3.13: Results for $\Delta\mathcal{E}$ obtained with multiplicative static noise as function of α . Results corresponding to $\eta_0 = 10^{-3}, 10^{-6}$ are presented multiplied by constant factors $10^{-6}, 10^{-9}$ respectively to stress that the noise amplitude constitutes a fixed amount into the comb energy being independent of the detuning.

noise amplitude. These results states that the relative. The conclusions drawn from Figure 3.12 persist. Again **Slwf**, **STlwf** are the most intense followed by **addST**, **mS** and finally **mST**. This holds true for the whole parameter set. As the detuning increases, $\Delta\mathcal{E}$ also increases. The main contribution to that may arise from a larger system size altogether with a higher comb peak density, resulting in more noisy modes. The most interesting observation comes by the aparent transition from monostable regime to bistable regime with pattern forming instability and between bistable regime with pattern forming instability to pattern forming instability with homogeneous instability. The system notes this by a higher energy contribution at the boundaries of this transitions in α domain, $\alpha = \{\sqrt{3}, 2\}$. For detunings near right boundary, multiplicative static noise and additive spatio temporal noise approach to each other in intensity. On account of the reasons given before, the higher comb peak density implies that numerically the discretization of N points representing the WGM is not accurate, and the system's reaction upon random fluctuations becomes similar, for every scheme used. Studying the fluctuations of this averages, the behaviour is the same, taking place higher fluctuations of the noisy modes (hence on the quantity $\Delta\mathcal{E}$) being greater for larger detunings.

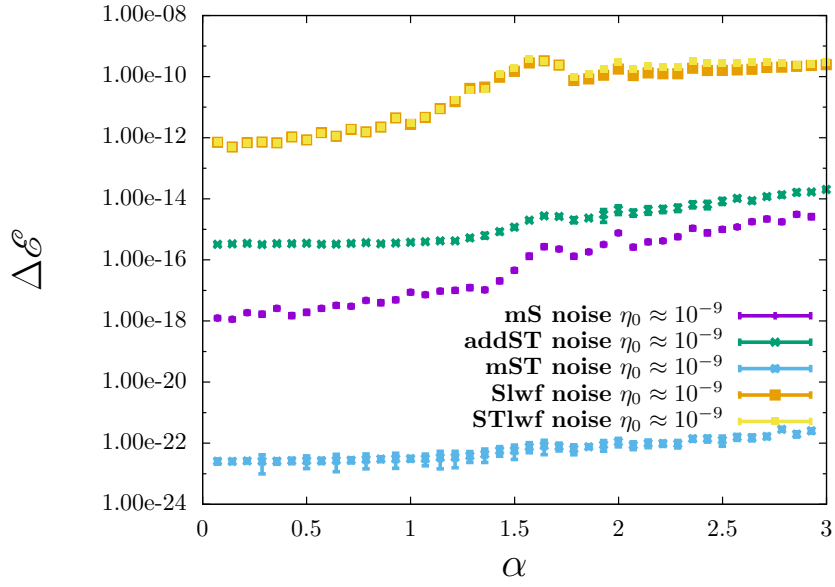


Figure 3.14: Results for $\Delta \mathcal{E}$ for all kind of fluctuations versus α . $\eta_0 = 10^{-9}$. $\sigma = 0.0001$.

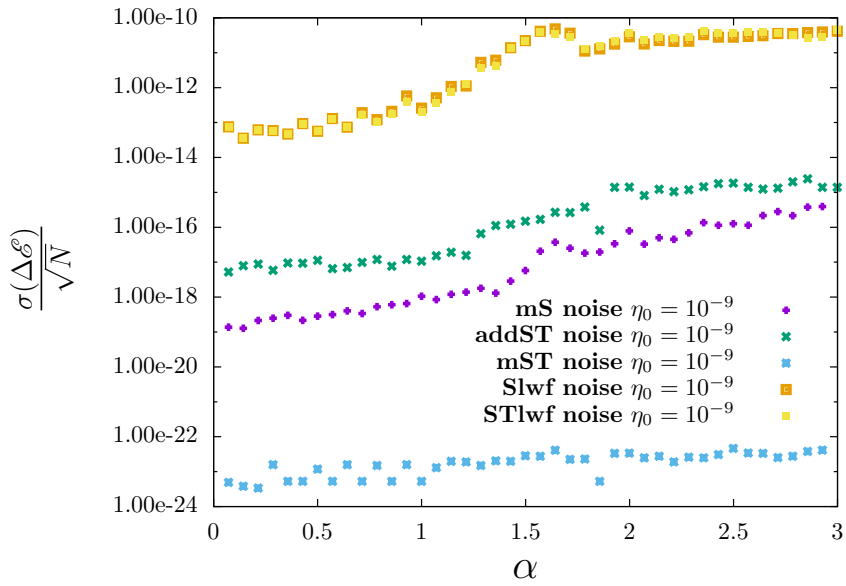


Figure 3.15: Results for $\sigma(\Delta \mathcal{E})$ for all kind of fluctuations versus α . $\eta_0 = 10^{-9}$. $\sigma = 0.0001$.

Once a general overview of the stochastic comb performance is provided, this work moves into the results yielding the properties seen at the experimental Figure 2.5. At outcomes displayed 3.7,3.10,3.8,3.9,3.11, whenever a scheme produces an effective excitation of noisy-modes around $k = 0$, it is shown qualitatively how these decline as the distance to $\langle |\hat{\psi}_{k=0}|^2 \rangle$ increases. This happens until their intensity intersects the corresponding noisy background. The next result gives insight on how such decay takes place as α varies. As for $N = 1024$ the density of comb peaks is large for large detunings, excited noisy modes are highly compacted and it is difficult to distinguish how they decrease. To overcome this issue it is proposed to study the behaviour of excited modes around $\langle |\hat{\psi}_{k=0}|^2 \rangle$ by means of the following two fourier modes and their complex conjugates.

$$\Omega_\alpha = \frac{\langle |\hat{\psi}_{k=\Delta k}|^2 \rangle + \langle |\hat{\psi}_{k=-\Delta k}|^2 \rangle - \langle |\hat{\psi}_{k=f_r/2}|^2 \rangle - \langle |\hat{\psi}_{k=-f_r/2}|^2 \rangle}{\langle |\hat{\psi}_{k=f_r/2}|^2 \rangle + \langle |\hat{\psi}_{k=-f_r/2}|^2 \rangle} \quad (3.11)$$

The difference between the first noise-excited mode, thus the most intense, and the noisy background, assumed to be at the center between nearest comb peaks¹, over the latter. Therefore the notation of $\pm\Delta k$, $\pm f_r/2$ in the subscripts. To make use of the fourier spectrum symmetry, modes are presented as the average among complex conjugates around $k = 0$. This quantity is a measure of how modes are excited relative to the background spectrum, as long as computational issues let the task to be studied. Outputs are presented in Figures 3.16,3.17. Systems not producing random fluctuations around the homogeneous mode corresponding to plots 3.7,3.9 are omitted from the figures, being bounded by $\Omega_\alpha \leq 1$.

According to previous results, modifying η_0 the net effect in $\Delta^{\mathcal{E}}$ is the same linear dependence for all systems but it gave not insight into the precise fourier spectrum shape. Results presented here show static multiplicative noise at Fig. 3.17 exhibit no difference for different η_0 while in turn for long wavelength fluctuations there is a clear difference, particularly for small detunings. Hence it is possibly to hypothesize that power spectral density spectrums for multiplicative noise are independent of the noise amplitude but a homogeneous factor. In logarithmic scale this is seen as a rigid displacement of the spectrum, being the shape of excitations independent of this parameter. On the other hand, the noise intensity seems to scale down this modes, having a net effect on how fluctuations excites the spectrum.

Comparing the potential of producing homogeneous random excited sidebands, the greater Ω_α , the greater this modes are excited. Longwavelength fluctuations in any case for the whole range of α overtakes those in static multiplicative noise, hence being a better candidate for the experimental observations. When including the dependence on the detuning, it is interesting to stress the appearance, as has been stated in other cases, of a transition at $\alpha = \sqrt{3}$, where while the detuning increases the excitation of these modes suddenly rise up again. After this transition, the dependence on η_0 seems to reduce for long wavelength fluctuations.

¹This is not exactly true, since what happens is the continuum background overlaps, but it is the deepest the numerical simulation data can compare with

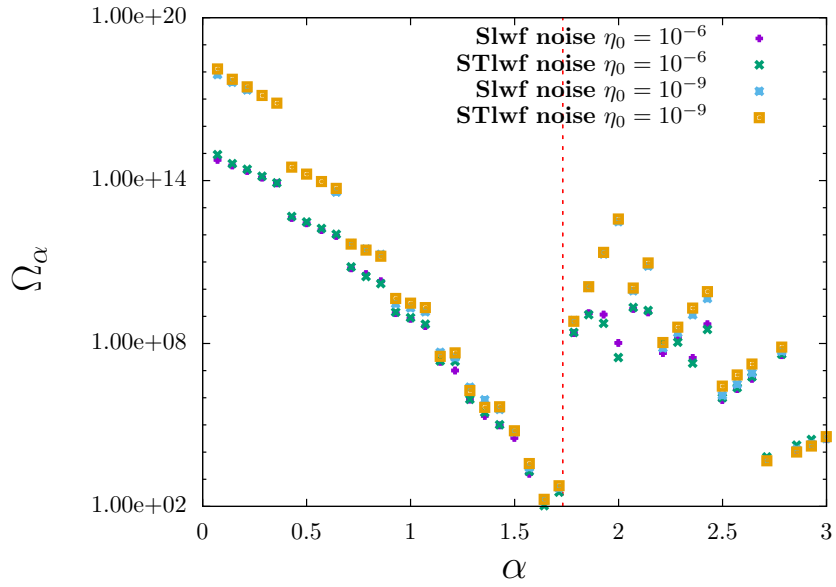


Figure 3.16: Quantity Ω_α for Static and Spatio Temporal long wavelength fluctuations versus α . Vertical red line indicates transition to bistable regime. $\sigma = 0.0001$.

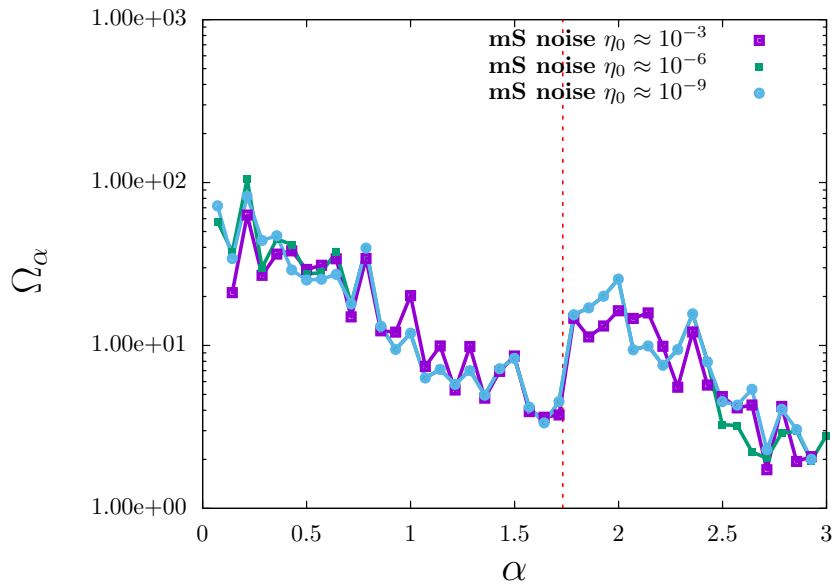


Figure 3.17: Quantity Ω_α for Static multiplicative noise versus α . Vertical red line indicates transition to bistable regime.

The last of the results deals with the parameter σ introduced when modeling longwavelength fluctuations. This time the quantity to be tested is the homogeneous modes, quantized as the energy they represent above the continuum background,

$$\mathcal{E}_{k=0} = \int_{-\frac{f_r}{2}}^{\frac{f_r}{2}} dk \langle |\delta\hat{\psi}_k|^2 \rangle - f_r \left(\langle |\delta\hat{\psi}_{k=-f_r/2}|^2 \rangle + \langle |\delta\hat{\psi}_{k=f_r/2}|^2 \rangle \right) \quad (3.12)$$

A magnitude represented in Figures 3.18,3.19,3.20,3.21 versus α and σ . Keeping fixed $\sigma = 10^{-4}$, Figures 3.18,3.19 show the principal behaviour with α presents a peak at intermediate values of the detuning, from which starts to begin decreasing until $\alpha = \sqrt{3}$, point beyond the bistable regime takes place, yielding a steady increase. From both pictures, Spatio-Temporal noise is slightly more effective in generating homogeneous excited modes. The main observation is that for higher detunings, $\mathcal{E}_{k=0}$ accordingly raises. The dependence with η_0 mainly introduces a constant contribution to the energy regardless of the detuning. Within this scenario, it can be seen according to Figures 3.20,3.21 that this is no longer true when σ comes into play. Bounding more strictly the wavelength interval where fluctuations occur, in particular limiting it to longer wavelengths by decreasing parameter σ , there is a point in which the last statement reverses. Again, η_0 does not play a major role. On the other hand as σ enlarges the increase in $\mathcal{E}_{k=0}$ quickly saturates to the maximum value presented for $\sigma = 10^{-4}$. The interval of this parameter encompasses the order of magnitude at which stochastic combs keep stable.

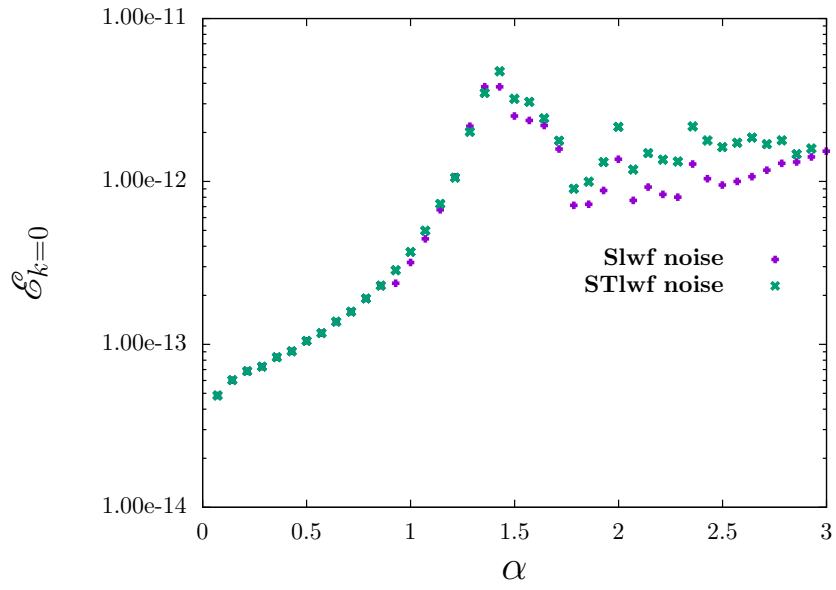


Figure 3.18: $\mathcal{E}_{k=0}$ versus α . $\eta_0 = 10^{-9}$. $\sigma = 0.0001$.

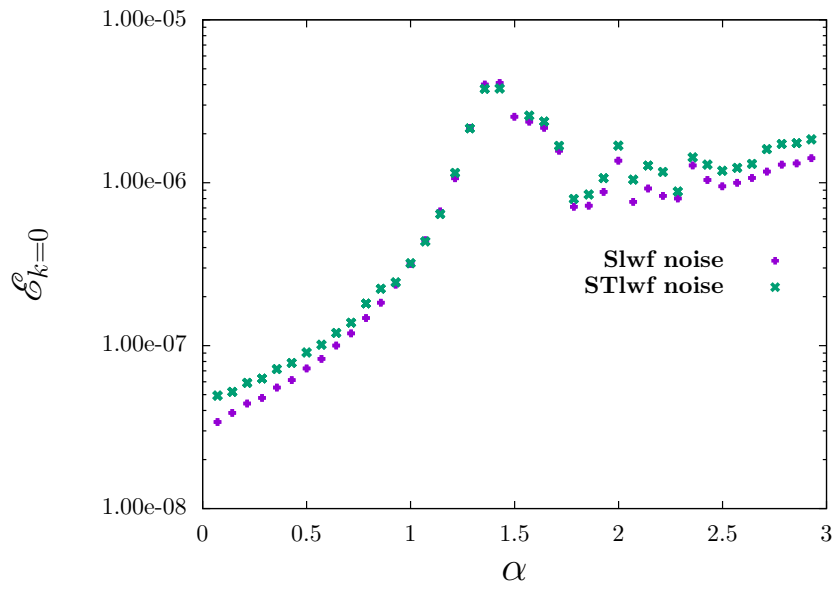


Figure 3.19: $\mathcal{E}_{k=0}$ versus α . $\eta_0 = 10^{-6}$. $\sigma = 0.0001$.

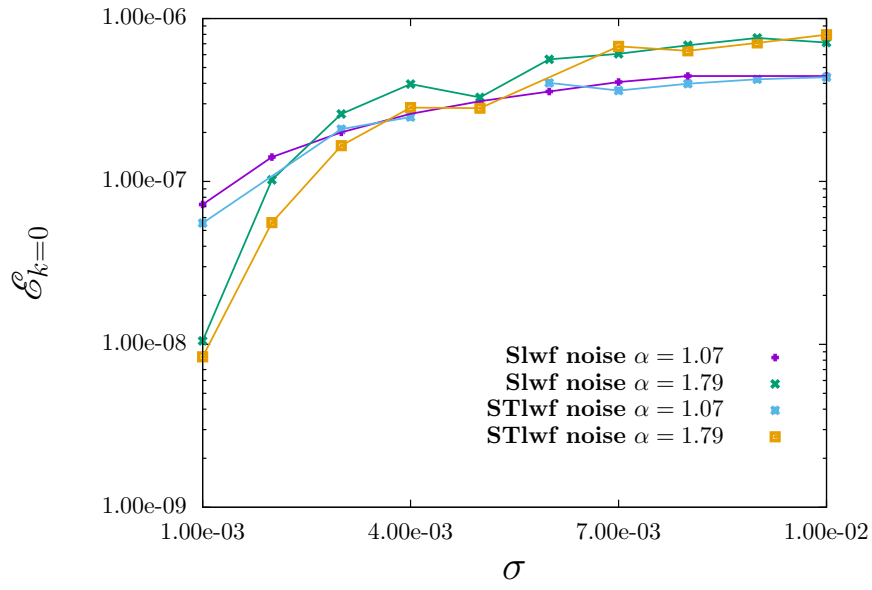


Figure 3.20: $\mathcal{E}_{k=0}$ versus σ . $\eta_0 = 10^{-6}$.

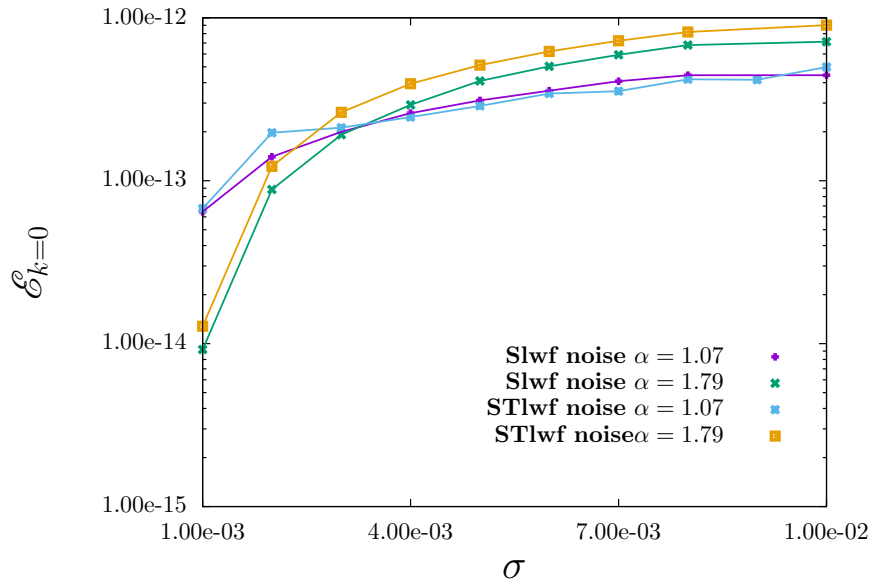


Figure 3.21: $\mathcal{E}_{k=0}$ versus σ . $\eta_0 = 10^{-9}$.

Chapter 4

Conclusions

Throughout the preparation of this thesis the generation of frequency combs has been addressed via the Lugiato-Lefever equation plus the addition of random fluctuations in a series of numerical models. The physical context of whispering gallery modes resonators and the Lugiato-Lefever model is reviewed. Prior probing the effects of random fluctuations in this equation, an extensive study of deterministic frequency combs is carried out. This study restricts the control of frequency combs to a single free parameter, the detuning, the difference in frequency between the input frequency and the nearest resonator mode in the WGR after a proper parametrization. The conditions exposed in chapter 2 to bring the system towards a critical unstability leads to the formation of stationary periodic patterns. Therefore this model and the pseudo spectral algorithm is validated to study frequency combs. Due to the use of discrete fourier transform and numerical issues, the problems of aliasing and system size are identified and solved by properly tuning Δk as function of α . Analyzing f_r , its value coincides with the critical wavelength λ_c up to $\alpha = \sqrt{3}$, transition to the bistable regime, and thus its dependence abruptly changes. The system size $L_{\Delta k}$, even though related to the concept of meaningful modes and the numerical precision used, gives an idea about how successive harmonics are excited relative to the pumping. A greater system size is indicative that the pumping more efficiently transfers more energy. This happens with increasing α . The comb peaks density being $\frac{1}{f_r}$ turns out to increase up to $\alpha = \sqrt{3}$, where the behaviour changes and starts to slightly increase with the remaining detuning interval.

Introducing stochastic combs and their properties, the amplitude of white noise in the algorithms does not play a major role in the development of spectral features. Small fluctuations yield the same output but for a homogeneous contribution to the whole comb. Furthermore, all schemes behave quite similar except for long wavelength fluctuations. An interesting feature, already noted for the same detuning in deterministic combs, is the appearance of a transition on how noisy modes abruptly changes at the onset of the bistable regime. This directly affects the noise spectrum and is clearly seen in Figures presenting Ω_α , 3.16,3.17. The width of long wavelength modes that fluctuates in the pumping frequency, indicated by the parameter σ in the modeling, has also been tested through the analysis of $\mathcal{E}_{k=0}$. The main observation is that the dependence with α of the homogeneous modes inverts if σ is moderate enough. Since this study was carried analyzing $\mathcal{E}_{k=0}$ the previous statement can present repercussions if the pumping frequency used is more or less precise.

The main goal of this thesis is to characterize the stochastic combs and to identify which schemes yield a similar output to Fig. 2.5, corresponding to laboratory measurements. In this respect the

work also succeeds showing that static multiplicative noise and both static and spatio-temporal long wavelength perturbations produce homogeneous random excited sidebands. On the other hand both spatio-temporal additive and multiplicative noise do not reproduce this result. A first claim is that additive noise, modeling random fluctuations in the electric field inside the resonator, does not play a role in this mechanism, while on the other side the temporal dependence in multiplicative noise, motivated by thermal fluctuations either seems to prevent the formation of those spectral features. Static multiplicative noise comes by introducing imperfections in the resonator, giving rise to local differences in the cavity modes, thus perturbing the detuning along the whole domain. Hence if the model has $k = 0$ assigned to the pumping frequency, these local differences in the detuning can be interpreted as if the pumping frequency was different, rather than the nearest cavity mode itself finally yielding the excitation of modes with $k \approx 0$. Nevertheless it should imply that the higher the fluctuations in α , then the wider the range of homogeneous sidebands should be excited. This feature is not observed during the modeling presented in this work (see Fig. 3.17).

Experimentally it may be difficult to isolate thermal fluctuations. Therefore static multiplicative noise could not properly predict the unexpected result in a real device. The possibilities are left with long wavelength fluctuations in the pumping as the most suitable candidate. These perturb modes with $k \approx 0$ and the physical motivation this term relies on states the fact the pumping laser is not ideally monochromatic. Considering their static or temporal behaviour, the performance is rather similar independent on their spatio-temporal nature. In addition this fluctuations present the most intense contribution to $\langle |\psi_k|^2 \rangle$ relative to the fluctuating noisy background. The quantitative analysis developed shows the excitation of noisy modes is more effective than for static multiplicative noise comparing Ω_α for each scheme.

The problem of aliasing arised during the study of deterministic frequency combs. The presence of finite size effects also comprises the study of stochastic frequency combs due to a relatively small discretization of fourier modes. Taking $N = 1024$ can present problems when the detuning is high and so the comb peaks density also raises. Due to that the resolution does not allow for noise modes to evolve. A smoother discretization would dramatically enlarge the computation time for studying these fluctuations, being out of the scope of this thesis. Thus for large α there is an uncertainty if results derived are real properties of these stochastic combs or rather those arise due to finite size effects. Looking into the future, a natural direction for this work could be guided towards studying another average magnitudes. Correlations among homogeneous noisy modes with comb peaks or the harmonics noisy sidebands could give insight into how mutually they are influenced. Then extending to our discussion on α it would characterize these spectral features on the parameter space. A deeper mathematical treatment of patterns and fourier modes is convenient to properly understand the model and its fluctuations as well.

Chapter 5

Appendix

5.1 Appendix A: Pseudo Spectral Method

This appendix will explain this method to solve numerically first order partial differential equations, involving time and 1D space. In a nutshell, it converts the partial differential equation problem into a set of ordinary differential equations. To this extent one takes the fourier transform of the PDE; doing so each ordinary differential equation corresponds to the evolution in wavenumber space of a single mode. Both deterministic and stochastic cases are described.

5.1.1 Deterministic Differential Partial Equations

A PDE of the previously required form can be expressed as

$$\partial_t A(x, t) = \mathcal{L}[A(x, t)] + \mathcal{N}[A(t, x)] \quad (5.1)$$

\mathcal{L} denotes the equation linear terms. \mathcal{N} on the other hand represents the nonlinear contribution. The field $A(t, x)$ is assumed to fulfill periodic boundary conditions in a domain $x \in [0, L]$. Furthermore the fourier/inverse fourier transform does exist and reads

$$\begin{aligned} \tilde{A}(t, q) &\equiv \mathcal{F}[A(t, x)] = \frac{1}{L} \int_0^L A(t, x) e^{iqx} dx \\ A(t, x) &\equiv \mathcal{F}[\tilde{A}(t, q)] = \sum_{k=-\infty}^{\infty} \tilde{A}(t, q) e^{-i\frac{2\pi}{L}kx} \end{aligned} \quad (5.2)$$

Defining $q_k = (2\pi/L)k$, the discretized wavenumbers. As it has been mentioned, the idea is taking the fourier transform of the equation.

$$\partial_t \tilde{A}(t, q) = \mathcal{F}[\mathcal{L}[A(x, t)]] + \mathcal{F}[\mathcal{N}[A(t, x)]] \quad (5.3)$$

From linear stability analysis, the fourier transform of a linear combination of linear operators

yields an algebraic expression in fourier space

$$\implies \mathcal{F}[\mathcal{L}[A(x, t)]] = \sigma_q \tilde{A}(t, q) \quad (5.4)$$

Fourier transform of nonlinear terms are taken with field dependence relying on the problem. Given the field at any time t it is possible to compute the nonlinear term in real space and taking its fourier transform afterwards.

$$\mathcal{F}[\mathcal{N}[A(t, x)]] = \tilde{a}_q(t) \quad (5.5)$$

The PDE and the system it describes converts into a set of ordinary differential equations, each modeling the time evolution of modes q .

$$\frac{d\tilde{A}(t, q)}{dt} = \sigma_q \tilde{A}(t, q) + \tilde{a}_q(t) \quad \forall q \quad (5.6)$$

To tackle this infinite dimensional problem, the procedure is to interpret $\tilde{A}(t, q)$ as coefficients of the **Discrete Fourier Transform**, DFT. It will be mentioned in APPENDIX B, but that approach let that given the periodic function as a set of discrete evaluations of itself, only a finite number of q has practical significance being the rest redundant. This is perfect for numerical calculations in which fields are inherently discrete.

The final idea underlying the method is to evolve the field in fourier space (every mode) one time step, and immediately after to compute the inverse discrete fourier transform to get the expression of the field at one time step. Thus iterating until the end of the simulation. Since \tilde{a}_q comes from the evaluation of non linear terms, it mixes all the modes making the evaluation of system given in expression (5.6) not so trivial to treat.

Integration scheme

There are many possible integration schemes to solve system (5.6) and some of them are explained in [29]. For the problem of solving the LLE it will be addressed another method, also valid for other non linear PDEs [30]. First a formal solution comes by exactly solving the linear problem and performing a change of variable that absorbs that part of the problem.

$$\partial_t \tilde{A}^l(t, q) = -\sigma_q \tilde{A}^l(t, q) \implies \tilde{A}^l(t, q) = \tilde{A}^l(t_0, q) e^{-\sigma_q(t-t_0)} \quad (5.7)$$

Hence calling

$$\tilde{A}(t, q) = z(t, q) e^{-\sigma_q(t-t_0)} \quad (5.8)$$

Inserting variable (5.8) into a mode evolving according to (5.6) yields the equation

$$\partial_t z(t, q) = \tilde{a}_q(t) e^{\sigma_q(t-t_0)} \quad (5.9)$$

The formal solution comes by integrating and reinserting the whole field expression,

$$\tilde{A}(t, q) = e^{-\sigma_q t} \left(A(t_0) e^{\sigma_q t_0} + \int_{t_0}^t \tilde{a}_q(s) e^{\sigma_q s} ds \right) \quad (5.10)$$

A rearrangement of times can be performed in a way that the solution reads

$$\frac{\tilde{A}(t + \delta t, q)}{e^{-\sigma_q \delta t}} - \frac{\tilde{A}(t - \delta t, q)}{e^{\sigma_q \delta t}} = e^{-\sigma_q t} \int_{t - \delta t}^{t + \delta t} \tilde{a}_q(s) e^{\sigma_q s} ds \quad (5.11)$$

Up to now we are dealing with the exact solution. At this point a Taylor expansion of \tilde{a}_q to zero order around $s = t$

$$\tilde{a}_q(s) \approx \tilde{a}_q(t) + \mathcal{O}(s - t) = \tilde{a}_q(t) + \mathcal{O}(\delta t) \quad (5.12)$$

gives the right hand side of the equation

$$e^{-\sigma_q t} \int_{t - \delta t}^{t + \delta t} \tilde{a}_q(s) e^{\sigma_q s} ds \approx \tilde{a}_q(t) e^{-\sigma_q t} \int_{t - \delta t}^{t + \delta t} e^{\sigma_q s} ds + \int_{t - \delta t}^{t + \delta t} \mathcal{O}(\delta t) e^{\sigma_q(s-t)} ds \quad (5.13)$$

The second integral gives the order of the final approximation,

$$\int_{t - \delta t}^{t + \delta t} \mathcal{O}(\delta t) e^{\sigma_q(s-t)} ds \approx \int_{t - \delta t}^{t + \delta t} \mathcal{O}(\delta t) ds + \int_{t - \delta t}^{t + \delta t} \mathcal{O}(\delta t) \mathcal{O}(\delta t) ds \approx \mathcal{O}(\delta t^3) \quad (5.14)$$

Being the total contribution the following result

$$e^{-\sigma_q t} \int_{t - \delta t}^{t + \delta t} \tilde{a}_q(s) e^{\sigma_q s} ds \approx \tilde{a}_q(t) \frac{e^{\sigma_q \delta t} - e^{-\sigma_q \delta t}}{\sigma_q} + \mathcal{O}(\delta t^3) \quad (5.15)$$

Finally yielding the iterative scheme

$$\tilde{A}(t + \delta t, q) = e^{-2\sigma_q \delta t} \tilde{A}(t - \delta t) + \frac{1 - e^{-2\sigma_q \delta t}}{\sigma_q} \tilde{a}_q(t) + \mathcal{O}(\delta t^3) \quad (5.16)$$

The total time step involved is $\Delta t = 2\delta t$ per iteration. Just using this algorithm, numerical solutions become unstable and may diverge. The expression makes use of the fourier transform of the field at an intermediate step t which is not initially given by the problem. A plausible solution is including an intermediate step in the algorithm where $\tilde{A}(t, q)$ is approximated. Starting from the formal solution expressed as

$$\frac{\tilde{A}(t + \delta t, q)}{e^{-\sigma_q \delta t}} - \tilde{A}(t, q) = e^{-\sigma_q t} \int_t^{t + \delta t} \tilde{a}_q(s) e^{\sigma_q s} ds \quad (5.17)$$

proceeding with the same steps one is able to reach the iteration

$$\tilde{A}(t, q) = e^{-\sigma_q \delta t} \tilde{A}(t - \delta t) + \frac{1 - e^{-\sigma_q \delta t}}{\sigma_q} \tilde{a}_q(t - \delta t) + \mathcal{O}(\delta t^2) \quad (5.18)$$

Regarding to the different integral time interval, this auxiliary expression is of order $\mathcal{O}(\delta t^2)$ since the first term in Eq. (5.14) does not vanish. The Algorithm works, first starting with an initial distribution of the field, computing its FFT and along with it solving the intermediate step by (5.18). Therefore one also obtains the FFT at such intermediate step. Finally one iterates the whole time step using expression (5.16).

5.1.2 Stochastic Partial Differential Equations

The issue of solving stochastic partial differential equations from the master thesis' point of view is addressed in this subsection. In particular to solve the LLE plus those cases included in (2.3). Not always a nice and complete numerical iteration as (5.16) is found. Each situation is treated separately

General remarks: Spatio Temporal Additive Noise and Static Multiplicative noise

Fields subjected to spatial-temporal noise considered here are,

$$\partial_t A(x, t) = \mathcal{L}[A(x, t)] + \mathcal{N}[A(t, x)] + \sqrt{D}\eta(t, x) \quad (5.19)$$

$$\partial_t A(x, t) = \mathcal{L}[A(x, t)] + \mathcal{N}[A(t, x)] + \sqrt{D}\eta(t, x) A(x, t) \quad (5.20)$$

Numerically the field only exists on a grid, both in time and space. This discretization implies taking a sample of all functions involved over such grid. Nevertheless, dealing with noise this is not possible since it is not a regular function. The approach taken goes through averaging all functions involved over the lattice cells resulting from this grid¹, including noise. This is known as **Course Grained** approach.

$$\eta_n^{(cg)}(t) = \frac{1}{\Delta x} \int_{x_n}^{x_{n+1}} \eta(x, t) dx \quad (5.21)$$

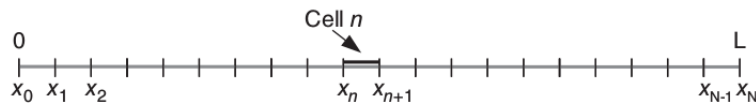


Figure 5.1: Discretization of the space in a regular lattice in one spatial dimension.

This is a stochastic process with average $\langle \eta_n^{(cg)}(t) \rangle = 0$ and correlations

$$\langle \eta_n^{(cg)}(t) \eta_m^{(cg)}(t') \rangle = \frac{1}{\Delta x} \delta_{n,m} \delta(t - t') \quad (5.22)$$

¹In fact temporal evolution consists on integrating over the time discretization.

Taking into consideration the noise gaussian nature, it let's to write the course grained noise as

$$\eta_n^{(cg)}(t) = \frac{1}{\sqrt{\Delta x}} \eta_n(t) \quad (5.23)$$

A set of n temporal noises terms. In case of pure spatial static noise, the result is more simple dealing with the integration of the spatial noise. This result is known [29] and reads

$$\eta_n^{(cg)} = \frac{1}{\Delta x} \int_{x_n}^{x_{n+1}} \eta(x) dx = \frac{1}{\Delta x} w_{\Delta x} = \frac{1}{\sqrt{\Delta x}} u_n \quad (5.24)$$

Being u_n a random gaussian number of zero mean and unit standard deviation. Regarding to pure temporal noise, even though it is homogeneous over all the spatial domain, likewise the coarse grained approximation can apply over the temporal grid.

$$\eta^{(cg)}(t) = \frac{1}{\Delta t} \int_{t_n}^{t_{n+1}} \eta(s) ds = \frac{1}{\Delta t} w_{\Delta t} = \frac{1}{\sqrt{\Delta t}} u_j \quad (5.25)$$

Again u_n being a random gaussian number of zero mean and unit standard deviation. The extension to spatio temporal noise is similar, characterizing both the average over space and time grid simultaneously by different gaussian random numbers. For the sake of notation, hereinafter all noise terms, although not explicitly mentioned, are coarse grained noise.

Turning back to the main problem, the conceptual manner to tackle it is the same; going into fourier space. This introduces the fourier transform of the noise. Its general relation is

$$\tilde{\eta}(t, q) = \frac{1}{L} \int_0^L \eta(t, x) e^{iqx} dx \quad (5.26)$$

Which also assumes noise is spatially periodic. its average, $\langle \eta_q(t) \rangle = 0$ and correlations can be computed [29],

$$\langle \tilde{\eta}_q(t) \tilde{\eta}_{q'}(t') \rangle = \frac{1}{L} \delta_{q, -q'} \delta(t - t') \quad (5.27)$$

Returning to the PDE, linear and non-linear terms remain unchanged. The infinite dimensional set of ordinary differential equations depend whether noise is multiplicative or additive

$$\frac{d\tilde{A}(t, q)}{dt} = \sigma_q \tilde{A}(t, q) + \tilde{a}_q(t) + \tilde{\eta}_q(t) \quad \forall q \quad (5.28)$$

$$\frac{d\tilde{A}(t, q)}{dt} = \sigma_q \tilde{A}(t, q) + \tilde{a}_q(t) + \mathcal{F}[\eta(t, x) A(t, x)] \quad \forall q \quad (5.29)$$

PSM relies on DFT. Using that definition of fourier transform average and correlations can be computed for $\tilde{\eta}_q(t)$. Apart from $\langle \eta_q(t) \rangle = 0$, correlations satisfy [29]

$$\langle \tilde{\eta}_q(t) \tilde{\eta}_{q'}(t') \rangle = \frac{N}{\Delta x} \delta_{q, -q'} \delta(t - t') \quad (5.30)$$

This result differs from the continuum FT approach (Eq. (5.27)) by a factor N^2 . Hence it has to be taken into account that there is a correspondence between correlations using the noise DFT and definition (5.26),

$$\tilde{\eta}_q^{(cont)}(t) \equiv \frac{1}{N^2} \tilde{\eta}_q^{(dft)}(t) \quad (5.31)$$

In this representation, each noise fourier coefficients act as white temporal noise. Continuing this introduction, the integration scheme has to consider the integration steps of noise.

Additive spatio temporal noise

Proposing the same change of variables as in the case for deterministic PDEs one reaches to the equation

$$\partial_t z(t, q) = \tilde{a}_q(t) e^{\sigma_q(t-t_0)} + \sqrt{D} \tilde{\eta}_q(t) e^{\sigma_q(t-t_0)} \quad (5.32)$$

Once integrated and after reintroducing the DFT coefficients, the formal solution reads

$$\tilde{A}_q(t) = e^{-\sigma_q t} \left(\tilde{A}_q e^{\sigma_q t_0} + \int_{t_0}^t \tilde{a}_q(s) e^{\sigma_q s} ds + \int_{t_0}^t \sqrt{D} \tilde{\eta}_q(s) e^{\sigma_q s} ds \right) \quad (5.33)$$

The addition of stochastic terms implies a two time step computation being unphysical. It would require for each $2\delta t$ to simulate an auxiliary noise term at $t + \delta t$, being dropped out for the next iteration. This is not consistent with a physical noise interpretation. Therefore the algorithm scheme is adapted to a one $\Delta t = \delta t$ step. Anyhow a random contribution into an intermediate field may be shielded by the random contribution at $\Delta t = \delta t$.

$$\frac{\tilde{A}(t + \delta t, q)}{e^{-\sigma_q \delta t}} - \tilde{A}(t, q) = e^{-\sigma_q t} \int_t^{t+\delta t} \tilde{a}_q(s) e^{\sigma_q s} ds + \sqrt{D} e^{-\sigma_q t} \int_t^{t+\delta t} \tilde{\eta}_q(s) e^{\sigma_q s} ds \quad (5.34)$$

Let's focus on the noise term

$$\tilde{g}_q(t) = \sqrt{D} e^{-\sigma_q t} \int_t^{t+\delta t} \tilde{\eta}_q(s) e^{\sigma_q s} ds \quad (5.35)$$

Since $\tilde{\eta}_q(s)$ is gaussian, that integral corresponds to a combination of gaussians, thus being a gaussian random process, with mean zero, and standard deviation given by

$$\begin{aligned} \langle \tilde{g}_q(t) \tilde{g}_{q'}(t') \rangle &= D e^{-(\sigma_q t + \sigma_{q'} t')} \int_t^{t+\delta t} \int_{t'}^{t'+\delta t} \langle \tilde{\eta}_q(s) \tilde{\eta}_{q'}(s') \rangle e^{(\sigma_q s + \sigma_{q'} s')} ds ds' \\ &= D e^{-(\sigma_q t + \sigma_{q'} t')} \int_t^{t+\delta t} \int_{t'}^{t'+\delta t} \frac{N}{\Delta x} \delta_{q, -q'} \delta(s - s') e^{(\sigma_q s + \sigma_{q'} s')} ds ds' \end{aligned} \quad (5.36)$$

This expression does not vanish if $|t - t'| < \delta t$. In that case, the dirac delta produces a contraction over one of the integral variables resulting in

$$\begin{aligned}
\langle \tilde{g}_q(t) \tilde{g}_{q'}(t') \rangle &= D e^{-(\sigma_q t + \sigma_{q'} t')} \frac{N}{\Delta x} \delta_{q, -q'} \int_t^{t+\delta t} e^{(\sigma_q + \sigma_{q'}) s} ds \\
&= \frac{ND}{\Delta x} \delta_{q, -q'} \frac{e^{[\sigma_{q'}(t-t') + (\sigma_q + \sigma_{q'})\delta t]} (1 - e^{-(\sigma_q + \sigma_{q'})\delta t})}{(\sigma_q + \sigma_{q'})}
\end{aligned}$$

Still both processes are independent and only correlated for $q = -q'$. For equations fullfilling $\sigma_q = \sigma_{-q}$ then previous equation leads to

$$\langle \tilde{g}_q(t) \tilde{g}_{q'}(t') \rangle = \frac{ND}{\Delta x} \frac{e^{\sigma_q(t-t'+2\delta t)}}{2\sigma_q} (1 - e^{-2\sigma_q\delta t}) \quad (5.37)$$

Due to practical purposes, in the PSM any instant t is given on a grid defined by $t_i = t_0 + i\delta t$. In addition to non vanishing condition $|t - t'| < \delta t$, variance is written as

$$\langle \tilde{g}_q(t_i) \tilde{g}_{q'}(t_j) \rangle = \frac{ND}{2\sigma_q \Delta x} (e^{2\sigma_q\delta t} - 1) \delta_{ij} \quad (5.38)$$

Process $\tilde{g}_q(t)$ can be exactly modeled by

$$\tilde{g}_q(t) = \left(\sqrt{\frac{ND}{\sigma_q \Delta x} (e^{2\sigma_q\delta t} - 1)} \right) \tilde{u}_q(t) \quad (5.39)$$

Where $\tilde{u}_q(t)$ is the DFT of a set of gaussian random numbers with zero mean and unit variance. The final algorithm reads

$$\tilde{A}(t + \delta t, q) = e^{-\sigma_q\delta t} \tilde{A}(t) + \frac{1 - e^{-\sigma_q\delta t}}{\sigma_q} \tilde{a}_q(t) + \tilde{g}_q(t) + \mathcal{O}(\delta t^2) \quad (5.40)$$

The most important result here is being able to exactly compute the stochastic contribution, given by gaussian random numbers.

Multiplicative Spatio-Temporal Noise

Following the previous steps faces a point where the exact derivation of the noise term is not trivial. The starting point is the following ode

$$\partial_t z(t, q) = \tilde{a}_q(t) e^{-\sigma_q(t-t_0)} + \sqrt{D} \mathcal{F}[\eta_n(t) A(t, x)] e^{-\sigma_q(t-t_0)} \quad (5.41)$$

Repeating the algorithm presentation as in previous sections of this appendix one gets to

$$\begin{aligned}
\frac{\tilde{A}(t + \delta t, q)}{e^{-\sigma_q\delta t}} - \tilde{A}(t - \delta t, q) &= \\
&= e^{-\sigma_q t} \int_t^{t+\delta t} \tilde{a}_q(s) e^{\sigma_q s} ds + \sqrt{D} e^{-\sigma_q t} \int_t^{t+\delta t} \mathcal{F}[\eta_n(s) A(s, x)] e^{-\sigma_q s} ds
\end{aligned} \quad (5.42)$$

The new unknown term is the stochastic process

$$T_q(t) = \sqrt{D} \int_t^{t+\delta t} \mathcal{F}[\eta_n(s) A(s, x)] e^{-\sigma_q s} ds \quad (5.43)$$

Involving integrals of white noise, it is a gaussian process with average and correlations as follows

$$\langle T_q(t) \rangle = \frac{\sqrt{D}}{N} \int_t^{t+\delta t} \left(\sum_{n=0}^{N-1} \langle \eta_n(s) \rangle A(s, x_n) e^{i \frac{2\pi}{L} n q} \right) e^{-\sigma_q s} ds = 0 \quad (5.44)$$

$$\begin{aligned} \langle T_q(t) T_{q'}^*(t') \rangle &= \\ &= \frac{D}{N^2} \int_t^{t+\delta t} \int_{t'}^{t'+\delta t} \left(\sum_{n_1=0}^{N-1} \sum_{n_2=0}^{N-1} \langle \eta_{n_1}(s) \eta_{n_2}^*(s') \rangle A(s, x_{n_1}) A^*(s', x_{n_2}) e^{i \frac{2\pi}{L} (n_1 q - n_2 q')} \right) e^{-\sigma_q s - \sigma_{q'} s'} ds ds' \end{aligned} \quad (5.45)$$

Using expression (5.22) the integral and summation contracts. It is worth to stress that it does not vanish if $|t - t'| \leq \delta t$. The method relies on a grid where $t_j = t_0 + j\delta t$. Thus numerically the expression vanishes unless $t = t'$. The expression arising

$$\begin{aligned} \langle T_q(t_i) T_{q'}^*(t_j) \rangle &= \\ &= \frac{D\delta_{i,j}}{N^2 \Delta x} \int_t^{t+\delta t} \left(\sum_{n=0}^{N-1} |A(s, x_n)|^2 e^{i \frac{2\pi n}{L} (q - q')} \right) e^{-(\sigma_q + \sigma_{q'}) s} ds \\ &= \frac{D\delta_{i,j}}{L} \int_t^{t+\delta t} \mathcal{F}[|A(s, x_n)|^2] e^{-(\sigma_q + \sigma_{q'}) s} ds \end{aligned} \quad (5.46)$$

This $q - q'$ non vanishing correlation prevents from finding an exact algorithm to adress the stochastic computation.

Multiplicative Spatial Noise

Even though noise is purely spatial, the fourier transform of the multiplicative stochastic term would lead to exactly the same non gaussian process but independent of time. Dropping out the dependence on time in the white noise terms yields for the correlation

$$\begin{aligned} \langle T_q(t) T_{q'}^*(t') \rangle &= \\ &= \frac{D}{N^2} \int_t^{t+\delta t} \int_{t'}^{t'+\delta t} \left(\sum_{n_1=0}^{N-1} \sum_{n_2=0}^{N-1} \langle \eta_{n_1} \eta_{n_2}^* \rangle A(s, x_{n_1}) A^*(s', x_{n_2}) e^{i \frac{2\pi}{L} (n_1 q - n_2 q')} \right) e^{-\sigma_q s - \sigma_{q'} s'} ds ds' \end{aligned} \quad (5.47)$$

While the mean remains equal. Merely spatial, in this simpler case there is no integral contraction. Summarizing, it is straightforward to obtain

$$\begin{aligned}
\langle T_q(t) T_{q'}^*(t') \rangle &= \\
&= \frac{D}{N^2 \Delta x} \int_{t'}^{t'+\delta t} \int_t^{t+\delta t} \left(\sum_{n=0}^{N-1} (A(s, x_n) A(s', x_n)) e^{i \frac{2\pi n}{L} (q-q')} \right) e^{-(\sigma_q s + \sigma_{q'} s')} ds ds' \\
&= \frac{D}{L} \int_{t'}^{t'+\delta t} \int_t^{t+\delta t} \mathcal{F} [(A(s, x_n) A(s', x_n))] e^{-(\sigma_q s + \sigma_{q'} s')} ds ds'
\end{aligned} \tag{5.48}$$

Hence being correlated for different q wavenumbers. Neither in this case the stochastic contribution is given by an exactly gaussian number amount.

5.1.3 Approximate approaches

The cases discussed, plus the not yet detailed long wavelength fluctuations schemes, show that not always is feasible a close form of the algorithm. Rather different approaches can numerically being held to achieve the results. Altogether with long wavelength fluctuations, the work proceeds as follows. The coarse grained approximation ultimately states that white noise is substituted by gaussian numbers (see Eq. (5.25) and (5.24)). Numerically time and space are discretized. Thus the stochastic contribution is introduced in the nonlinear term $a(t, x)$ as gaussian numbers corresponding to particular elements in space and time arrays/grids. Doing so the method is equivalent as solving for the deterministic case but with varying $a(t, x)$ due to the random numbers. According to the physical argument given in the explanation of the additive spatio temporal noise situation, a two time step iteration is inconsistent. Hence here it is uniquely adopted the auxiliar scheme of Eq. (5.18).

The numerical implementation of these random numbers for spatio-temporal multiplicative noise follows the formula explicitly given in equation (2.48). On the other hand to model long wavelength fluctuations, static white noise as random gaussian numbers is generated in fourier space. Then this profile is screened according to the formulas (2.49,2.50). Altogether each random mode is transformed to real space where it is added to pumping term, i.e. to the coefficient $a(t, x)$.

5.2 Appendix B: Discrete Fourier Transform

This appendix will briefly summarize what is the DFT and will mention the library used to numerically apply it to a 1D grid field.

5.2.1 DFT

In appendix A, Eqs. (5.2) are conventional definitions of fourier transform, in particular applying periodic boundary conditions over a domain $x \in [0, L]$. DFT entails numerical FT performance. Numerically, functions are discrete sets of data $f(x_n)$, $x_n = n\Delta x$; $n = 0, \dots, N-1$, corresponding to a certain grid over their domain. Hence a first approximation would be to have a discrete set of fourier coefficients, computed just using the original discrete set of function evaluations,

$$\tilde{f}_k \approx \frac{1}{N} \tilde{f}_k^{fft} \quad (5.49)$$

$$\tilde{f}_k = \sum_{n=0}^{N-1} f(x_n) e^{i \frac{2\pi}{N} kn} \quad (5.50)$$

When taking into consideration the inverse fourier transform, the infinite sum has to be replaced by a finite one using the new coefficients.

$$f(x_n) = \frac{1}{N} \sum_{k=\Lambda_1}^{\Lambda_2} \tilde{f}_k e^{-i \frac{2\pi}{N} kn} \quad (5.51)$$

It can be proven that any choice $\Lambda_2 - \Lambda_1 = N - 1$ leads to an exact correspondence $f_n \longleftrightarrow \tilde{f}_k$.

$$\begin{aligned} \mathcal{F}^{-1}(\tilde{f}_k) &\equiv \frac{1}{N} \sum_{k=\Lambda_1}^{\Lambda_1+N-1} \tilde{f}_k e^{-i \frac{2\pi}{N} kn} \\ &= \frac{1}{N} \sum_{k=\Lambda_1}^{\Lambda_1+N-1} \sum_{n'=0}^{N-1} f_{n'} e^{i \frac{2\pi}{N} (n'-n)k} \\ &= \sum_{n'=0}^{N-1} f_{n'} e^{i \frac{2\pi}{N} (n'-n)\Lambda_1} \left(\frac{1}{N} \sum_{k=\Lambda_1}^{\Lambda_1+N-1} e^{i \frac{2\pi}{N} (n'-n)(k-\Lambda_1)} \right) \\ &= \sum_{n'=0}^{N-1} f_{n'} e^{i \frac{2\pi}{N} (n'-n)\Lambda_1} \left(\frac{1}{N} \sum_{k=0}^{N-1} e^{i \frac{2\pi}{N} (n'-n)k} \right) \end{aligned} \quad (5.52)$$

In the last statement the identity $(1/N) \sum_{k=0}^{N-1} e^{i \frac{2\pi}{N} (n'-n)k} = \delta_{n,n'}$ applies, finally yielding

$$\mathcal{F}^{-1}(\tilde{f}_k) = \sum_{n'=0}^{N-1} f_{n'} e^{i \frac{2\pi}{N} (n'-n)\Lambda_1} \delta_{n,n'} = f(x_n) \quad (5.53)$$

Proposing in this way the DFT the application is completely bijective. The choice of Λ_1 does not alter the value of the coefficients at x_n but it does affect how approximate the approximation is assuming the extension to continuum between gridpoints.

Nevertheless, to prevent from a non-desired effect called **aliasing**, a proper choice of Λ_1 would be, in case of odd sampling number, $\Lambda_1 = -(N-1)/2$, or in case of even sampling number $\Lambda_1 = -N/2+1$ or either $\Lambda_1 = -N/2$.

Aliasing and Sampling Theorem

From Eq. (5.52), DFT coefficients are periodic $\tilde{f}_{k+N} = \tilde{f}_k$. Meanwhile, fourier transform coefficients decays for large $|k|$. This is a deviation in the approximation inherently present in DFT. Looking at Eq. (5.52) again, there is another deviation. Due to periodicity of $e^{i2\pi kn/N} + e^{-i2\pi kn/N}$ for $k+N/2$, greater values of k only reproduces the same spectrum cell $k \in [-N/2, N/2]$, creating an “alias”. This problem is known as **aliasing**. The wavenumber spectrum only have real resemblance to the continuum transform for $|k| < N/2$, where N refers to the function sampling, as depicted in Fig. (5.2).

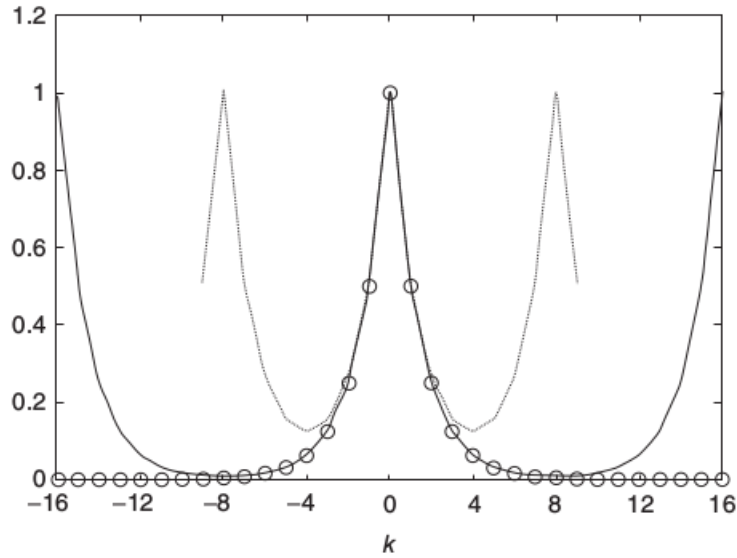


Figure 5.2: DFT Fourier transform vs Continuum Fourier transform of $f(x) = 3/(5 - 4 \cos x)$. Fourier coefficients can be analytically obtained; $\tilde{f}_k = 2^{-|k|}$. The two lines that do not decay correspond to function sampling DFT with $N = 8$ for the dotted curve and $N = 16$ for solid one. Clearly aliasing appears by reproducing the “alias” for smaller $|k| > N/2$. Picture taken from [29]

A comment about it is that this deviation in the approximation is independent of the bijective correspondence between $f_n \longleftrightarrow \tilde{f}_k$, but relies on the sampling size. Coefficients will retrieve the same function sampling, but its DFT will differ.

The previous result can be understood as the corollary stemming from the **Sampling Theorem**

[31]. It states that given the maximum characteristic system frequency ν , then the sampling rate has to be 2ν to effectively reproduce it seen in Fig. 5.3. That maximum significant system frequency k^* is such that $\tilde{f}_k \geq \tilde{f}_{k^*} \quad \forall |k| < |k^*|$ in the continuum fourier transform.

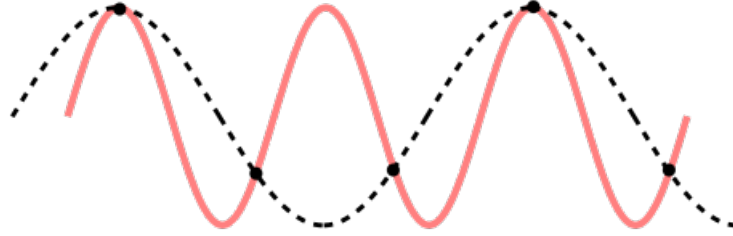


Figure 5.3: The samples of two sine waves can be identical, when at least one of them is at a frequency above half the sample rate.

To sum up, a smart choice of N requires $\nu = (N\Delta k)/2$ so that the simulation captures all the important modes of the system and does not present aliasing. Not considering nothing else the system size is defined as $\Delta k = 2\pi/L$ being the smallest system's wavenumber. So to settle down the whole system, only N and Δk are required as parameters. For instance $\Delta x = L/N = 2\pi/N\Delta k$.

5.2.2 Subroutine Fast Fourier Transform from the West (FFTW)

The implementation of the DFT comes by the **Fast Fourier Transform** Algorithm. References of this algorithm can be found in [29]. In particular the FORTRAN subroutine library that was used is called FFTW [32]. This subroutine has a simple implementation. First as a preamble it needs to create two plans.

```

integer fftw_forward , fftw_backward
parameter ( fftw_forward = -1, fftw_backward = 1)

integer fftw_estimate , fftw_measure
parameter ( fftw_estimate = 0, fftw_measure = 1)

integer fftw_out_of_place , fftw_in_place , fftw_use_wisdom
parameter ( fftw_out_of_place = 0)
parameter ( fftw_in_place = 8, fftw_use_wisdom = 16)

call fftw_f77_create_plan ( plf , n, fftw_forward ,
*   fftw_estimate + fftw_in_place )
call fftw_f77_create_plan ( plb , n, fftw_backward ,
*   fftw_estimate + fftw_in_place )

```

Each plan is labeled by the first integer argument, plf or plb in this case. Next, n is the sampling size. The third argument indicates if that plan will perform the fourier transform (+1) or either the inverse transform (-1). Finally the last combination of parameters as the fourth integer argument indicates that once performed the transformation, the output is stored in the same input sampling array. A deeper understanding of this parameters is found in the reference.

To perform the transformation one needs to call the subroutine

```
call fftw_f77_one(plf,eant,dummy) ! Fourier transform
call fftw_f77_one(plb,eant,dummy) ! Inverse Fourier transform
```

Where eant is the array introducing the sampling and recovering the transformation. Using this scheme dummy is an analogous empty array which does not play any role since we it is required not to storage the output in any different array. Under other parameters it serves as the preceding consideration. A final consideration has to be considered here, approximation Eq. (5.50) needs to be included in the array prior to the subroutine plf call.

Bibliography

- [1] S. Cundiff, J. Ye, and J. Hall, *Sci. Am.* **294**, 74 (2008).
- [2] Andrew D. Ludlow, Martin M. Boyd, Jun Ye **Optical Atomic Clocks** *Reviews of Modern Physics*, Volume 87 (April 2015)
- [3] Chih-Hao Li, Andrew J. Benedick, Peter Fendel, Alexander G. Glenday, Franz X. Kartner, David F. Phillips, Dimitar Sasselov, Andrew Szentgyorgyi, Ronald L. Walsworth **A laser frequency comb that enables radial velocity measurements with a precision of 1 cm s⁻¹**, *Nature*, **452** (2008)
- [4] Th. Udem and F.Riehle **Frequency combs applications and optical frequency standards**. *Rivista del nuovo cimento* Vol. 30, N. 12 2007.
- [5] Victor Torres-Company, Andrew M. Wiener, **Optical frequency comb technology for ultrabroadband radio frequency photonics** *Lasers and Photonics Reviews*, issue **3** vol. **8** (2004).
- [6] I. Coddington, W.C. Swann, L. Nenadovic, N. R. Newbury **Rapid and precise absolute distance measurements at long range** vol. *Nature Photonics* **3** (2009).
- [7] Matthew C. Stowe, Michael J. Thorpe, Avi Pe'er Jun Ye, Jason E. Stalknaker, Vladislav Gerginov, Scott A. Diddams **Direct Frequency Comb Spectroscopy** *Advances in Atomic, Molecular and Optical Physics* vol. **5** (2005).
- [8] **Construction of a femtosecond mode-locked laser**<http://www.df.unipi.it/~fisapp/Gruppi/Metrologia/spiegazioni/boris.pdf>
- [9] Maleki, Lute **High Performance Optical Oscillators for Microwave and mm-wave Applications** *Microwave Journal* issue **6**, vol. **56** (2013).
- [10] P. Del'Haye *et al.*, **Optical frequency comb generation from a monolithic microresonator** *Nature* (London) 450, 1214 (2007).
- [11] P. Del'Haye, **Optical Frequency Comb Generation in Monolithic Microresonators**, chapter 1, phd thesis 2011.
- [12] Yanne K. Chembo, Nan Yu, **Modal expansion approach to optical-frequency-comb generation with monolithic whispering-gallery-mode resonators**, *Physical Review A* **82**, 033801 (2010).
- [13] T. Herr, **Solitons and dynamics of frequency comb formation in optical microresonators**, chapter 2, phd thesis 2013.

- [14] H.A. Haus, IEEE J. Sel. Top. Quantum Electron, 6, 1173 (2000).
- [15] Yanne K. Chembo, Curtis M. Menyuk, **Spatiotemporal Lugiato-Lefever formalism for Kerr-comb generation in whispering-gallery-mode resonators**, Physical Review A **89**, 053852 (2013).
- [16] P. Parra-Rivas, D. Gomila, M. A. Matías, S. Coen and L. Gelens. **Dynamics of localized and patterned structures in the Lugiato-Lefever equation determine the stability and shape of optical frequency combs**, Physical Review A **89**, 043813 (2014).
- [17] D. Gomila, Pere Colet. **Fluctuations and correlations in hexagonal optical patterns**, Physical Review E **66**, 046223 (2002).
- [18] P. Del'Haye *et al.* **Octave Spanning Tunable Frequency Comb from a Microresonator** Physical Review Letters **107**, 063901 (2011).
- [19] Tilo Steinmetz *et. al.*, Science 5 September 2008: Vol. **321** no. 5894 pp. 1335-1337.
- [20] Jinendra K. Ranka, Robert S. Windeler, and Andrew J. Stentz **Visible continuum generation in air-silica microstructure optical fibers with anomalous dispersion at 800 nm**, Optical letters, issue 1, vol. **25** (2000).
- [21] V.B. Braginsky, M.L. Gorodetsky, V.S. Ilchenko **Quality-factor and nonlinear properties of optical whispering-gallery modes** Physics Letters A issues 7–8 vol. **137** (1989)
- [22] D. K. Armani, T. J. Kippenberg, S. M. Spillane & K. J. Vahala **Ultra-high-Q toroid microcavity on a chip** Nature **421**, 925-928 (2003)
- [23] S. M. Spillane, T. J. Kippenberg & K. J. Vahala **Ultralow-threshold Raman laser using a spherical dielectric microcavity** Nature **415**, 621-623 (2000)
- [24] J. U. Fürst, D. V. Strekalov, D. Elser, A. Aiello, U. L. Andersen, Ch. Marquardt, and G. Leuchs **Low-Threshold Optical Parametric Oscillations in a Whispering Gallery Mode Resonator** Phys. Rev. Lett. **105** (2010)
- [25] T. J. Kippenberg, S. M. Spillane, and K. J. Vahala **Kerr-Nonlinearity Optical Parametric Oscillation in an Ultrahigh-Q Toroid Microcavity** Phys. Rev. Lett. **93** (2004)
- [26] Vladimir S. Ilchenko, Anatoliy A. Savchenkov, Andrey B. Matsko, and Lute Maleki **Nonlinear Optics and Crystalline Whispering Gallery Mode Cavities** Phys. Rev. Lett. **92** (2004)
- [27] Tal Carmon & Kerry J. Vahala **Visible continuous emission from a silica microphotonic device by third-harmonic generation** Nature Physics **3** pp. 430-435 (2007)
- [28] RP Photonics Encyclopedia; http://www.rp-photonics.com/mode_locking.html.
- [29] Raúl Toral, Pere Colet, **Stochastic Numerical Methods: An Introduction for Students and Scientists**, Wiley (2014)
- [30] R. Montagne, E. Hernandez-Garcia, A. Amengual and M. San Miguel **Wound-up phase turbulence in the Complex Ginzburg-Landau Equation**. Appendix A. Phys. Rev. Lett. **77**, 267 (1996)

- [31] Wikipedia Sampling Theorem https://en.wikipedia.org/wiki/Nyquist-Shannon_sampling_theorem.
- [32] FFTW webpage <http://www.fftw.org/>.